UNIVERSITY OF CALIFORNIA, SAN DIEGO

Non-Explosive Simulated Blast Loading of Composite Sandwich Beams

A Thesis submitted in partial satisfaction of the requirements
for the degree Master of Science

in

Structural Engineering

by

Antony C. Chen

Committee in charge:

Professor Hyonny Kim, Chair
Professor Francesco Lanza di Scalea
Professor Michael Todd

2010

The Thesis of Antony C. Chen is approved, and it is acceptable in quality and form for publication in microfilm and electronically:

_____

_____

_____

Chair

University of California, San Diego

2010

TABLE OF CONTENTS

LIST OF ABBREVIATIONS

B Sandwich beam width

b Transformed core width

D Total sandwich beam depth

d Depth of balsa core

FC Force cell

FEA Finite element analysis

GG Dynamic speed gas gun test

IS Intermediate Speed

LHS Left hand side

PPGP Pressure pulse generating projectile

QS Quasi-static

RHS Right hand side

LIST OF FIGURES

LIST OF TABLES

ACKNOWLEDGEMENTS

I would like to take this opportunity to thank Professor Hyonny Kim for giving me the opportunity to research and study the field of advanced composites. His guidance and knowledge has been instrumental in helping me through my research. It has also instilled in me a passion for the field and to use my knowledge to go on and create bigger and better things for the benefit of the world.

I would also like to thank all of my fellow students who have spent time working in SERF291 lab or downstairs in the impact lab. Thank you for helping me lift heavy objects, cut composites, and break things. Your help and company have made this time here infinitely more enjoyable.

I would also like to thank all the professors here at UC San Diego who have taught me and challenged me throughout my stint here.

Thank you all.

ABSTRACT OF THE THESIS

Non-Explosive Simulated Blast Loading of Composite Sandwich Beams

by

Antony C. Chen

Master of Science in Structural Engineering

University of California, San Diego 2010

Professor Hyonny Kim, Chair

A dynamic loading method for simulating explosive blast was developed using a crushing foam projectile launched by a gas gun at velocities ranging from 30-60 m/s. This test method is used to load composite specimens to study the dynamic failure of carbon/epoxy sandwich beams. The beams consist of an end-grain balsa core and carbon

fiber laminate facesheets. A focused study was conducted on the failure behavior of the facesheets, in isolation of core-failure effects, as well as the behavior of the full sandwich structure. Dynamic three point bending was conducted using the crushing foam loading methodology to impart simulated dynamic blast loading at relevant strain rates onto the beam specimens. Slower, more controlled dynamic tests, as well as quasi-static tests, were also performed using a servohydraulic test machine to obtain a highly detailed view of the specimens' behavior during the failure process.

INTRODUCTION

Advanced composites are becoming more widely used as materials for various classes of structures. In particular, the use of composites in the construction of large load bearing ship structures has been increasing steadily over the past few decades. Mouritz *et. al.* [1] provides a detailed review of a number of recent developments in advanced naval composite structures. Composites were first used immediately after World War II in the construction of small personnel boats. These structures proved to be stiff, strong, durable and easy to repair, leading to the rapid expansion of the use of composites for numerous naval structures. Studies have shown that use of composites over traditional materials such as steel and aluminum has been found to drastically reduce the structural weight of the boat hull and increase fire resistance. The reduced hull weight allows for an increase in military payload as well as greater range and reduced fuel consumption for the vehicle. Construction of composite structures tends to be more expensive than with traditional materials. Use of composites, however, reduces maintenance costs due to their resistance to corrosion and reduction of fatigue cracking, which on top of increased fuel economy, allows for lower operating costs over the life of the vehicle. Currently a lack of empirical data has impeded more widespread use of composites. For example, the resistance of advanced composites to damage caused by explosive loading has yet to be fully addressed. Knowledge of the vulnerability and survivability of composite structures to blast loading can be essential in the

design of composite structures for a number of applications, especially military. Increased knowledge of composites behavior can also be instrumental in the expansion of the use of composites over existing structural materials.

Dynamic behavior overall must be studied to the depth it has for other materials such as metals and alloy. Because of this, many concerns still exist pertaining to the behavior of composites when subjected to high strain rates imposed by blast loading. The objectives of this study are two-fold. First is the development of a non-explosive based methodology to impart dynamic loading that would produce relevant deformation and failure modes in test specimens as well as to be used to measure material properties and to document failure modes. Second, is the use of this methodology to gather failure strain measurements and observations of the failure modes and failure process in small scale test specimens (e.g. beams) with the intention of providing basic-level data that is to be used to support the formulation of computational failure models of a given material when subject to dynamic blast loading. Understanding the failure behavior of these materials in the small scale can help to understand and predict the failure of structures in the full scale since most failure initiates as small-scale local processes which are observed by use of appropriate reduced-sized test specimens.

This dynamic testing methodology must be capable of meeting a number of requirements. First, it must be able to reproduce a pressure time history representative of actual blast (in air). Second, it must be relatively inexpensive and time effective because numerous tests must be conducted for the purposes of collecting data used for the

calibration and validation of material constitutive and failure models. Finally, the methodology must allow for the comprehensive collection of data including local strain and deflection over time as well as the visual observation of specimen response.

Of interest for this study are advanced composite panels intended for use on naval vessels. The panels consist of an end-grain balsa core and carbon fiber laminate facesheets. Experimentation has first been conducted on facesheets that have been separated from the core to conduct a focused study on the failure behavior of the facesheets, in isolation of core-failure effects, when subjected to dynamic three-point bending. The previously defined non-explosive dynamic test method was used to impart dynamic loading and observe the resulting behavior of beam type specimens. These tests were then supplemented with quasi-static and intermediate-rate dynamic tests to more carefully observe behavior of the specimens up to and beyond failure as well as observe any dependency upon loading rate. Next, the dynamic failure of the sandwich beams is studied using the same loading methodologies. The same range of fast to slow rate tests were conducted to study the behavior of the full sandwich structure when subjected to dynamic loading with the goal of gathering material constitutive data and failure modes of the specimens. All test results are presented as a function of loading rate.

CHAPTER 1 LITERATURE REVIEW

Review of Blast Features

Details on blast loading in the open literature have focused on the description of overpressure pulse measurements onto full-scale walls and smaller-scale test panels. A selection of these is summarized here for the purpose of describing the range of pressures and duration of pulse that are relevant to the topic of blast loading onto structures.

A pressure pulse typical of blast loading begins a sudden rise to a large peak pressure followed by an exponential decay into a flat overpressure tail, pressure above ambient atmospheric pressure, which gradually decays to atmospheric pressure. Jacinto *et al*. [2] conducted a series of air-blast tests to measure overpressure pulses and the dynamic response of plates for explosive charges ranging in mass from 0.8 to 10 kg located at 30 to 60 m from target plates of 1 to 1.5 m^2 in area. They measured pressure pulses which had an almost immediate rise to peak pressures in the 1-10 kPa range with pressures tapering-off over durations of up to 10 ms. Scherbatiuk and Rattanawangcharoen [3] conducted open air blast tests on free-standing soil-filled concertainer walls (folded wire mesh geotextile lined cubical connected baskets) walls and measured pulses of similar shape and of magnitudes in the range 0.8 to 6 MPa and lasting for durations of 3 to 8 ms. Thus after peak

pressures were attained, the pressures expectedly dropped off in the above mentioned time periods. In still other experiments, peak and overpressures pressures were measured by Houlston *et al.* [4] in the range 50 kPa to nearly 4 MPa for durations of 1 to 2 ms in for blasts onto test plates. Details of charge type and mass were not provided, but it is notable that at the higher pressures attained, the pulse durations were no longer than 1 ms. Davidson *et al*. [5] measured peak pressures in the 300 kPa range with durations of roughly 10 ms for blasts onto polymer-reinforced concrete masonry walls.

Studies have been conducted on blast induced pressures directly related to ship structures as illustrated by the following examples. Slater [6] investigated blast-resistance of glass fiber reinforced plastic (GRP) composite panels for use in naval ship structures. Full-scale test panels, with dimensions 2.7 m x 4.9 m, were subject to explosive blast loading. Measured pressure pulses reported had peak pressures of 105 to 405 kPa (classified as moderate and severe conditions, respectively) and durations of 50 to 100 ms for panel and beam specimens, and 200 ms for the full-scale test panel. Methods for investigating blast damage to composites by smaller-scale test specimens were reported on by Mouritz [7] who studied underwater blast loading onto relatively small (270 x 70 mm) stitched composite test specimens by suspending 30 or 50 g of explosive 1 m distance away from the specimen under water. These produced low and high intensity blast overpressures, with peak pressures reaching 13 and 25 MPa, respectively, as measured by a pressure sensor mounted onto the specimen surface. The pulses were roughly triangular in profile, with an almost equal rise and decay time, lasting 20 to 35 μs and were used to excite damage, namely delamination cracking, in

the test specimens. Surveys such as these, therefore, show that blast peak pressures of typical interest lie in a rather broad range of about 0.5 to10 MPa, with overpressure durations ranging from 0.5 to 10 ms or even higher. This current study is focused on dynamic loading of smaller-scale test specimens. Because these specimens are typically on an order of magnitude smaller in scale relative to full-size ship structures, higher magnitude pressures are needed in order to excite failure. Of main interest, therefore, is the time-scale for which these pressure pulses are being applied.

Use of Projectiles in Blast Simulation

Application of non-explosive based dynamic loading has been achieved using projectiles to excite dynamic loading on small scale composite specimens. Recent studies [8-10] using a metallic foam projectile have been conducted to achieve results to this effect. Development of the projectile began with the characterization of the high strain rate compressive behavior of aluminum alloy foams by Deshpande and Fleck [8], detailing constitutive properties of two aluminum alloy foams. They found a minimal strain-rate dependence of the aluminum alloy foams under compression, thus allowing for the development of a rate-independent constitutive law. A study by Radford *et al.* [9] looked into using the same aluminum foams as a pressure pulse generating projectile by characterizing pressure histories created by the projectiles when impacting onto a Kolsky bar. Findings revealed that metal foams collapse at almost constant pressures, with pressure magnitudes increasing on the order of hundreds of MPa with dynamic

loading rates compared to quasi-static loading due to shock wave propagation. The collapse pressure could be further controlled by the density of the foam used. The goal was to simulate intense underwater fluid shock loading with pressure pulses having 10-300 MPa peak values and a decay times on the order of 0.1 ms. These projectiles were implemented by Rathbun *et al.* [10] to study the performance of stainless steel honeycomb core sandwich structures subjected to dynamic loading. The performance of the sandwich beams is compared to solid beams of an equivalent weight to demonstrate the benefits of sandwich construction.

There is however a concern that the use of harder materials such as metallic foams may incite more of a ballistic impact response and associated localized failure. This can be useful in simulation of fluid shock loading, however the present study is more concerned with the simulation of lower intensity air blast loading. To this goal, a crushing projectile using a softer polymer foam material is to be explored. Extensive research into the compressive behavior of polymer foams was conducted by Gong *et. al.* [11, 12] and Jin *et. al.* [13] showing similar behavior under compression to the metal foam, albeit with lower maximum pressures developed.

Review of Dynamic Beam Bending

The failure behavior of sandwich panels used on composite ship structures when subject to explosive blast loading is to be explored via dynamic testing of beam specimens. The failure of composites under dynamic load has not been studied in as

great a depth as it has for metals and alloys. For instance, there is extensive research into dynamic three-point bend testing of other materials to investigate their fracture behavior. Charpy or drop-weight tests are typically used to provide a dynamic load input. Dynamic fracture toughness is then evaluated by measuring the response of the specimen or analyzing the impact [14-16]. To facilitate very high loading rates in 3-point beam bending tests, Yokoyama *et al.* [17] developed a technique wherein a pre-cracked bend specimen was held in place by three Hopkinson bars: two to provide a simply-supported boundary conditions and one to provide loading. A striker bar was then launched from a compressed air gun to strike the loading bar and impart a dynamic load into the specimen. Response from the Hopkinson bars as well as the specimen was then recorded.

Research has also focused on the failure modes and bending behavior of composite sandwich beams subjected to three-point bending, typically under a static load [18-20]. A dynamic bend test was performed by Crupi *et al.* [21] with force imparted using a pendulum hammer. Techniques such as these do not, however, create the strain rates necessary to simulate explosive blast loads such as those from the previously described Rathbun *et al.* [10] study. Lim *et al.* [22] utilized a compressed air impactor to induce dynamic three-point bending in E-glass/Epoxy and PVC foam core sandwich beams. This study illustrated the dependence on facesheet thickness and core density to failure mode. Thicker facesheets and a lower density core resulted in failure modes dominated by core shear while thinner facesheets and a higher density core resulted in failure modes dominated by facesheet failure.

Of issue in the study reported on at present is the behavior of a balsa wood core. Studies have been performed on the mechanical characteristics of balsa. Da Silva *et al.* [23] conducted an extensive study of the constitutive properties of balsa under compression. Vural and Ravichandran [24] performed research on the dynamic response of balsa wood noting the dependence of initial failure with the rate of loading. Therefore rate dependent characteristics may be seen in sandwich structures with a balsa wood core.

CHAPTER 2 PROJECTILE DEVELOPMENT

Non-explosive based dynamic loading is created by launching a “soft” crushing projectile. The ultimate goal was to create a projectile with the capability of producing a known pressure pulse to excite failure in composite panel targets of varying geometry and boundary conditions. The pressure pulse would require the following attributes: peak pressures that are scalable depending on specimen span (smaller specimens requiring higher pressure compared to full-scale structures to generate failure), a controllable rise time to that peak pressure, and a controllable overpressure magnitude. Fig. 1 illustrates a generic example of a desired pressure pulse shape, where an initial peak pressure is followed by an overpressure level before dropping off to zero.

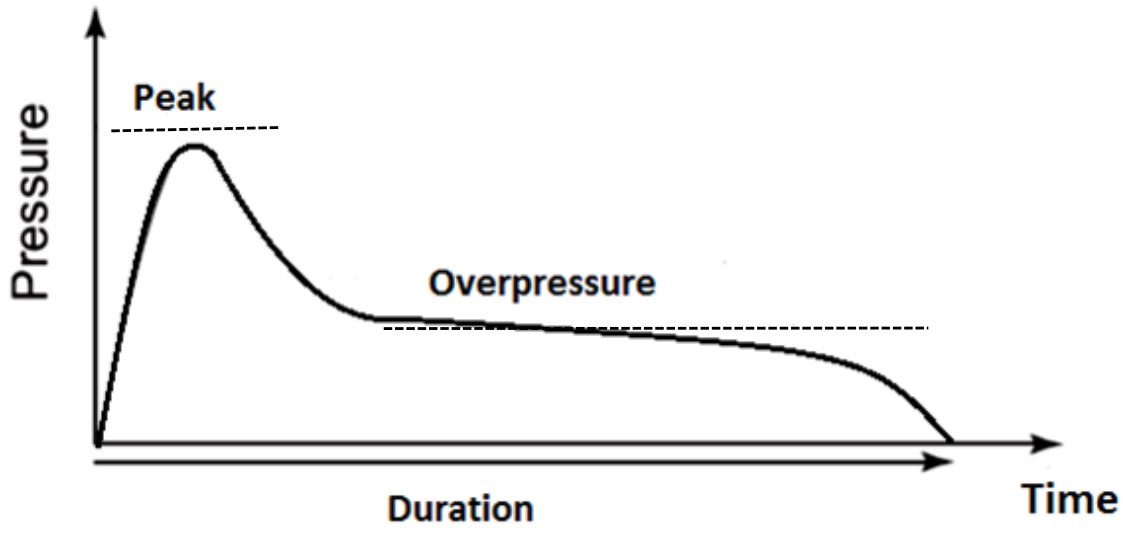

Figure 1. Desired pressure pulse features

Urethane Foam Projectiles

A soft projectile, referred to herein as the pressure-pulse generating projectile (PPGP) is constructed of a two-part liquid cast crushable rigid urethane foam mounted in front of a 663 g aluminum body. The projectile body has a 78.9 mm diameter and is constructed from one of three rigid urethane foams of nominal density 80, 160, and 240 kg/m^3 (5, 10, and 15 lb/ft^3 Smooth-On Foam-iT! series castable urethane foam). Rise times and peak magnitudes could be controlled by changing the foam density. Polymer foam was chosen as a crushable media due to the desirable compressive stress vs. strain behavior these materials have been show to exhibit [11-13]. Specifically, under large compressive crushing strain, the polymer foams showed an almost elastic-perfectly plastic response with the magnitude of the "yielding" stress directly controllable by selection of the density of foam. Similar quasi-static and dynamic tests compression tests were conducted with the foams used herein, with results shown in Fig. 2 and 3. Specimens of each foam density were molded into cylinders with diameters of 76.2 mm and lengths of 101.6 mm. These were tested using a servohydraulic 100 kN capacity MTS 810 material test system (uniaxial tension/compression test machine). Each specimen was placed under compression between two hardened steel platens and crushed at quasi-static ($3.33x10^{-4}$ m/s) and dynamic (0.25 m/s) speeds. The resulting stress versus strain curves are shown in Figs. 2 and 3.

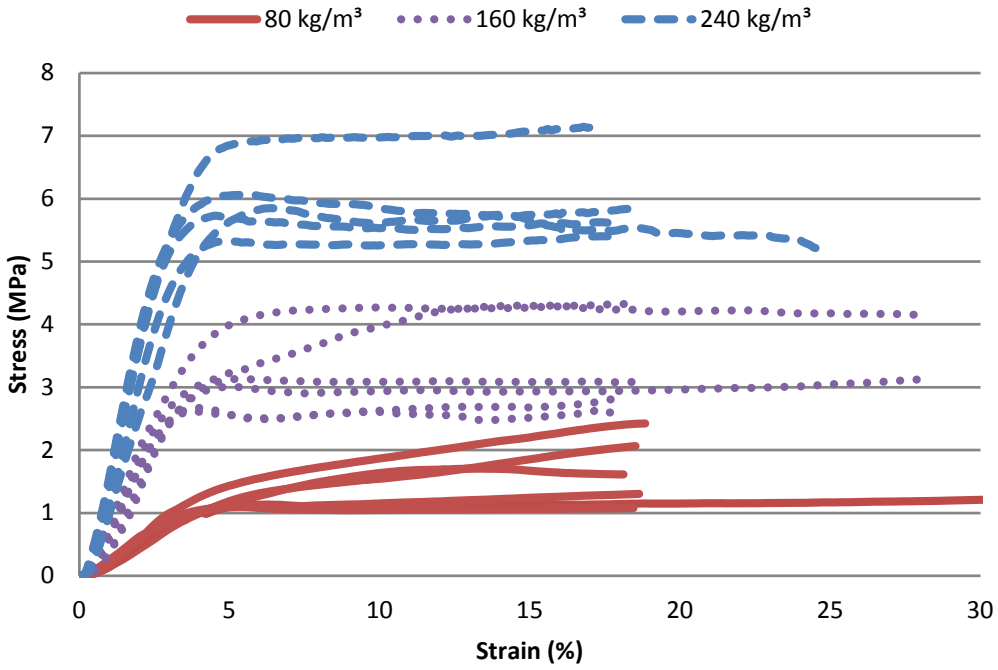

Figure 2. Stress versus strain for quasi-static foam compression tests; 3.33×10^{-4} m/s

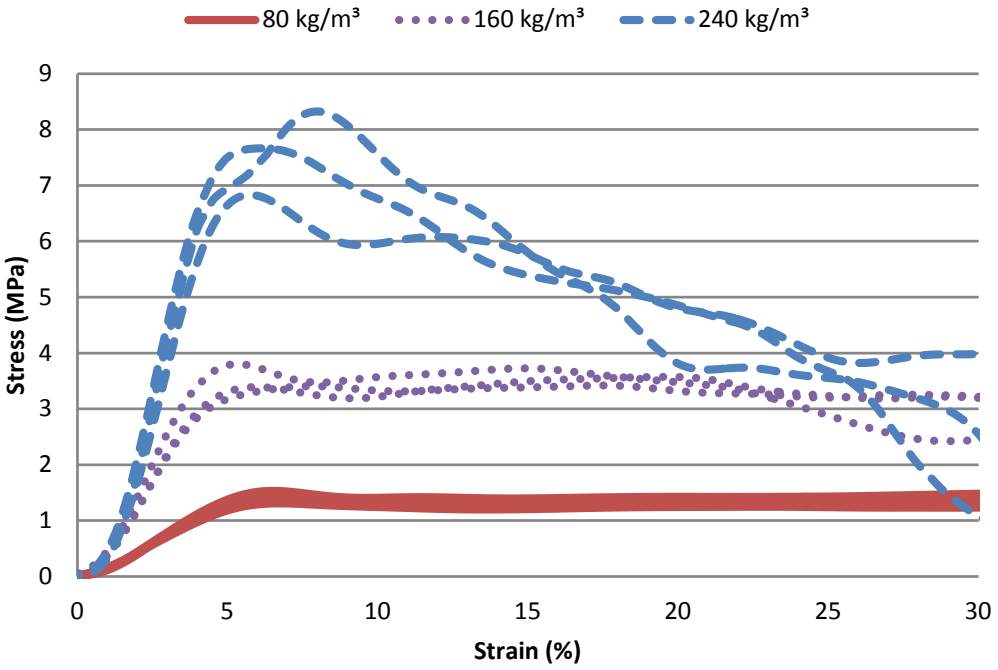

Figure 3. Stress versus strain dynamic foam compression tests; 0.25 m/s

Stiffness and yield strengths were calculated from these results and are shown in Tables 1 and 2. Similar to studies from earlier literature, these results displayed an almost elastic-perfectly plastic response, with stiffness and yield stresses increasing linearly with foam density. Note a dramatic drop-off in the stress versus strain curves of the 240 kg/m^3 as well as less dramatic behavior in the 160 kg/m^3 projectile prior to yielding while under dynamic compressive loading. The outer walls of the specimen would buckle when yielding leading fracturing of the entire specimen. This is in contrast to the other tests which would perfectly crush creating a stress plateau as the specimen yielded. Comparing the dynamic and quasi-static tests reveal rate independent behavior in foam stiffness (see Table 1), however yield stress tended to be higher in the dynamic tests (see Table 2), particularly for the 240 kg/m^3 foam. These data show that the rigid urethane foams used in this study can be used to control the pressure peak by selection of density, or even by modification of the density via addition of filler particles to increase mass.

Table 1. Foam compressive yield strength (MPa) Quasi-static Tests at 3.33x10^{-4} m/s

Test no.	**80 kg/m^3**	**160 kg/m^3**	**240 kg/m^3**
1	1.6819	4.2677	6.0516
2	1.2678	3.0015	5.8397
3	1.1312	4.2972	5.2534
4	1.0902	3.128	5.7699
5	1.1104	2.659	6.9559
6	1.5305	2.5985	5.3173
average	1.302	3.325317	5.864633

Table 2. Foam compressive yield strength (MPa) Dynamic tests at 0.25 m/s

Test no.	80 kg/m³	160 kg/m³	240 kg/m³
1	33.2	111.9	234.6
2	27.5	94.4	208.7
3	33.1	96.2	215.5
average	31.3	100.8	219.6

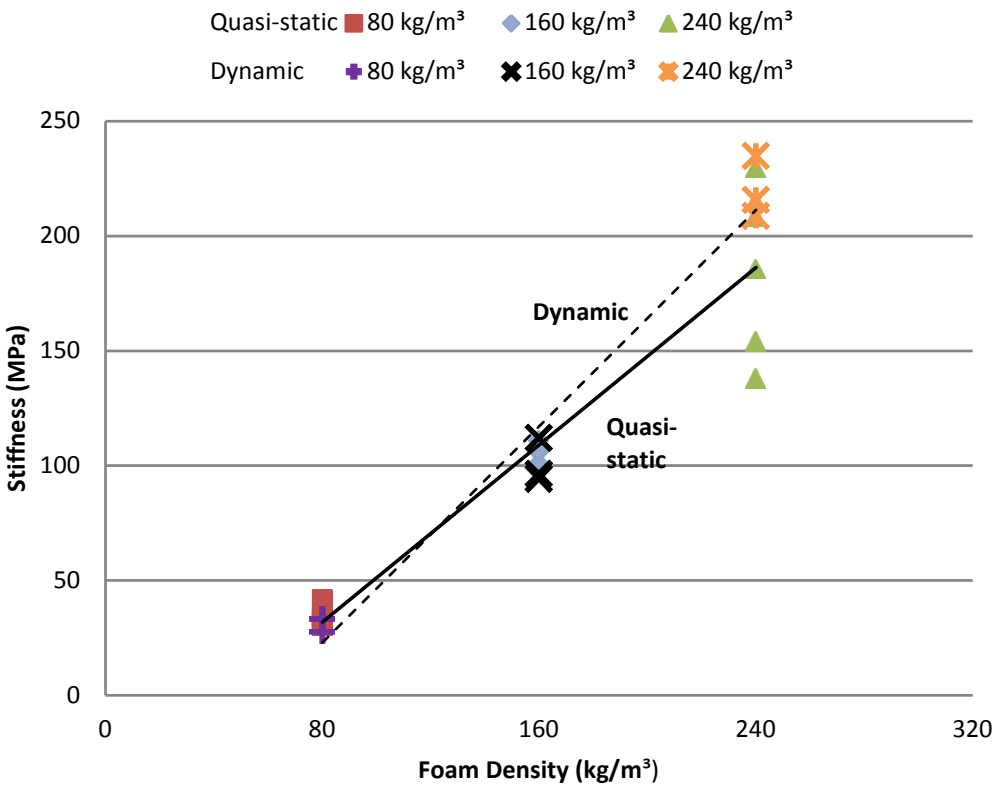

Figure 4. Stiffness versus foam density

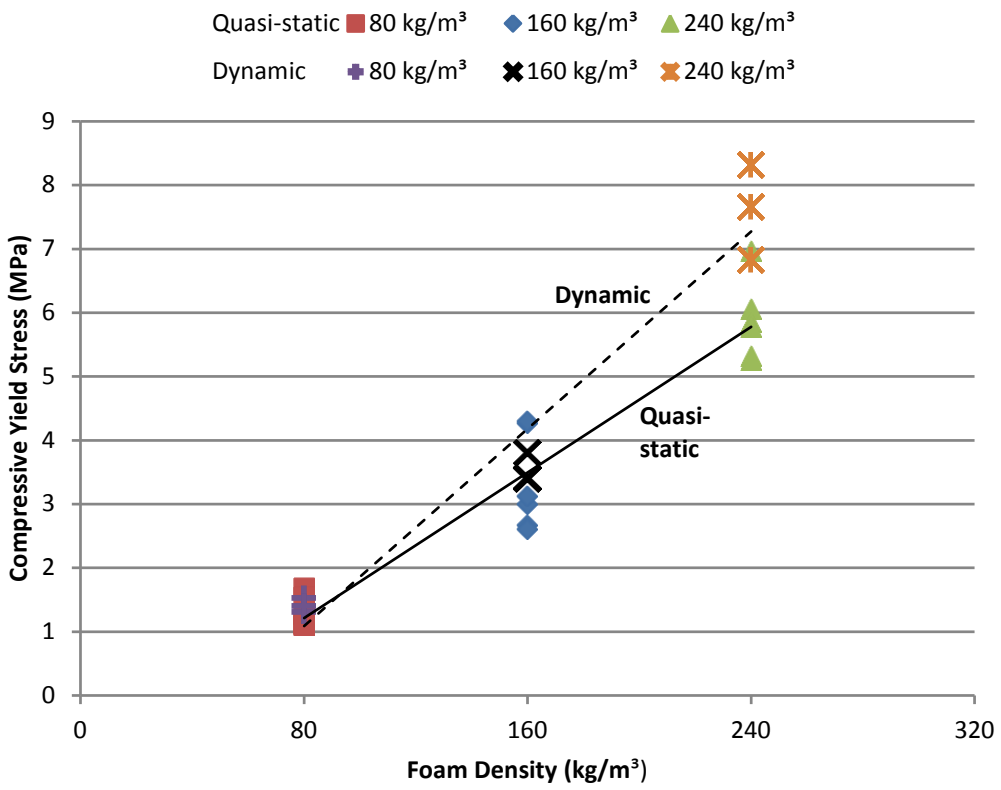

Figure 5. Compressive yield stress versus foam density

Initial Projectile Design

An initial design of the projectile is shown in Figure 7. Three part foam mold (a) foam body (b) foam body extension (c) curved face, consisted of an 88.9 mm length cylinder of crushable foam. An aluminum body (mass) mounted aft of the foam provides a way to impart large amounts of momentum and to drive crushing of the entire foam length, as well as hold the V-seals that produce a low-friction gas-tight seal between the projectile and barrel. Aft of the body are lightweight flexible foam fins to provide flight

stability to the projectile. Between the foam and the aluminum body is a liquid-cast dense urethane plastic interface section that reinforces the connection of the crushable foam to the body. Without this dense plastic section, the foam would tend to locally crush at this location where it contacts the aluminum body.

Fabrication of the projectile consists of molding the crushable foam and plastic interface section as one continuous unit using a three piece stainless steel closed mold (see Fig. 7) which defines a gently curved 38.1 mm radius forward-facing geometry. The process begins by mixing (two liquid parts) and pouring the rigid urethane foam into the cylindrical mold. The resulting cylindrical shape is trimmed by a length of 12.7 mm before it is placed back into the mold and the liquid urethane casting plastic is poured in. This non-expanding plastic fills up the rest of the mold creating the dense plastic interface geometry which then inserts snugly into a socket on the forward face of the aluminum projectile body. As shown in Fig. 6.

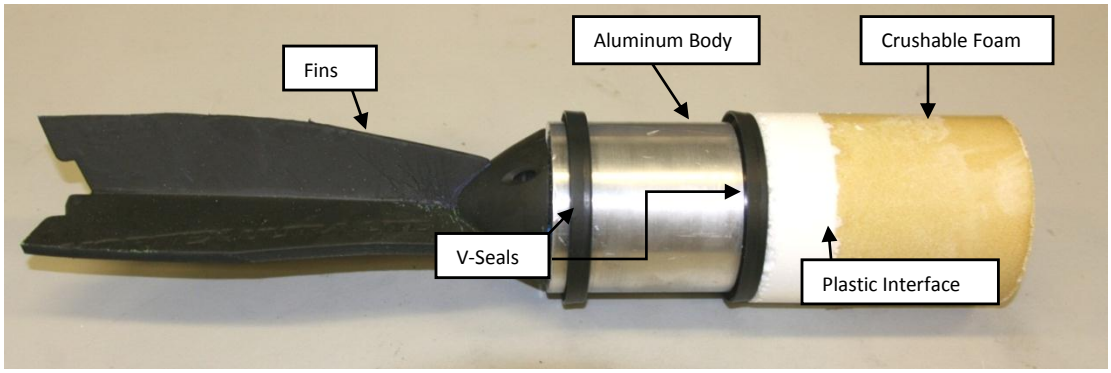

Figure 6. Initial design of PPGP

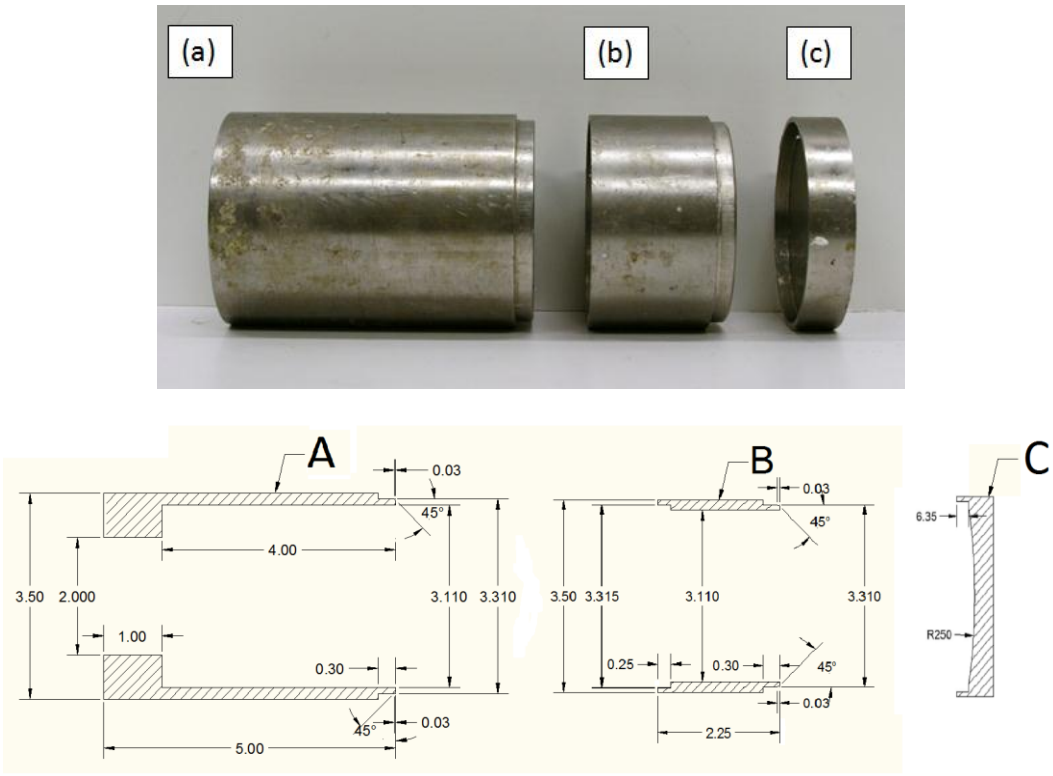

Figure 7. Three part foam mold (a) foam body (b) foam body extension (c) curved face (dimensions in inches)

An initial set of tests were conducted to observe the flight characteristics of the projectile as it is desired to achieve stable flight as well as a normal-contact impact to uniformly compress the projectile. Observation by high-speed video shows the flight path to be straight and stable, with no gross tilting or even spin of the projectile. Upon confirmation of stable flight, impacts onto the force measurement bar (FMB described in Ch. 3) were carried out to characterize the pressure pulses produced by the different foam densities. Fig. 8 shows the PPGP impacting its target at an incoming velocity of 30.5 m/s. The projectile is observed to strike the target squarely and then crush as it imparts a pressure pulse.

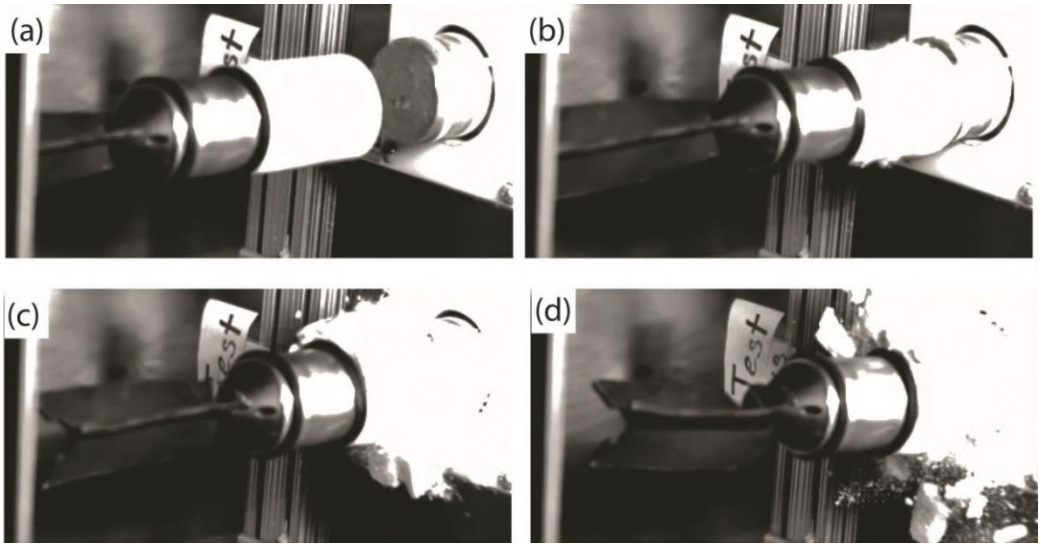

Figure 8. PPGP impacting FMB at 30.5 m/s; 160 kg/m^3 density foam

Typical pressure pulse measurements for the three foam densities tested are plotted in Figs. 9 to 11 for projectiles launched at a nominal velocity of 30.5 m/s. Repetitions show the projectiles to produce pressure pulses that were fairly consistent in peak pressures, rise times, and pulse duration. It can be clearly observed that higher foam densities result in higher peak pressures, and the lowest density foam exhibited longer pulse duration.

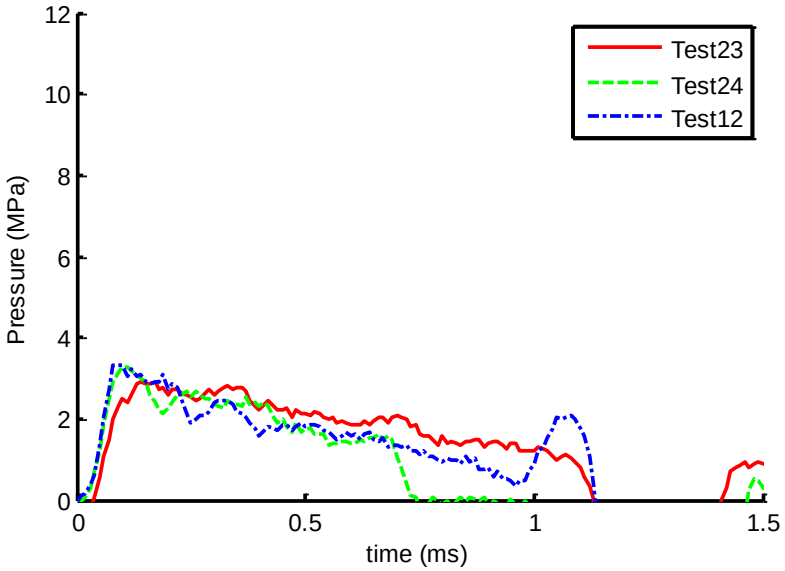

Figure 9. Pressure history for 80 kg/m^3 projectile at 30.5 m/s

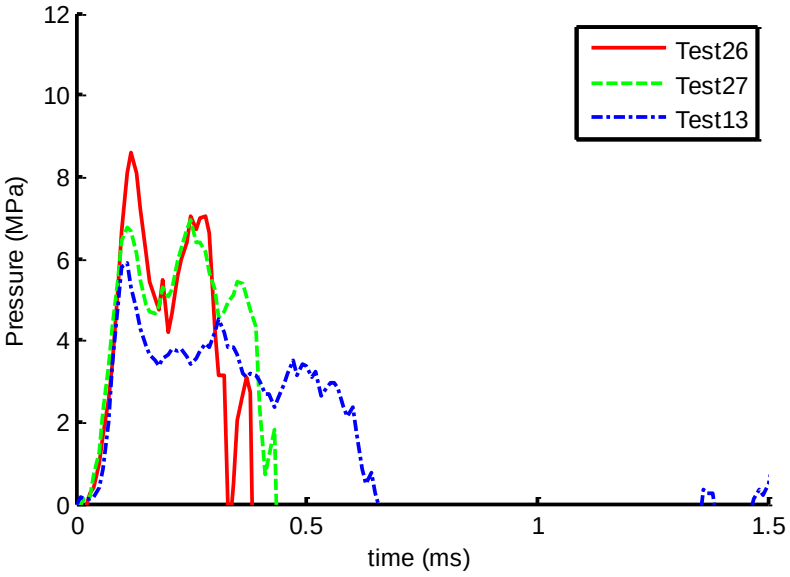

Figure 10. Pressure history for 160 kg/m^3 projectile at 30.5 m/s

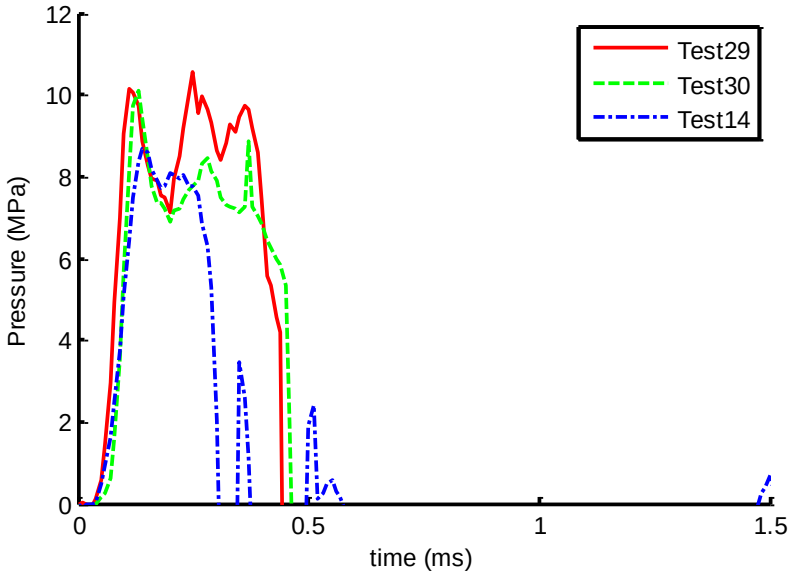

Figure 11. Pressure history for 240 kg/m^3 projectile at 30.5 m/s

Projectile Redesign

Some difficulties were found with use of the initial projectile design. Locations of initial failure on the foam tended to be unpredictable. Failure would begin in the front for some, as was desired, and some would fail towards the rear of the foam. Pressure pulses produced by the higher density foams tended to be shorter, more erratic in shape when comparing multiple tests, and overall not producing the desired "progressive crushing" behavior which would provide longer pulses. This problem was solved by introducing "triggers" to control the crushing of the projectile: 6 holes radially-oriented of depth 12.7 mm and diameters of 6.35 mm arranged equally-spaced around side of projectile, located 25.4 mm from the front face, as shown in Fig. 12. Failure would

initiate at these triggers and propagate from the front to the rear of the length of foam. There was also the possibility that the crushing of the earlier projectile design did not exhaust enough momentum to fully stop the flight of the aluminum mass mounted at the end of the projectile, thereby allowing the undesired possibility of the mass of striking the desired targets. It was important to prevent the aluminum mass from directly striking and exciting failure in any test specimens. To prevent this, the length of crushable foam on the projectile was extended to 139.7 mm, which would also create a longer pressure pulse. Fig. 12 illustrates the final projectile design. Fig. 13 illustrates the behavior of the final design observed by high speed video as it imparts and crushes onto a force-measuring apparatus

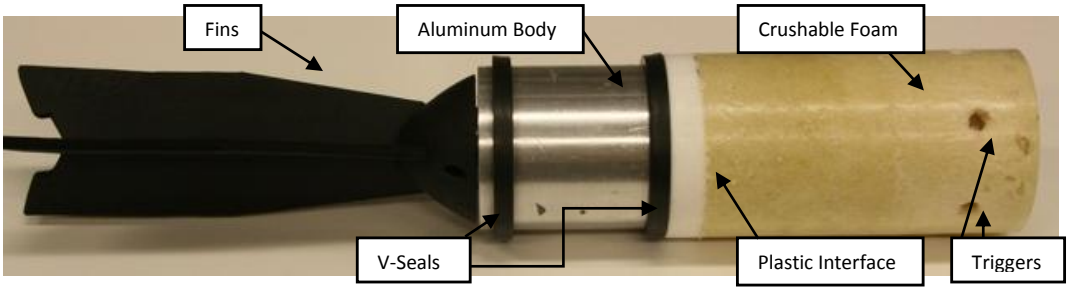

Figure 12. Final design of PPGP

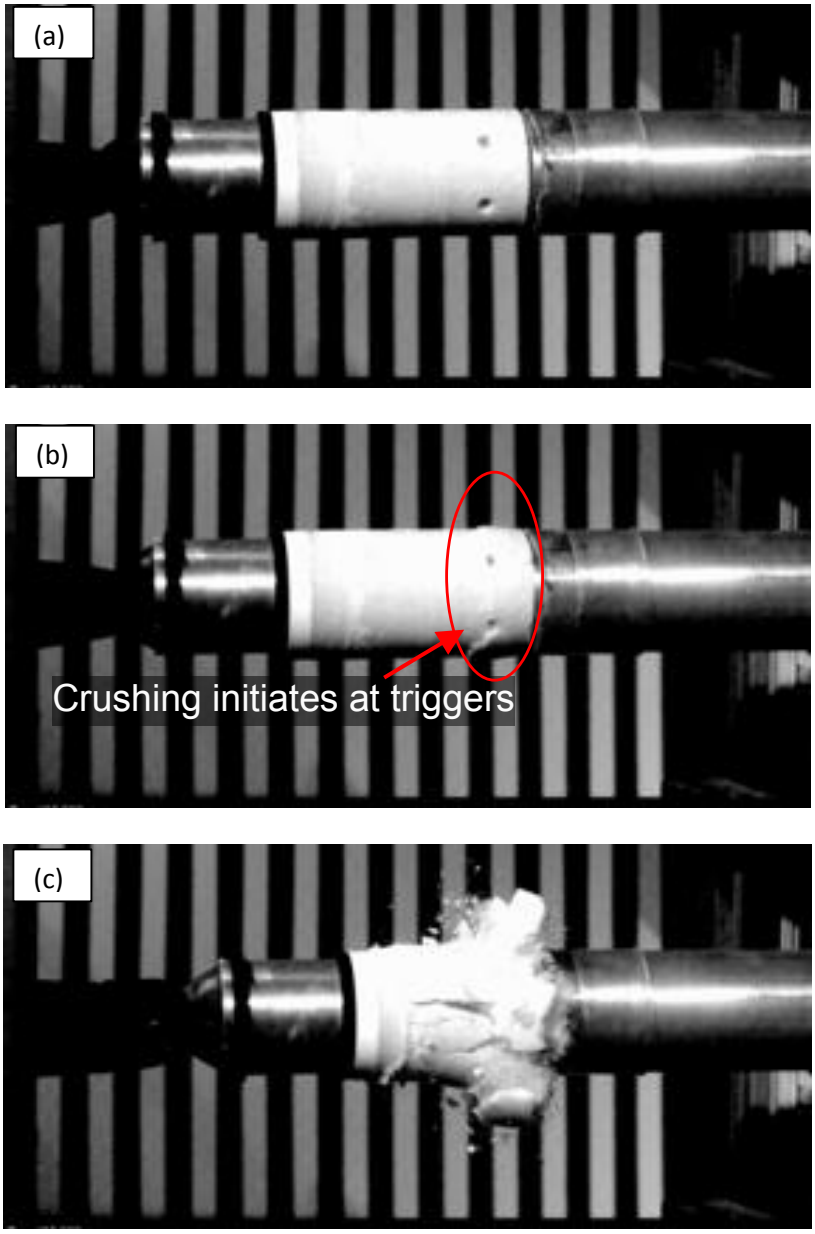

Figure 13. 160 kg/m^3 density projectile impacting FMB at 38.1 m/s

The final projectile design was observed to consistently to achieve stable flight and accurate targeting (see Fig. 13a). Crushing initiates at the triggers, and failure of the projectile propagates from the triggers to the rear (see Fig. 13b). Full stopping of the projectile projectile's momentum is transferred and the aluminum mass does not strike the target (see Fig. 13c). Lengthening of the projectile resulted in a longer pressure pulse

(results shown in Ch. 3) with a sharp peak pressure at the front matching those from the previous design, followed by a long overpressure tail at the end. This basic pulse shape was repeatable from test to test with much less variation compared to the earlier projectile having no triggers.

Higher Peak Pressure Projectiles

Additional tuning of the pressure pulse, particularly increasing the initial peak pressure was explored by using a higher density material fitted onto the front end of the PPGP. This was investigated using two materials. Tests were first performed using the same castable urethane plastic used to construct the foam-aluminum interface section of the projectile, also applied as a layer at the front face (see Fig. 14). A 19 mm thick layer of the plastic (density ~1050 kg/m^3) was mixed and poured into the three piece PPGP mold. When the plastic was fully cured, foam was poured and cast on top of it creating a 121 mm foam body and the same plastic-aluminum interface backing as before. The placement of the trigger holes were moved back to 50.8 mm from the front face due to the introduction of the hard plastic. The urethane plastic would shatter upon impact creating higher peak pressures compared to the foam alone (see Fig. 15).

Figure 14. Plastic Front Projectile

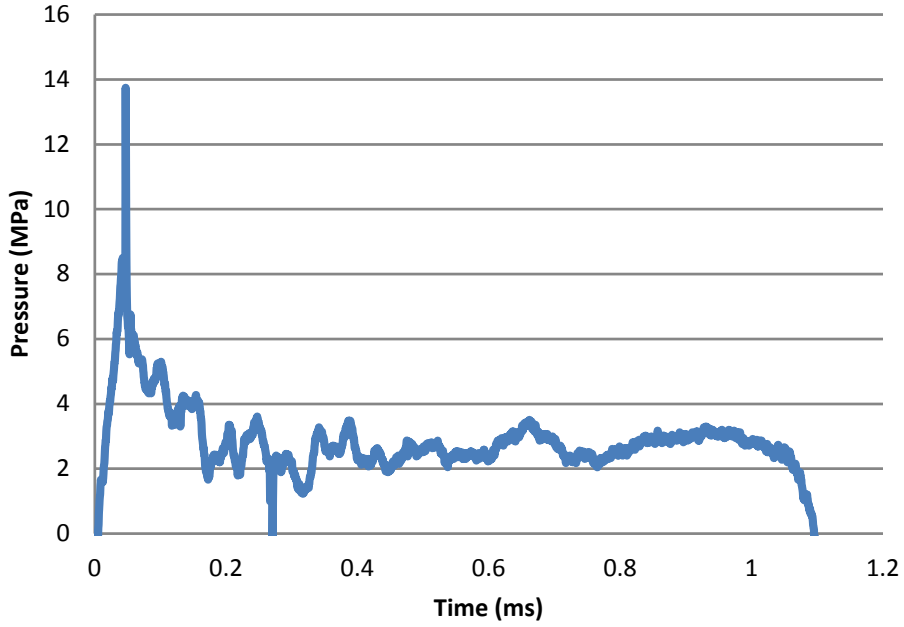

Figure 15. Plastic front projectile at 30.5 m/s

A second front face material was tested with using urethane rubber mixed with steel shot (see Fig. 16). This could create a higher density flexible material, about 1240 kg/m^3, capable of reaching higher peak pressures with a less dramatic rise compared to those from the plastic front projectiles.

Figure 16. Steel shot rubber front projectile

CHAPTER 3 EXPERIMENTAL APPARATUS AND PPGP RESULTS

Gas Gun

The PPGPs were launched using the gas gun test setup shown in Fig. 17. This gun has a 79 mm inner diameter bore, 2.29 m long barrel, and is capable of firing up to 79 mm diameter projectiles to velocities in excess of 200 m/s. The gas gun is powered by bottled nitrogen gas that pressurizes a tank connected to the breach end of the barrel. The tank pressure is released into the breach of the gun via a fast-opening valve actuated with helium gas. The projectile passes through a velocity measuring system composed of two laser photogates prior to impacting the target of interest.

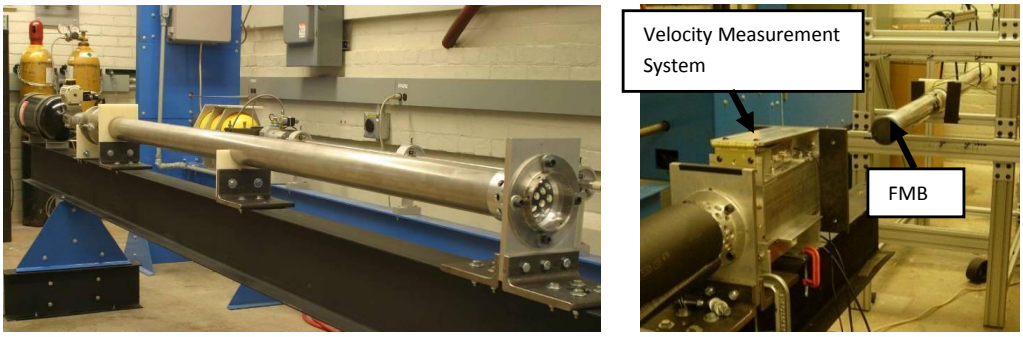

Figure 17. Gas gun and force measurement bar setup

PPGP Pressure versus Time Measurements

Pressure pulses produced by the PPGP were measured by a dynamic force measurement bar (FMB). This apparatus (see Fig. 18) consists of a 3.5 m long hollow aluminum bar of 76.2 mm inner diameter and 63.5 outer diameter having a 25.4 mm thick end-cap onto which the PPGP impacts. Stress waves travelling down the bar are measured by two strain gages located 457 mm from the end cap and placed on opposite sides of the bar. From these dynamic strain measurements, the applied pressure (force) pulse can be determined via elastic stress-strain relationship. Note that the FMB has measurement duration limit of 1.1 ms due to the time for an axial stress wave to travel to the far end of the bar and return to the strain gage location. A Vishay 2310B strain signal conditioner is used for the strain gage excitation and signal amplification (10x gain and 10 volt excitation). A Picoscope 3424 12-bit digital oscilloscope was used for high speed data acquisition. For visual observation of the projectile's behavior, a Phantom V7.3 high speed camera was used to record the projectile in flight and during the impact event at a frame rate of up to 14,000 frames per second.

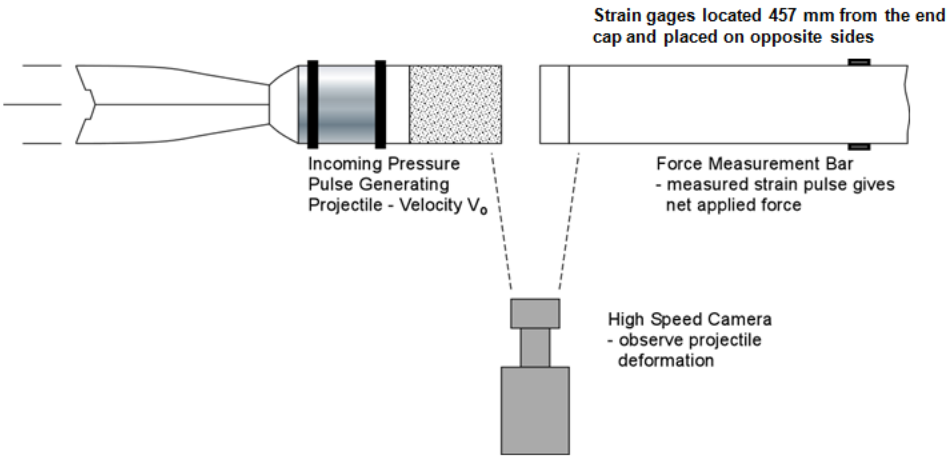

Figure 18. FMB test setup

Projectiles were fired at speeds of 38.1 to 42.7 m/s with gun pressures of 517 to 689 kPa respectively. Pressure pulses consisted of a sharp rise to a peak pressure followed by a long overpressure tail. This basic shape was highly repeatable from test to test for each foam density. Fig. 19 displays the FMB data measured from projectiles representative of the three densities used. Note that data after 1.1 ms must be ignored since the timing corresponds to when the return pulse arrives at the strain gage location. As shown by the data plotted in Fig. 18, the pressure pulse shape is directly affected by the foam density, with higher peak pressure created by higher foam densities.

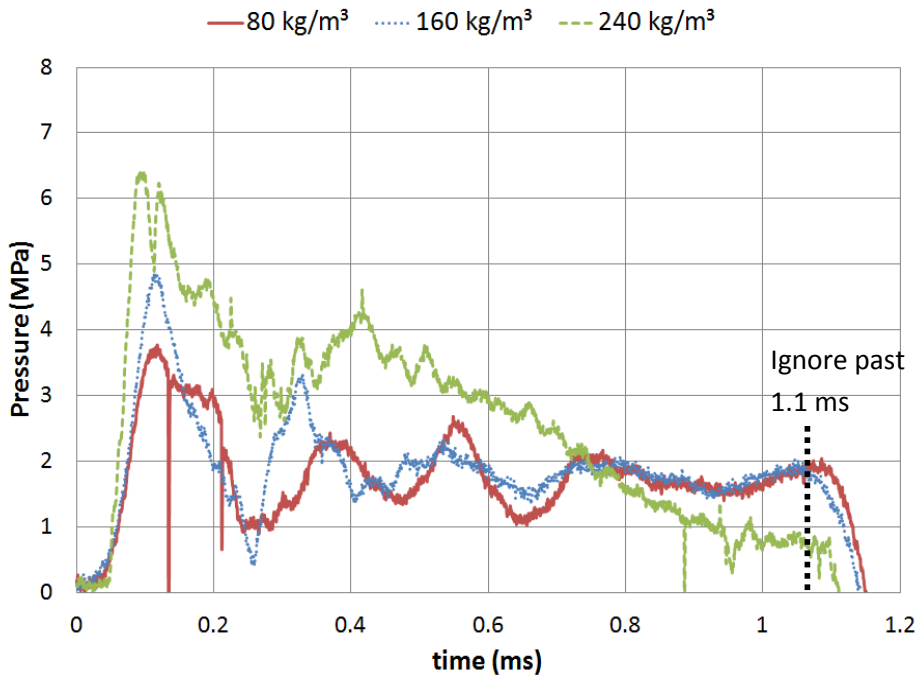

Figure 19. FMB measurements of three foam densities; 38.1 m/s

The projectiles produced pressure pulses for all three foams exceeding the measurement duration capability of the FMB. To alleviate this problem, the FMB tests were supplemented with impacts onto a Dytran 1060V5 dynamic piezoelectric-based force sensor used in place of the FMB. The test setup is shown in Fig. 20. The force sensor is attached to a heavy steel base plate and the PPGP is fired at a 76.2 mm diameter, 25.4 mm thick aluminum alloy end-cap attached to the face of the force sensor.

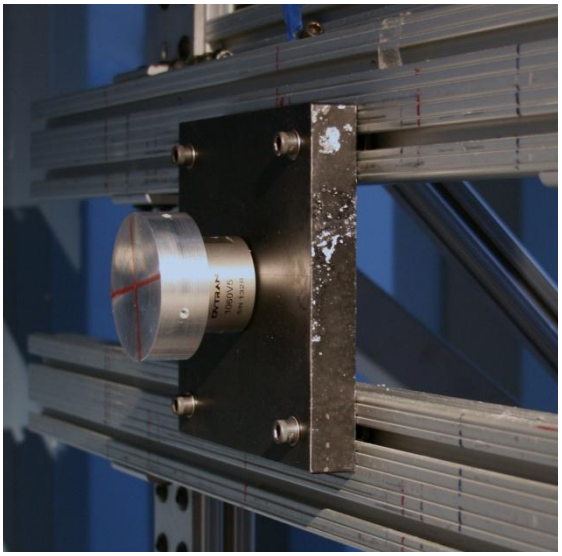

Figure 20. Force cell setup

The piezoelectric force cell based measurement of pressure pulses for projectiles of each density is shown in Fig. 21. Visible in this figure is a large amount of ringing in the pressure history measurement which is caused by high frequency ringing effects of the system that diminish after 1 ms. Due to this ringing a hybrid pressure history plot of the FMB (before 1 ms) and piezoelectric-based load cell measurements (after 1 ms) was created, as shown in Fig. 21. Note that these are averages of several representative tests combined into single trendlines and also that the pressure drops to zero by 5 ms for all densities. The peak pressures for all tests, plotted in Fig. 23, show that the peak pressures produced are fairly repeatable from test to test and that the peak pressure is linearly related to the foam density (over the range tested). The total impulse (integration of force vs. time from 0 to 5 ms) of the combined measured pressure pulses reveals a strong increase with higher foam density as shown in Fig. 24.

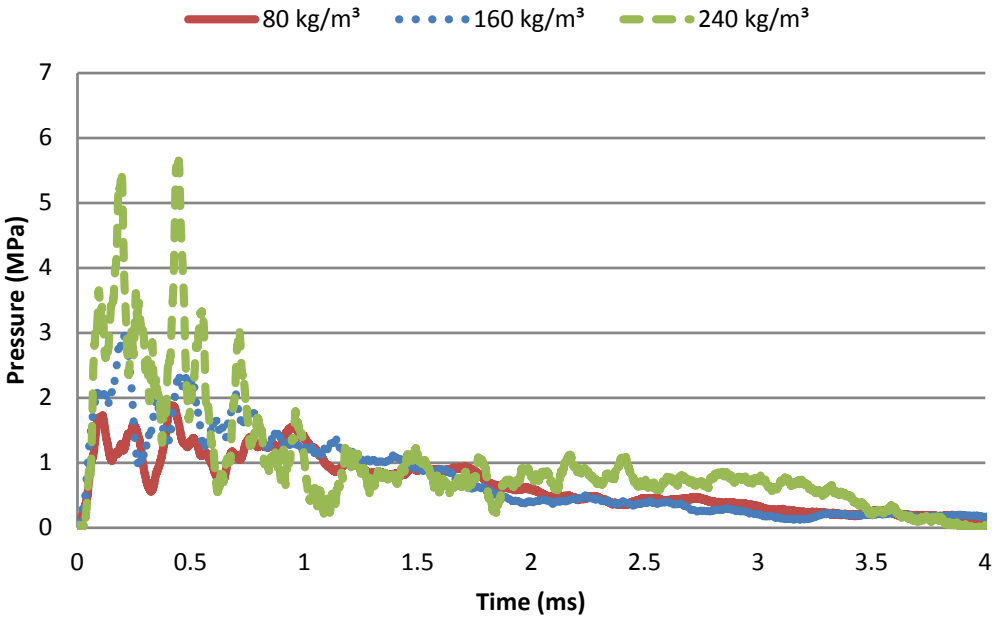

Figure 21. Piezoelectric force cell measurement of pressure history; impacts at 38.1 m/s

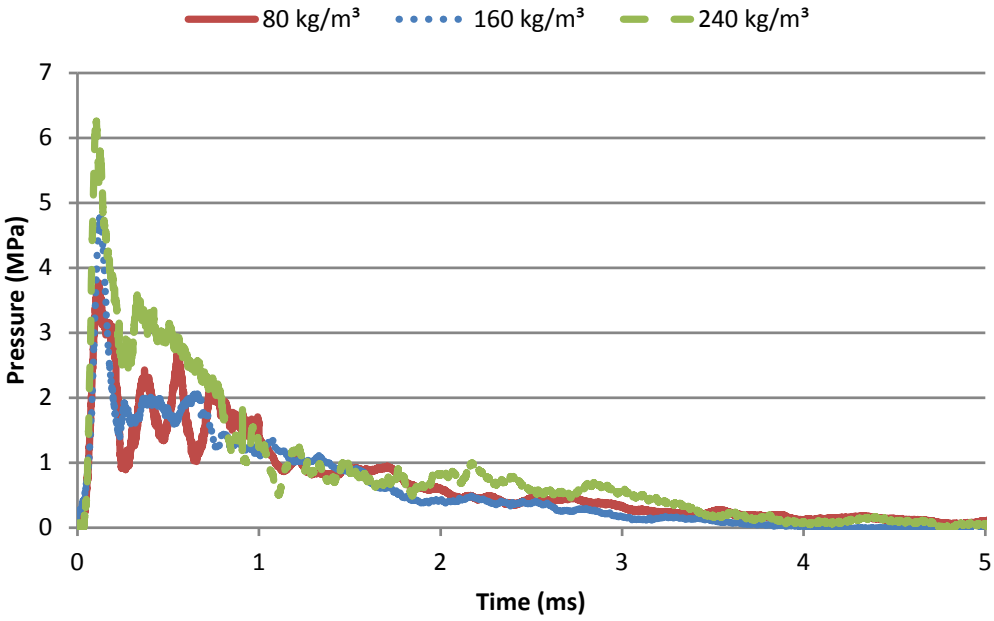

Figure 22. Full pressure history hybrid measurement of three foam densities; impacts at 38.1 m/s

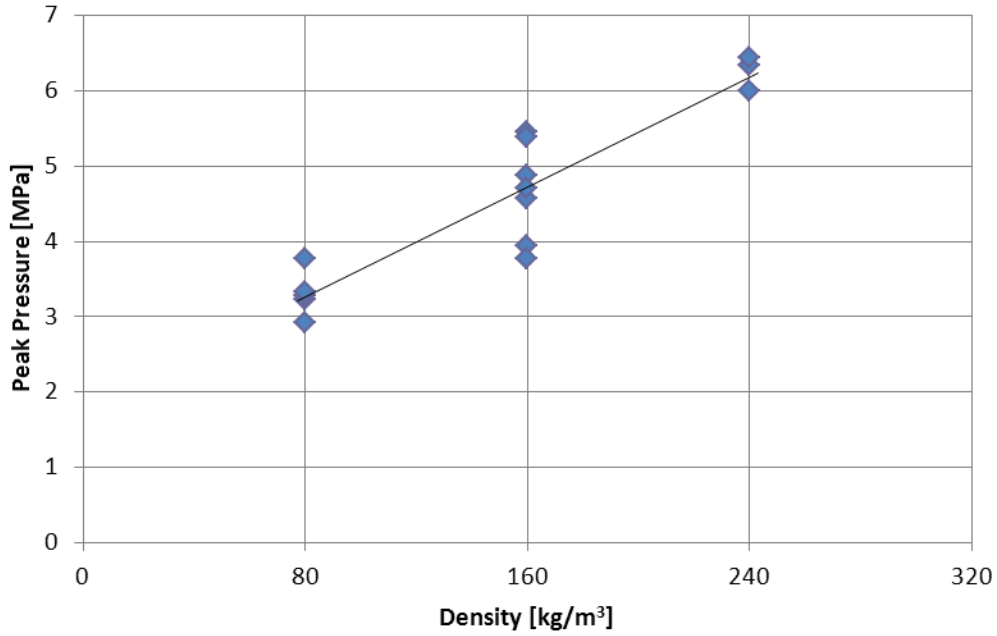

Figure 23. Plot of peak pressure versus foam density; impact at 38.1 m/s

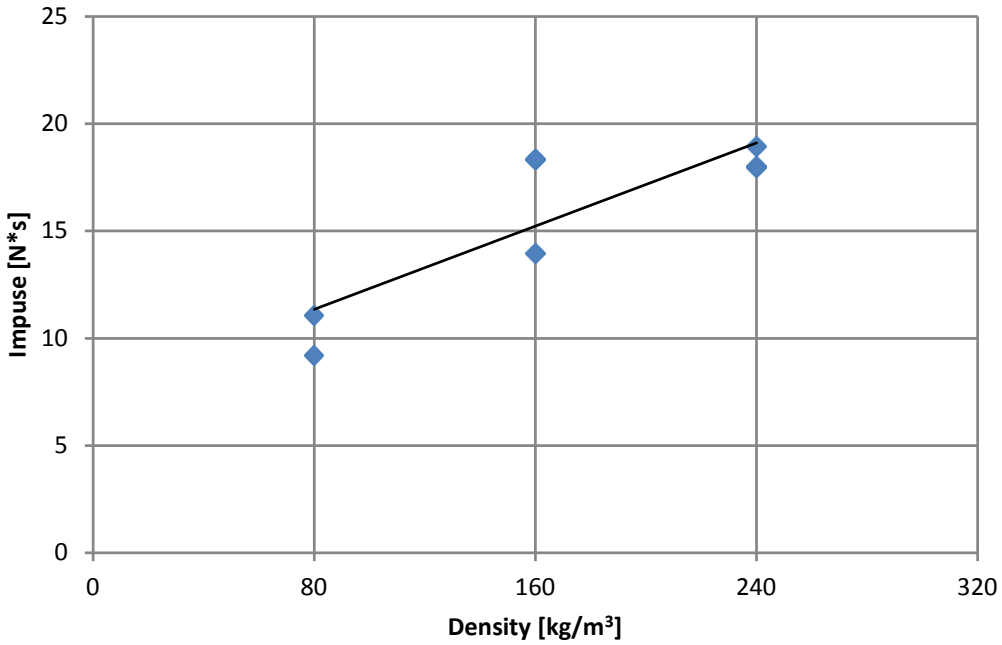

Figure 24. Plot of total impulse versus foam density; impact at 38.1 m/s

Impacting projectiles at higher velocities resulted in higher peak pressures with roughly the same post-peak pressure level, as shown in Fig. 25. The figure shows the pressure time histories of two 160 kg/m^3 projectiles. One was fired at 42.7 m/s using a gun reservoir pressure of 689 kPa and the other was fired at 50 m/s using a pressure of 1,034 kPa. The same effect was seen in the foam compression tests where the tests conducted at a higher speed exhibited higher yield stresses. The loading ramp-up to peak pressure, however, appeared rate independent. Fig. 25 clearly demonstrates that projectile speed has a strong influence over creating more intense pressure peaks, i.e., a strong dynamic effect exists. Higher velocities are avoided, however, since the foam can completely crush down and the aluminum body then impacts the target of interest with considerable residual velocity. This issue can be addressed, in part, by using a longer crushing foam front. Such modifications were not investigated within the project activities reported on.

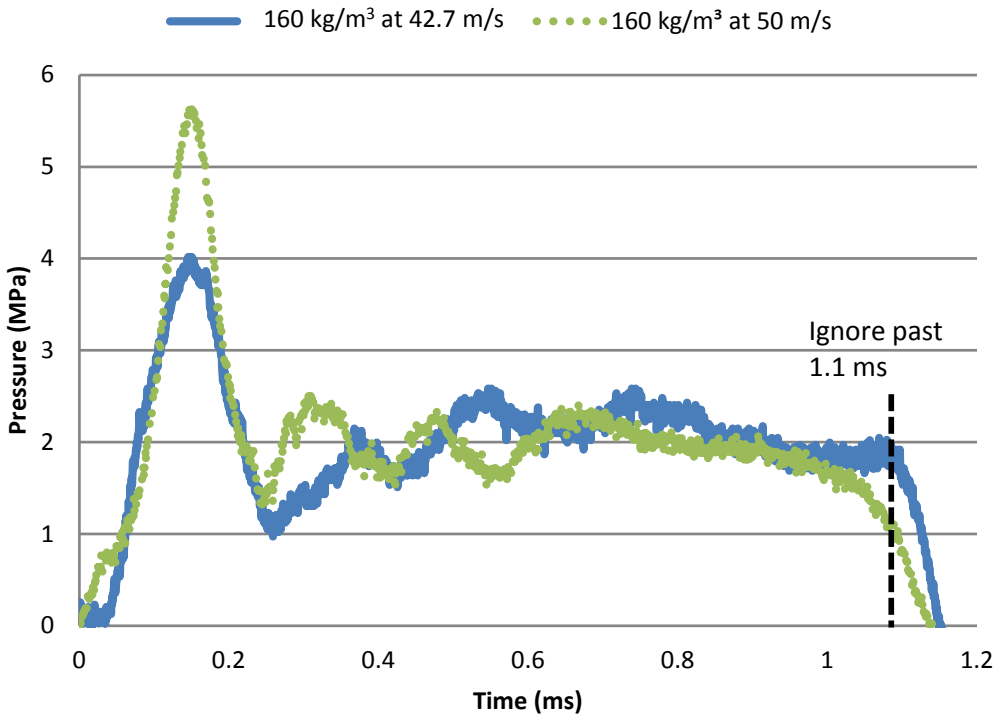

Figure 25. 160 kg/m^3 foam projectile launched at 42.7 m/s and 50 m/s

CHAPTER 4 COMPOSITE FACESHEET BEAM TESTS

While the aim of this project is to understand the failure behavior of sandwich panels composed of carbon/epoxy laminate facesheets and an end-grain balsa core, the bending behavior of the facesheets, in isolation of core failure effects subjected to dynamic three-point bending, was first studied. Dynamic testing was conducted using the previously described PPGP to impart a known artificial explosive pressure pulse onto beam specimens. These tests were supplemented by slower, more controlled dynamic tests (intermediate speed), as well as quasi-static tests to obtain more detailed observations of the specimens' behavior during the failure process.

Test Specimens

Sandwich specimens of interest consisted of a 3.175 mm facesheet that located on one side of the 76.2 mm thick end-grain balsa core, and a 12.7 mm facesheet on the other. A stack of these panels is shown in Fig. 26. The facesheeets were composed of a high-strength carbon fiber (Toray T700) in woven form impregnated with vinylester resin via a vacuum assisted resin transfer molding (VARTM) process. The facesheets were a quasi-isotropic type layup composed of a combination of woven 0/90, +/-45 layers, and a top ply of stainless steel mesh to provide EMF shielding.

Figure 26. Carbon/epoxy balsa core sandwich panel specimens

To study the facesheet bending failure, beams were constructed using the thicker 12.7 mm facesheets. These were first cut into 76 by 305 mm beam specimens. The balsa wood was then removed carefully over areas where contact is made with test fixtures and at locations of the strain gages (see Fig. 27). The top face of the specimen and side facing the camera were painted white to better view initial and progressive failure of the plies (see Fig. 28). To record strain data, 350 Ω strain gages (Vishay L2A-06-250LW-350 for earlier tests, then TML FLA-6-350-1L for later tests) were placed at the midspan of the beam as well 38.1 mm away from the midspan corresponding to the PPGP radius (see Fig. 27).

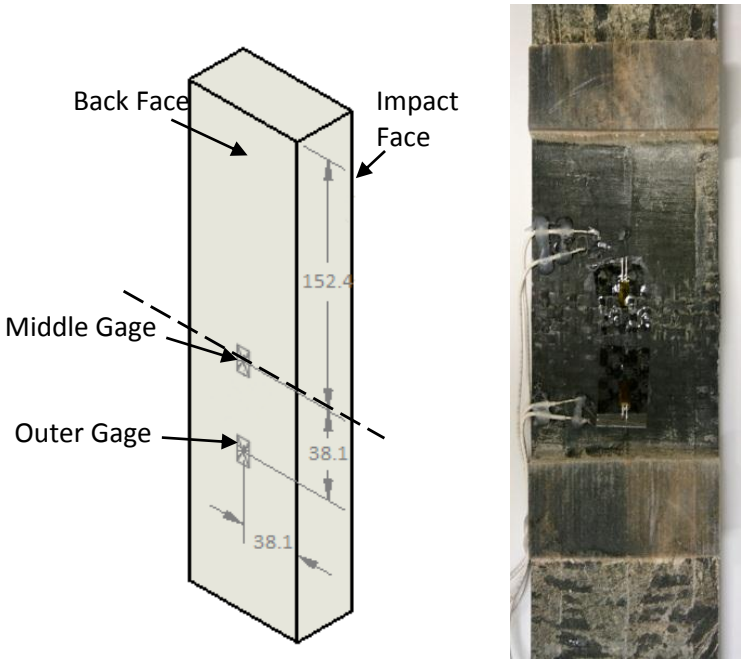

Figure 27. Facesheet beam specimen strain gage placement

High Speed Dynamic Tests

Material properties of the carbon/epoxy laminate facesheets and full sandwich beams were determined through study of three point bending behavior. High speed dynamic tests were conducted using the PPGP to impart dynamic loading on the beams. It is assumed that the loading on the specimen is the same as the pressure pulse history produced by the PPGP impacting the FMB. This assumption is based on numerical analyses conducted of a soft elasto-plastic projectile impacting a rigid surface, a stiff plate, and a flexible plate, with the results showing the contact force that develops is nearly the same. This analysis was not part of this thesis work and is thus provided in Appendix VIII.

To load the beam targets, a 160 kg/m^3 foam projectile is used. This is fired at 517 kPa, producing a speed of 42.7 m/s. The beams were mounted using steel "v-block" supports (see Fig. 28) to hold the beams in place and provide simply supported boundary condition. Two Vishay 2310B high speed strain signal conditioners were used for strain gage excitation and signal amplification. A Picoscope 3424 12-bit digital 4-channel oscilloscope is used for data acquisition. Beams were supported with a span of 267 mm, with the PPGP being fired directly at the midpoint of the beam. The experiments were visually observed with a Phantom v7.3 high speed video camera at frame rates up to 14,000 frames per second. The deflection history of the beams was then calculated from the high speed video using the Phantom camera software (version 675) measurement capabilities.

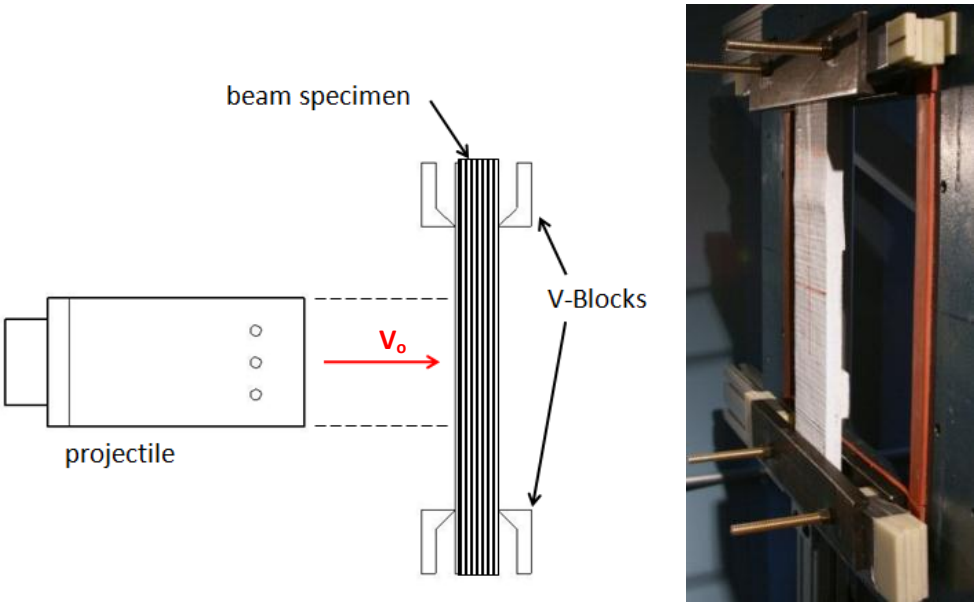

Figure 28. High speed dynamic test setup for facesheet beams

Quasi-static and Intermediate Speed Tests

To supplement the data from the beam impact tests, quasi-static bending tests were conducted on specimens of the same 12.7 mm facesheet beam geometry. This provided the ability to carefully observe and better resolve strain, deflection, and locations of damage as the specimens undergo failure, as well as the ability to directly measure the applied force. The specimens were tested using a servohydraulic 100 kN capacity MTS 810 material test system (uniaxial tension/compression test machine)**.** A fixture was machined to create a simply supported boundary condition. Like the impact tests, the specimens were simply-supported at both ends with a 267 mm span with two 19.05 mm diameter steel rollers (see Fig. 29).

To simulate loading conditions similar to the dynamic PPGP impact tests, a 76.2 mm diameter cylinder of hard rubber foam was used to impart a distributed pressure load at the center of the specimen as the test machine actuator pushed the beam's outer simple supports upwards. Tests were conducted at speeds of 8.33×10^{-5} m/s to observe the progression of damage of the specimens in quasi-static loading and at 0.25 m/s (intermediate speed) to test the specimens under more dynamic loading conditions similar to the dynamic gas gun tests. For these tests, Encore Model 663 strain signal conditioners were used for strain gage excitation and signal amplification. Strain gages were placed in the same locations as in the high speed PPGP tests. A laser extensometer was used to record beam center displacement data during the quasi-static tests.

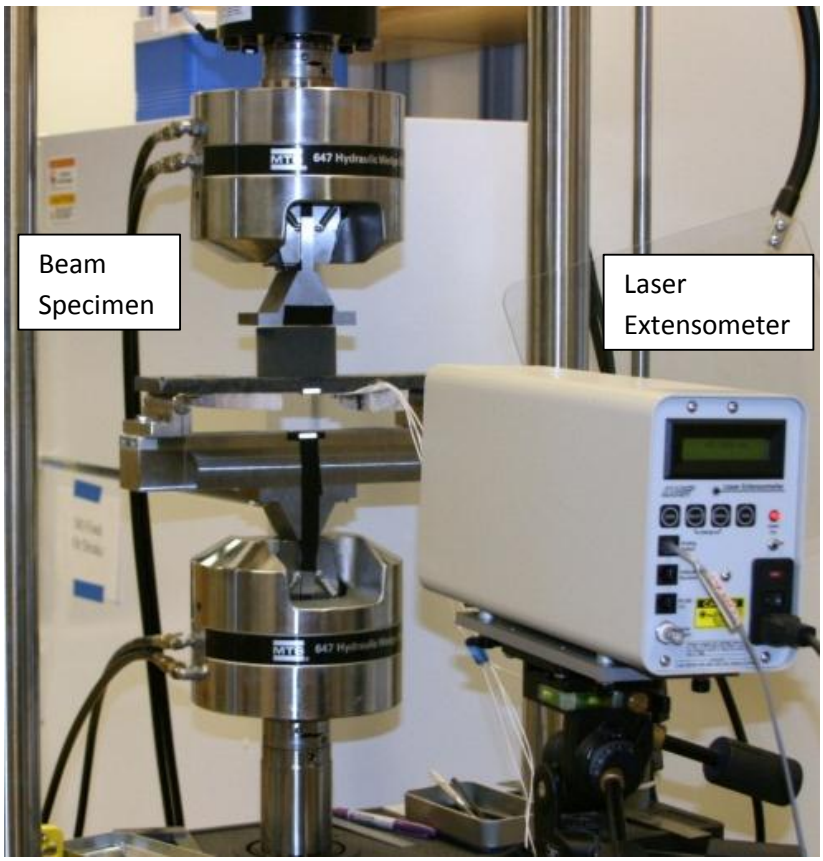

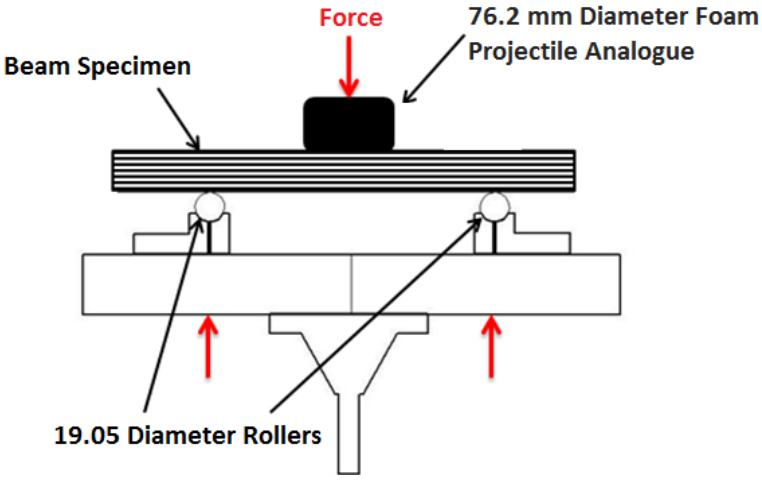

Figure 29. Intermediate and quasi-static test setup for facesheet beams

Results

Dynamic tests began with exploring the extent of damage which could be produced by firing the PPGP at uninstrumented 12.7 mm thick carbon fiber facesheet beams. The compressive strength of composites is typically lower than the tensile strength, and thus initial failures were observed to occur on the impact face of the beam in the vicinity of the impact location. Firing the 160 kg/m^3 projectiles at 42.7 m/s at the beams caused visible surface cracks as well as visible delamination of the surface ply. A slightly raised surface was also visible at the impact face, which is typical of compressive failure in fiber-reinforced composites due to the presence of delamination (see Fig. 30a). Firing a higher density projectile (240 kg/m^3) at the same velocity created a greater amount of damage, including visible frontside compressive fiber failure as well as significant delamination of multiple plies through the laminate thickness, as shown in Fig. 30b.

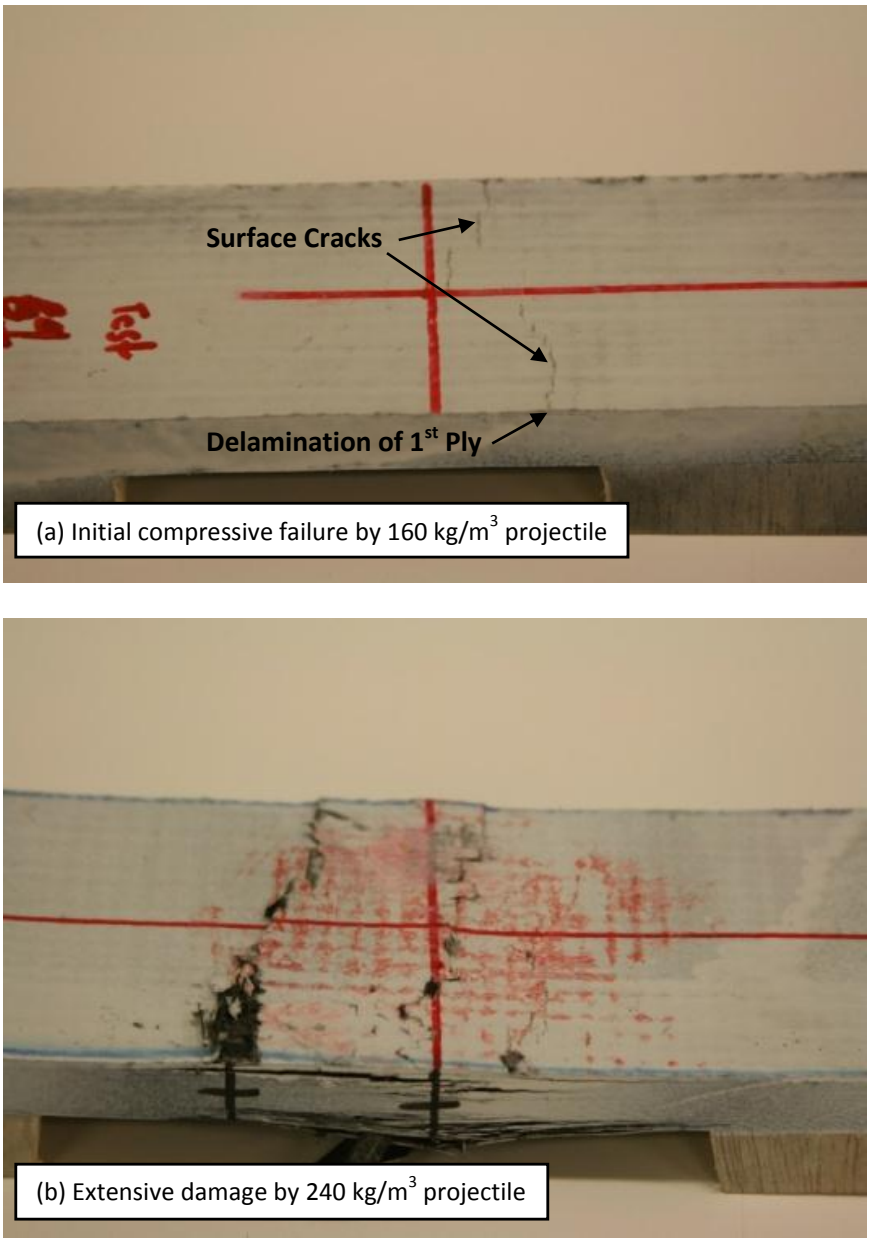

Figure 30. Typical damage caused by 160 and 240 kg/m^3 projectile

Viewing the high speed video footage of dynamic tests clearly illustrates the progressive failure process of the beams. Fig. 31 shows the oblique side view of an impact test and details the sequence of events leading to failure. Failure begins at the front (impact) side of the beam (Fig. 31b) soon after the PPGP comes into contact due to

compressive bending stress. Cracking and delamination then progresses from the front side through the thickness of the beam to the midplane (Fig. 31c) before backside tensile failure occurs (Fig. 31d).

Figs. 32 and 33 illustrate the similar behavior for the quasi-static and intermediate speed tests, respectively. Viewing the video documentation for these slower tests provides the ability to view the failure behavior of the beam much more carefully and in much higher detail. Again, failure initiates where the hard rubber foam loading point contacts the beam specimen causing compressive failure on the front face of the beam. Failure then progresses towards the midplane of the beam. Once the midplane is reached, backside tensile failure immediately follows.

Strain data are plotted against time as well as displacement in Figs. 34-36. These are representative of each test speed. Also shown are the locations of each time step illustrated in Figs. 31-33 in the corresponding strain curves. Of note here is the behavior of the beams as they approach failure. For the dynamic tests (i.e. gas gun impact and intermediate speed) the events of failure occur continuously. Compressive failure first occurs. Cracking and delamination propagate down to the midplane, and at this point a plastic hinge begins to form causing the outer gage strain curve to plateau (i.e. roughly constant value). Backside tensile failure follows, a plastic hinge is fully formed, and the strain recorded on the outer gage will drop. This event causes the middle gage to fail. For the quasi-static tests, some initial delamination and cracks of the surface plies will form with no detectable indications in the strain curves. After some time, further

compressive failure will appear. This happens as one quick continuous event. Cracking and delamination will propagate down to the midplane. The outer gage will then plateau, followed by backside tensile failure and the outer gage dropping. This event is much less dramatic for the quasi-static tests and the middle gage will continue to record strain past tensile failure.

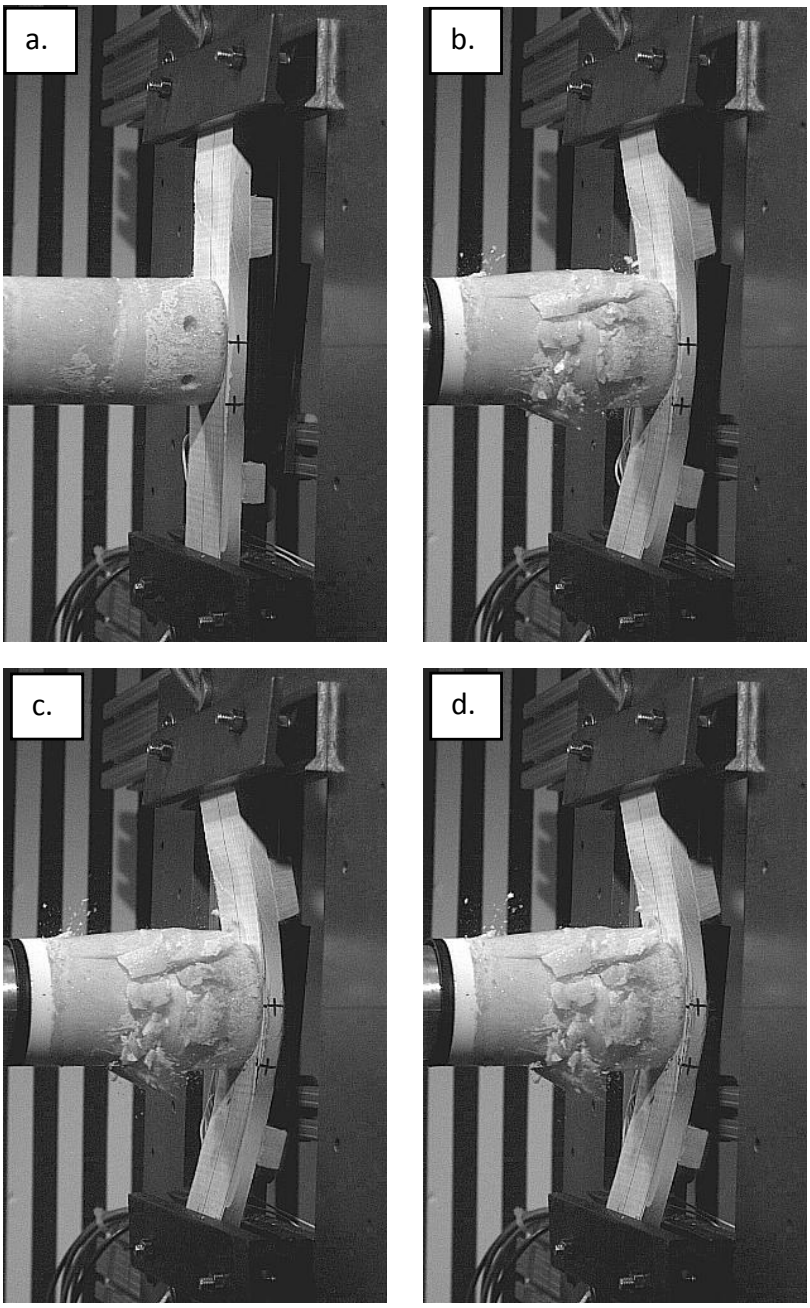

Figure 31. Progressive failure in dynamic thick beam impact test; 160 kg/m^3 PPGP at 42.7 m/s; (a) t = 0 ms, first contact, (b) t = 0.712 ms, initial compressive failure, (c) t = 0.855 ms failure propagates to midthickness, (d) t = 0.926 ms backside fiber failure

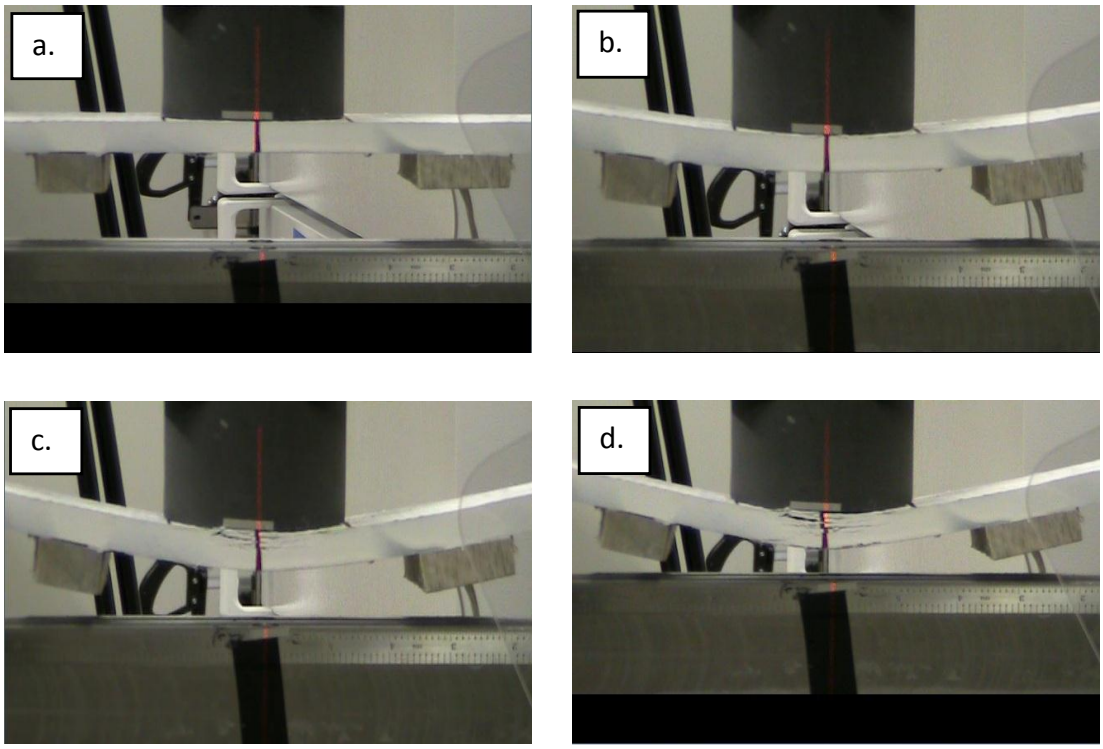

Figure 32. Progressive failure in quasi-static thick beam test; hard rubber indentor at 8.33 x 10^{-5} m/s displacement rate; (a) t = 0 sec, actuator comes into contact with the beam specimen, (b) t = 100 sec, initial compressive failure, (c) t = 170 sec, cracks propagate to mid-plane of the specimen , (d) t = 230 sec, backside fiber failure

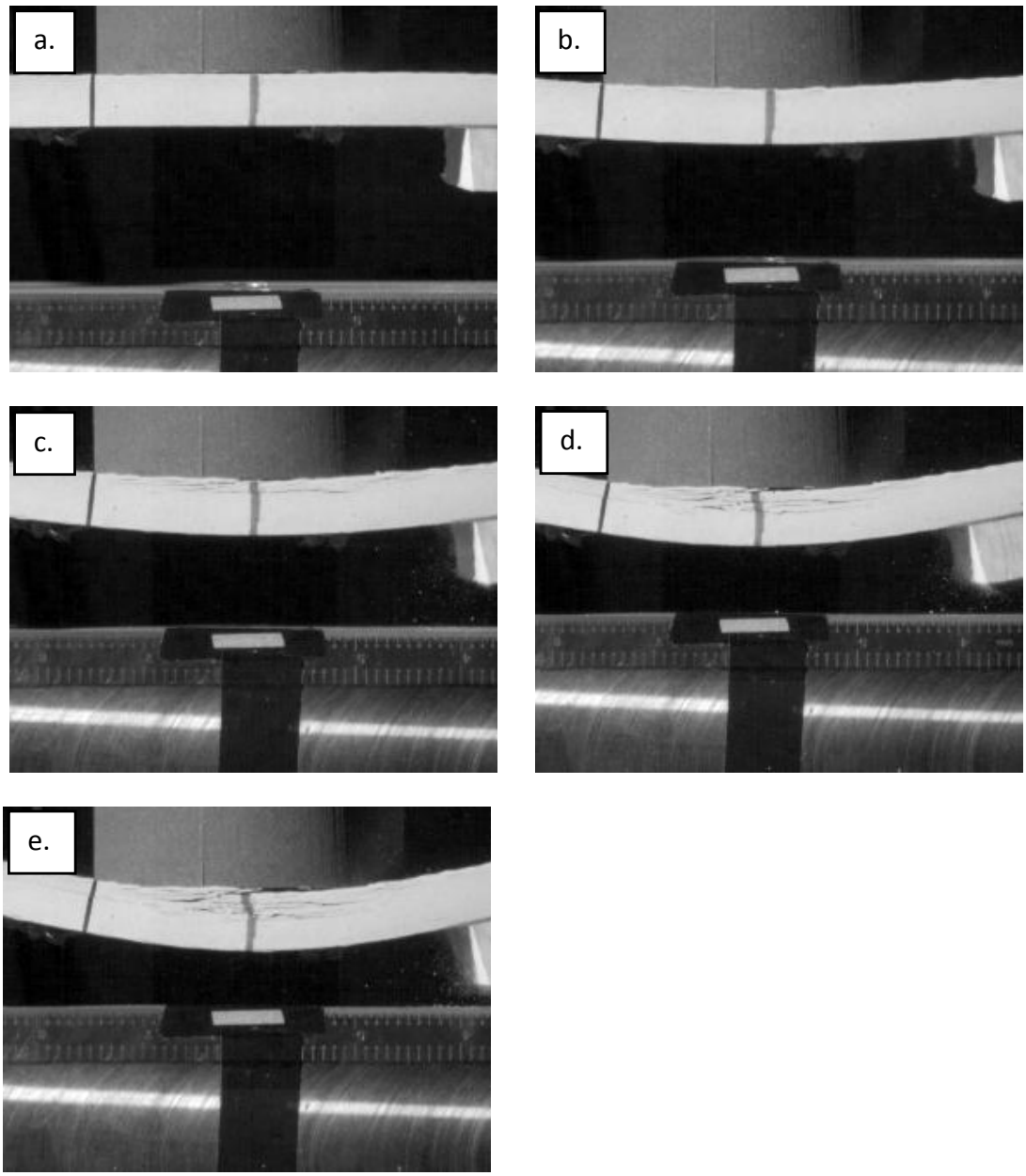

Figure 33. Progressive failure in intermediate speed thick beam test; hard rubber indentor at 0.25 m/s loading rate; (a) t = 0 ms actuator comes into contact with beam specimen, (b) t = 58 ms initial compressive failure, (c) t = 80 ms, progressive delamination, (d) t = 100 ms, progressive delamination reaches midthickness, (e) t = 115 ms, backside fiber failure

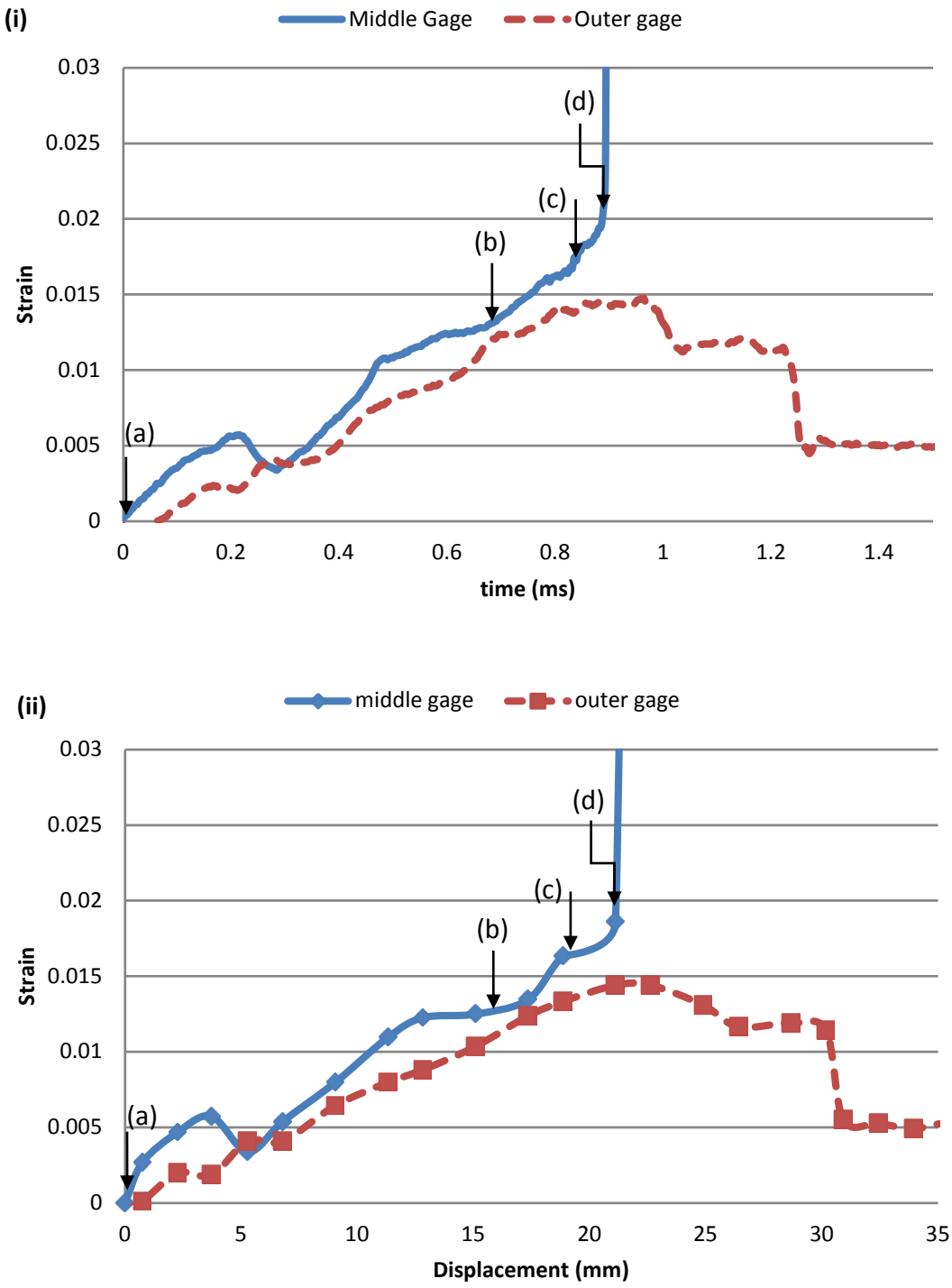

Figure 34. Progressive failure in dynamic thick beam impact test; 160 kg/m^3 PPGP at 42.7 m/s; (i) strain versus time, (ii) strain versus axial displacement; letters match images shown in Fig. 31

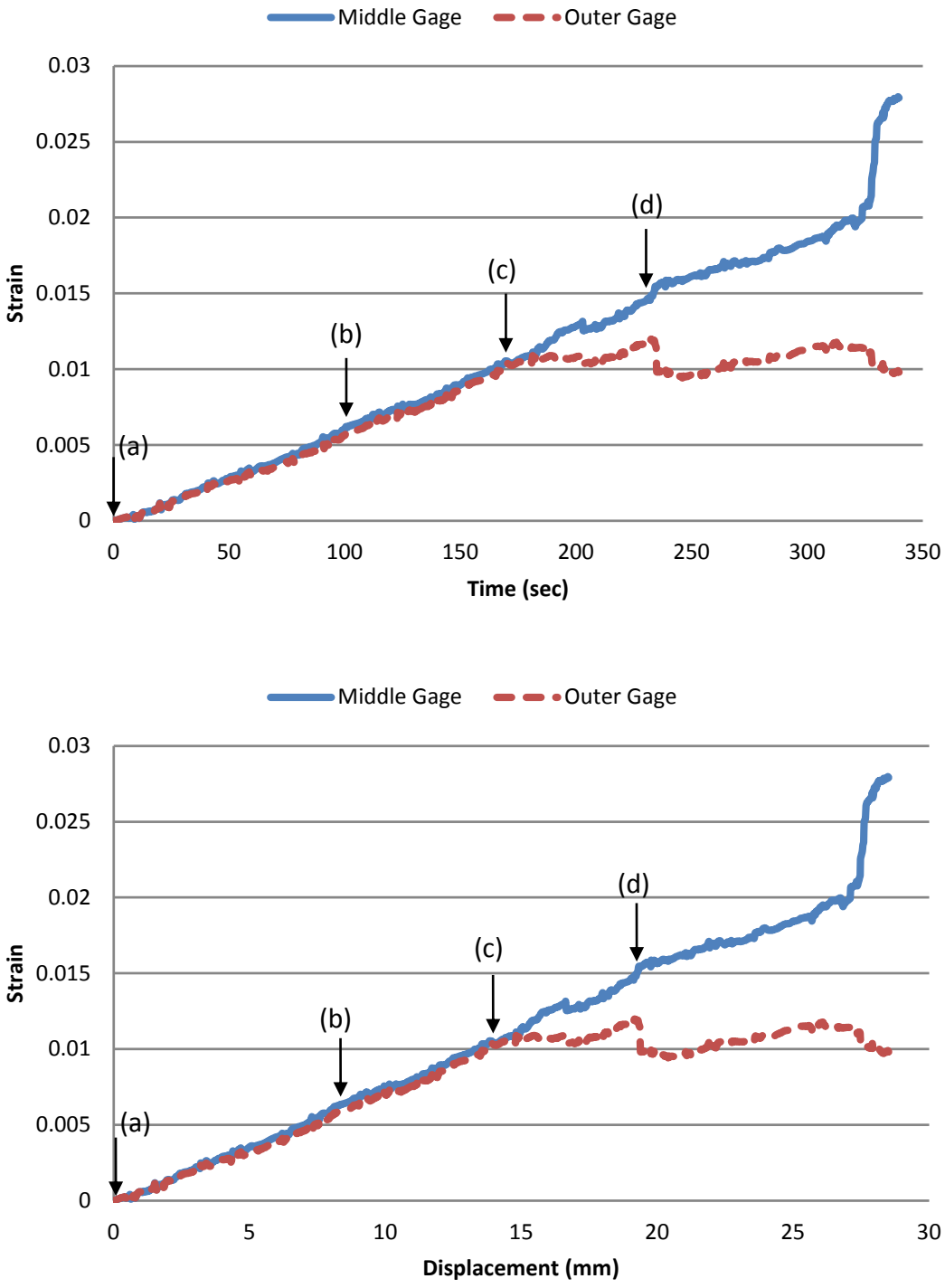

Figure 35. Progressive failure in quasi-static thick beam test; hard rubber indentor at 8.33 x 10^{-5} m/s loading rate; (i) strain versus time, (ii) strain versus axial displacement; letters match images shown in Fig. 32

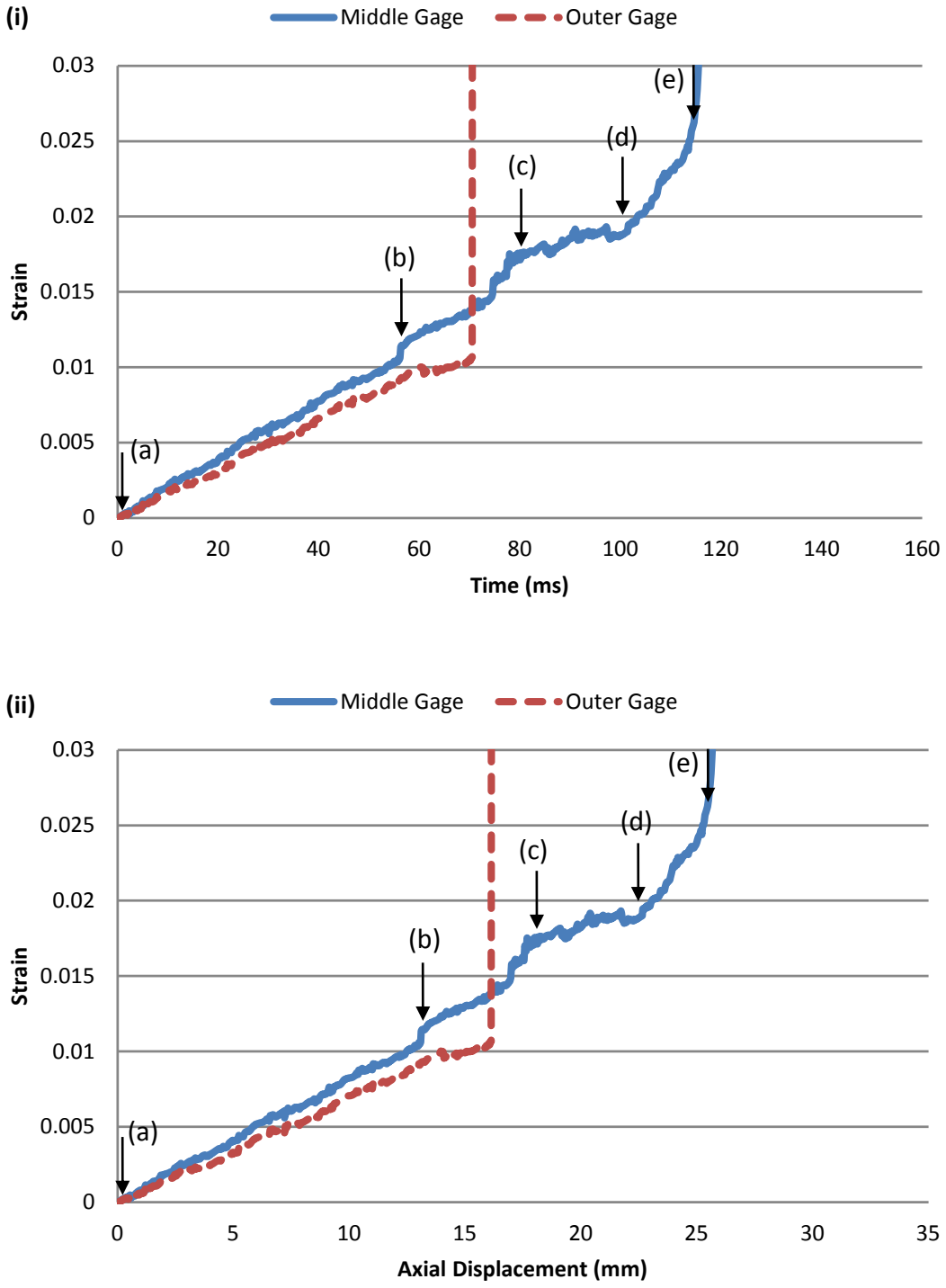

Figure 36. Progressive failure in intermediate speed thick beam test; hard rubber indentor at 0.25 m/s loading rate; (i) strain versus time, (ii) strain versus axial displacement; letters match images shown in Fig. 33

It should be noted that the video images and strain plots in Figs. 31-36 are representative examples of several tests repeating the same conditions. Tensile and compressive failure strain values were gathered from all these tests. Table 3 tabulates the failure strains and corresponding strain rates for each experiment at the initial compressive failure and tensile failure events. It was found that when comparing dynamic failures (high and intermediate speeds) to quasi-static failure, the specimens failed at significantly higher tensile strains (about 20-40% greater) and compressive failure strains (about 40-60% greater), showing that this material exhibits increasing failure strains for higher strain rates. Figures 37 and 38 plot compressive failure strain and tensile failure strain versus strain rate respectively.

Table 3. Strain rate and failure strain for three-point bend tests

Test ID*	Test Speed (s^{-1})	Compressive Failure Strain	Tensile Failure Strain
GG1	High, NA	NA	NA
GG2	High, 20.2	0.0138	0.0207
QS1	Low, 6.50E-05	NA	NA
QS2	Low, 6.57E-05	0.0057	0.0165
QS3	Low, 5.87E-05	0.0050	0.0148
QS4	Low, 6.08E-05	0.0063	0.0169
IS1	Intermediate, 0.181	NA	NA
IS2	Intermediate, 0.191	0.0106	0.0272

* GG = dynamic gas gun; IS = intermediate speed; QS = low speed quasi-static

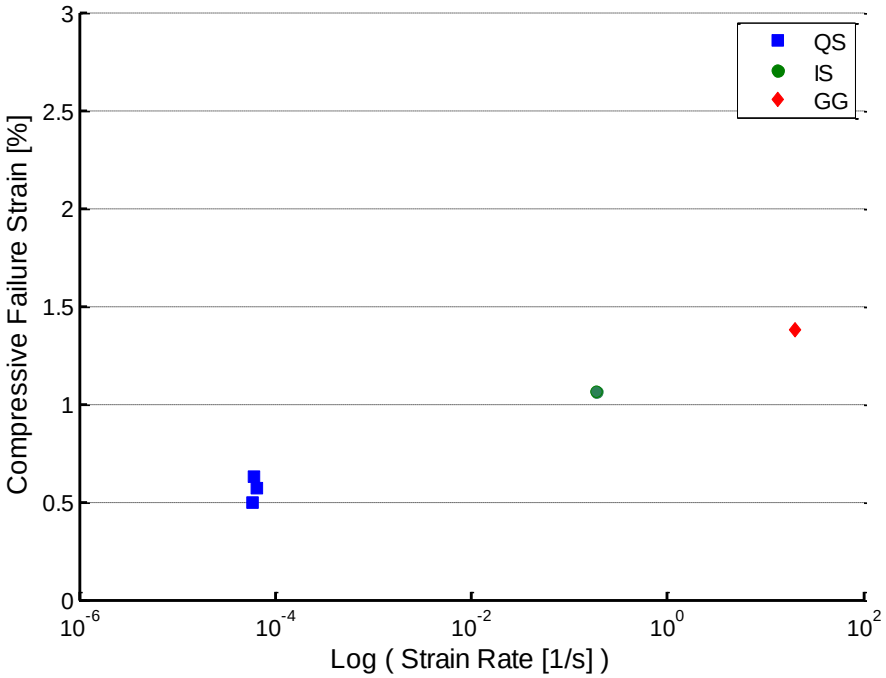

Figure 37. Compressive failure strain versus strain rate

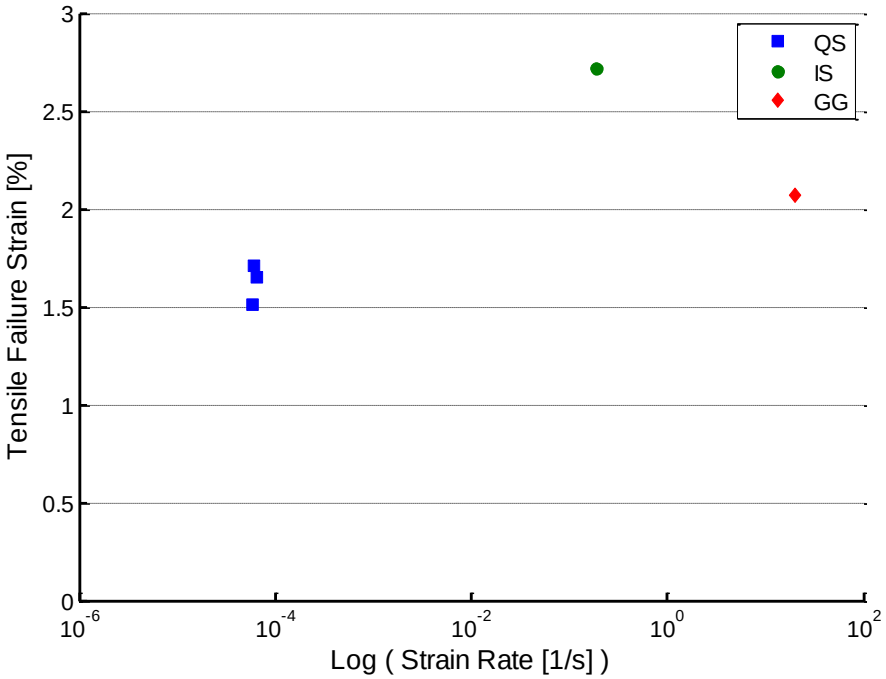

Figure 38. Tensile failure strain versus strain rate

Tensile Tests

Tensile tests were performed on the 3.175 mm thick facesheets of the sandwich specimens to directly measure laminate level material properties. Specimens were cut at 0, 45, and 90 degree orientations (see Fig. 39) into 203.2 mm by 25.4 mm specimens as specified in Fig. 40. 50.8 mm by 25.4 mm endtabs were also cut from the same material and ground to a low-angle taper using a handheld grinder. The endtabs were adhesively bonded to the ends of the tensile specimens so as to eliminate grip-induced stress concentrations in the specimens. The resulting stress versus strain curves are shown in Figs. 41-43. Young's modulus and tensile failure strains from these tests are summarized in Tables 4 and 5. The measure of tensile failure strains were in the same range as those recorded from the thick beam tests despite the major differences in loading mode (bending versus axial strain).

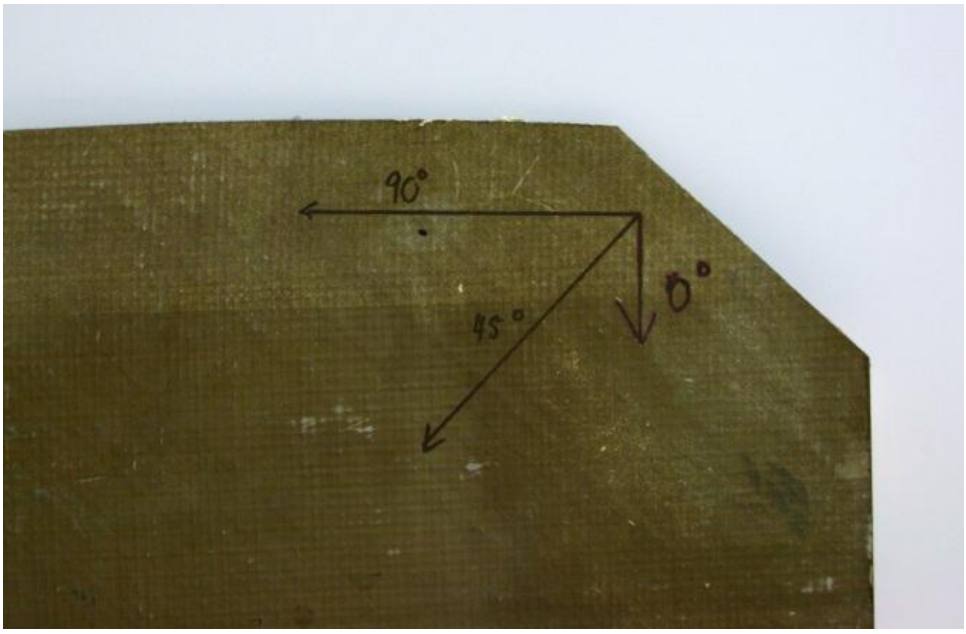

Figure 39. Tensile specimen orientation

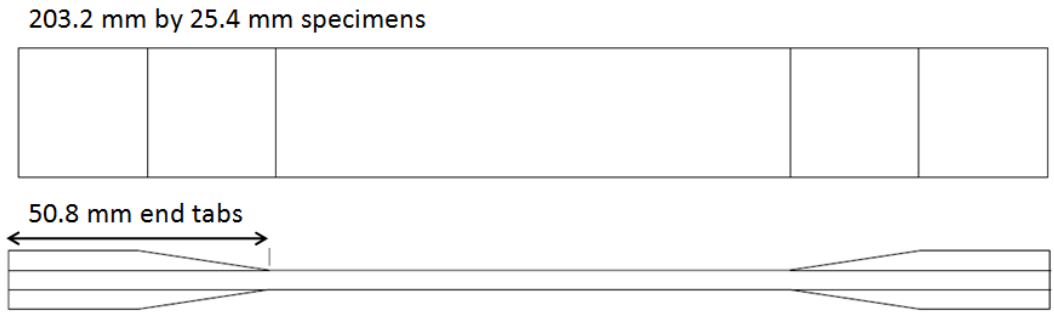

Figure 40. Tensile tests specimen

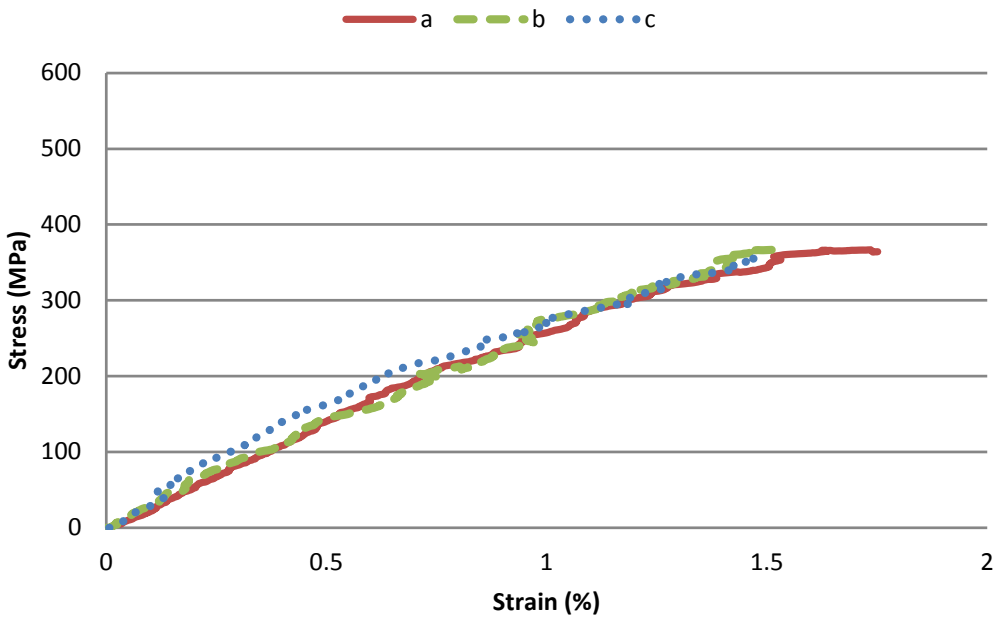

Figure 41. Stress versus strain: 0 degree orientation tensile specimens

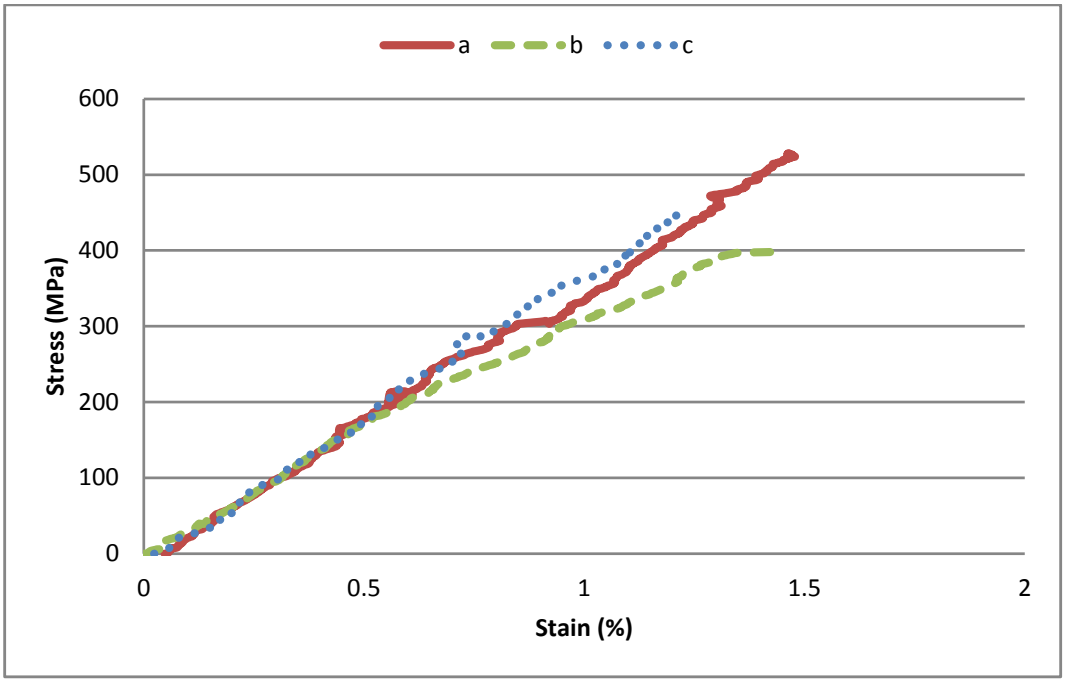

Figure 42. Stress versus strain: 45 degree orientation tensile specimens

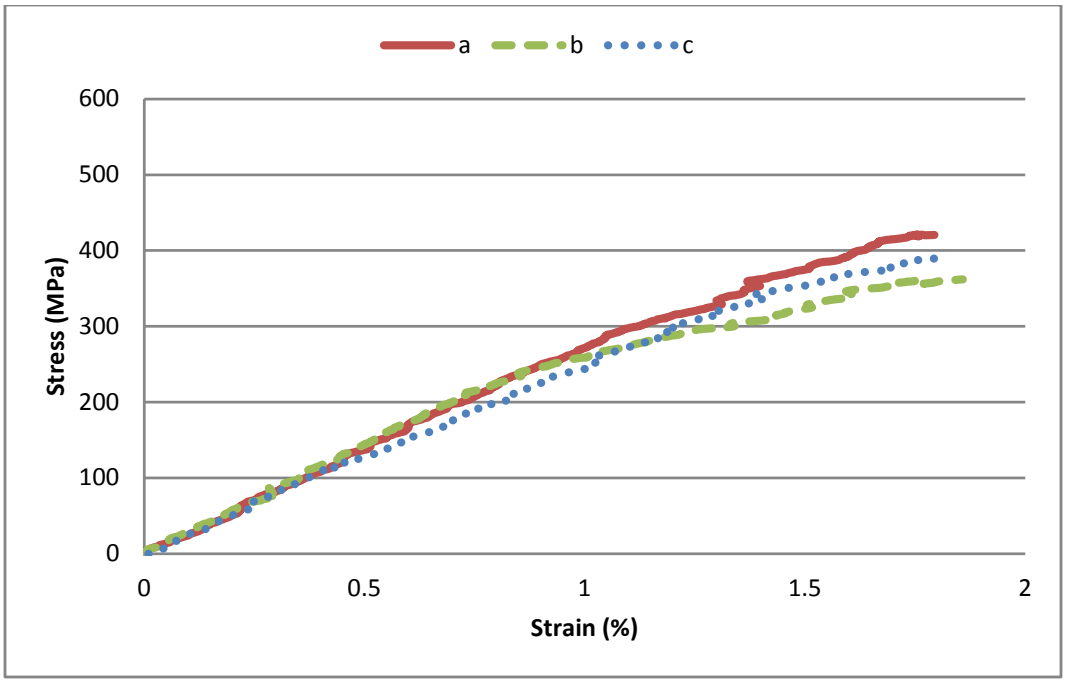

Figure 43. Stress versus strain: 90 degree orientation tensile specimens

Table 4. Tensile test Young's modulus

Young's Modulus (GPa) for Orientation:	0°	45°	90°
A	28.5	37.9	27.6
B	24.2	37.2	28.1
C	35.1	31.5	24.7
Average	29.3	35.5	26.8

Table 5. Tensile test failure strain

Tensile Failure Strain (%) for Orientation:	0°	45°	90°
A	1.78	1.50	1.81
B	1.56	1.22	1.90
C	1.49	1.64	1.84
Average	1.61	1.45	1.85

CHAPTER 5 SANDWICH BEAM TESTS

A series of experiments were conducted to observe the failure of full sandwich beam specimens using dynamic three-point bending applied via PPGP impacts. To dynamic three-point bending. Dynamic testing was conducted using the previously described PPGP to impart a known simulated explosive pressure pulse onto beam specimens. Bending of these specimens was also studied using slower, more controlled dynamic tests, as well as quasi-static tests to better observe and resolve the behavior of these specimens during the failure process.

Tests Specimens

The sandwich specimens tested consist of two 3.175 mm thick facesheets and an end-grain balsa core that is 50.8 mm thick. These were cut into 76 by 305 mm beam specimens as shown in Fig. 44.

Figure 44. Sandwich specimens

Earlier tests of large scale structural joints (related activity ongoing in parallel to, but not part of, this thesis work) using panels of the same material showed initial damage to be balsa core shear failure followed by delamination of the core from the facesheets (see Fig. 45). Small scale beam tests were therefore expected to be dominated by the same type of core failure. Physical inspection of the core showed it to be highly non-homogeneous with a significant variation in stiffness that was observed qualitatively by pressing on the surface with a sharp tool (see Fig. 46). For testing, the impacted face and camera side of the specimens were painted white to better view the development and growth of cracks. Additionally, lines were drawn longitudinally across the beam to better view core shear failure as it occurs.

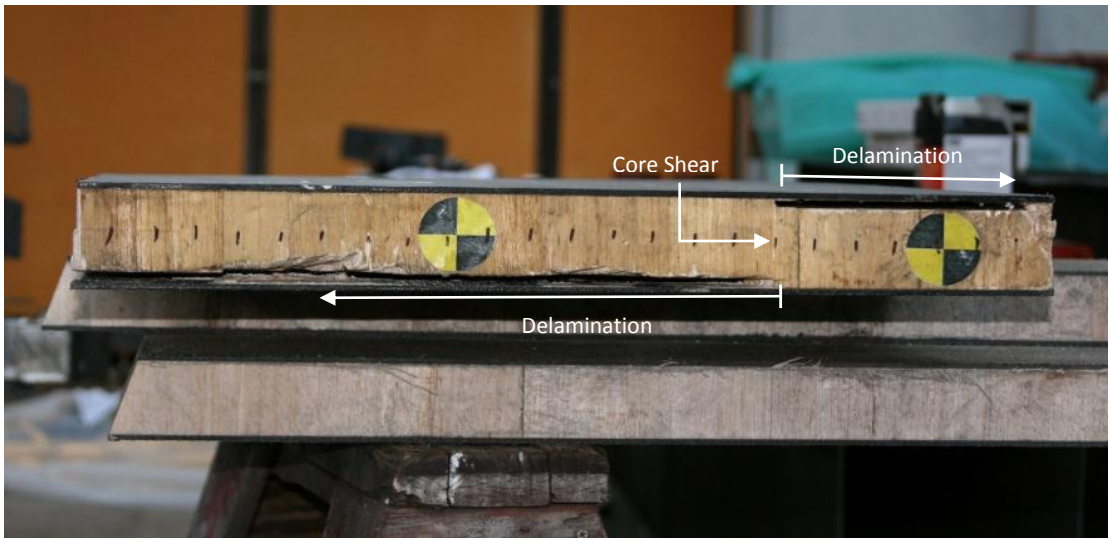

Figure 45. Shear failure of large scale testing of sandwich panels

Figure 46. Non-homogeneity of balsa wood core

High Speed Dynamic Tests

Dynamic three point bending tests were performed on sandwich beam specimens using the previously described PPGP to impart simulated explosive loading. The test specimens were instrumented with a 350 Ω strain gage (TML FLA-6-350-1L) at the midspan opposite of the impacted face to record bending strain and a 350 Ω 45° rosette (TML FRA-3-350-11-1L) was placed at the beam midplane 62.5 mm away from the edge of the beam to record shear strain developed in the balsa core (see Fig. 47). The beams were mounted using steel "v-block" supports (see Fig. 48) to hold the beams in place and provide simply supported boundary conditions. To relieve stress concentrations at points of contact between the v-block supports and the test specimen, aluminum tabs 25.4 by 76.2 mm and 3.175 mm thick were attached to the specimens to pad these locations. Four Vishay 2310B strain signal conditioners were used for strain gage excitation and signal amplification. A PicoScope 3424 12-bit digital oscilloscope was used to provide 4 channels of high speed data acquisition. Due to the limited number of channels, two strain gage outputs were connected to the same channels as the velocity measurement system (see Appendix III). Beams were supported with a span of 267 mm, with the PPGP being fired directly at the midpoint of the beam. The experiments were visually observed with a Phantom v7.3 high speed video cameras at frame rates up to 14,000 frames per second.

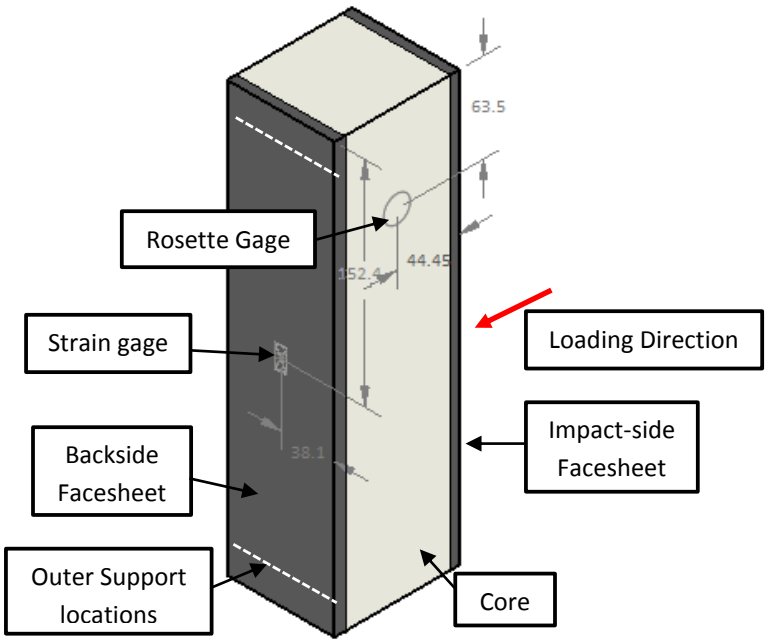

Figure 47. Dynamic gas gun test strain gage placement

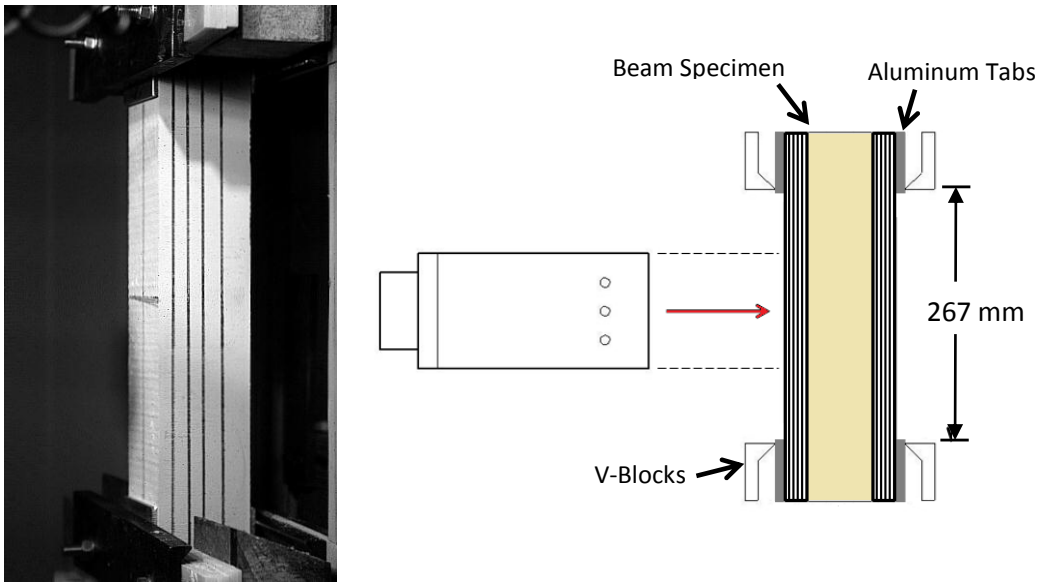

Figure 48. Dynamic gas gun test setup

Quasi-static Speed and Intermediate Speed Tests

Slower speed tests were conducted using the servohydraulic 100 kN capacity MTS 810 material test system to supplement the data from the beam impact tests. The beams were supported with a 267 mm span using the same test fixtures as the earlier thick beam tests supplying a simply supported boundary condition. Here, two 45° rosettes were placed on the core at opposite sides 63.5 mm away from the ends of the specimen along the beam midplane (see Fig. 49). Two rosettes were used to better capture shear strain at different points of the balsa core and to account for the non-homogeneous nature of the balsa wood. Loading conditions of the dynamic PPGP impact tests were simulated using a 76.2 mm diameter cylinder of hard rubber to impart a distributed pressure load at the center of the specimen as the test machine actuator pushed the beam's simple supports upwards (see Fig. 50). Slow speed quasi-static tests were conducted at 8.33×10^{-5} m/s and intermediate speed dynamic tests were performed at 0.25 m/s. For intermediate speed tests, the test machine's load cell was not able to capture data fast enough. To alleviate this, a 100 kN piezoelectric dynamic force sensor (Dytran 1060V5) was used to capture force data instead. For strain signal amplification and excitation, three Encore Model 663 strain signal conditioners and four Vishay 2310B strain signal conditioners were used to capture 7 channels of strain data.

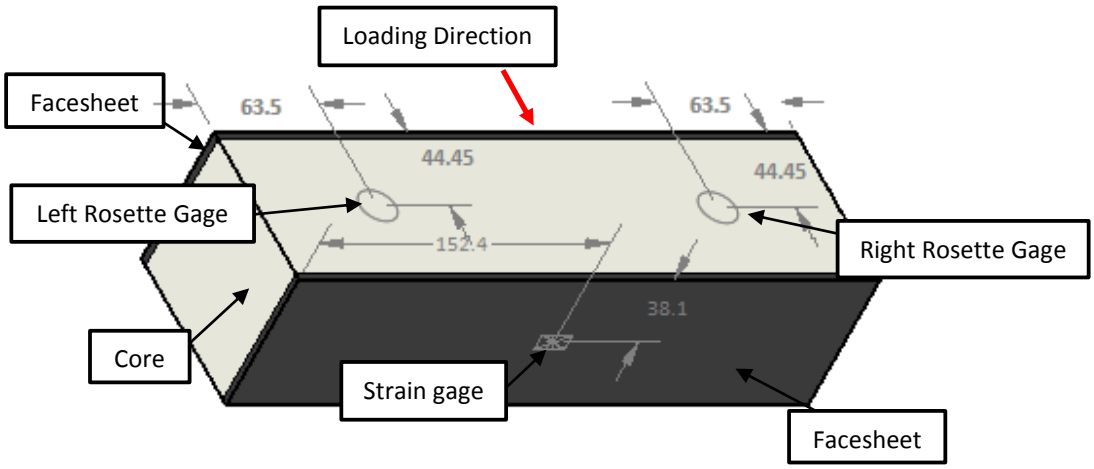

Figure 49. Sandwich beam quasi-static and intermediate speed tests

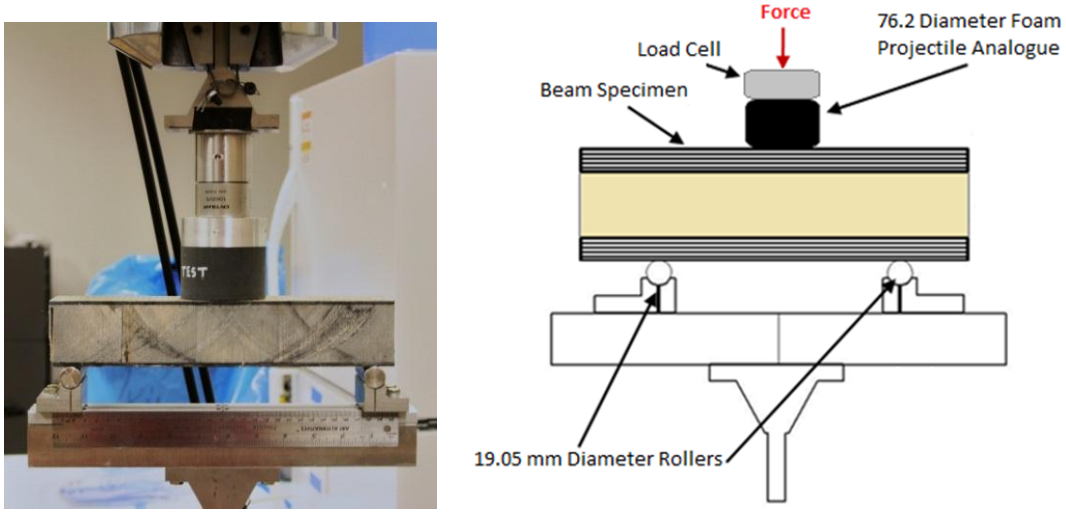

Figure 50. Intermediate and quasi-static test setup for sandwich beams

Results

Initial tests began with exploring the extent of damage the PPGP was capable of producing to the sandwich beams and what form of failure would be produced. The 160 kg/m^3 density projectile reliably produced failures in the sandwich specimens. Beam failure was dominated by shear failure of the balsa wood core followed by widespread core-facesheet separation (see Fig. 51). Locations of initial failure were fairly unpredictable, as failure tended to occur somewhere between the midspan and the location of the outer supports on either side of the beam. Single or multiple shear cracks would occur. Visible failure observed from high speed video began as a shear crack through the cross section of the balsa core.

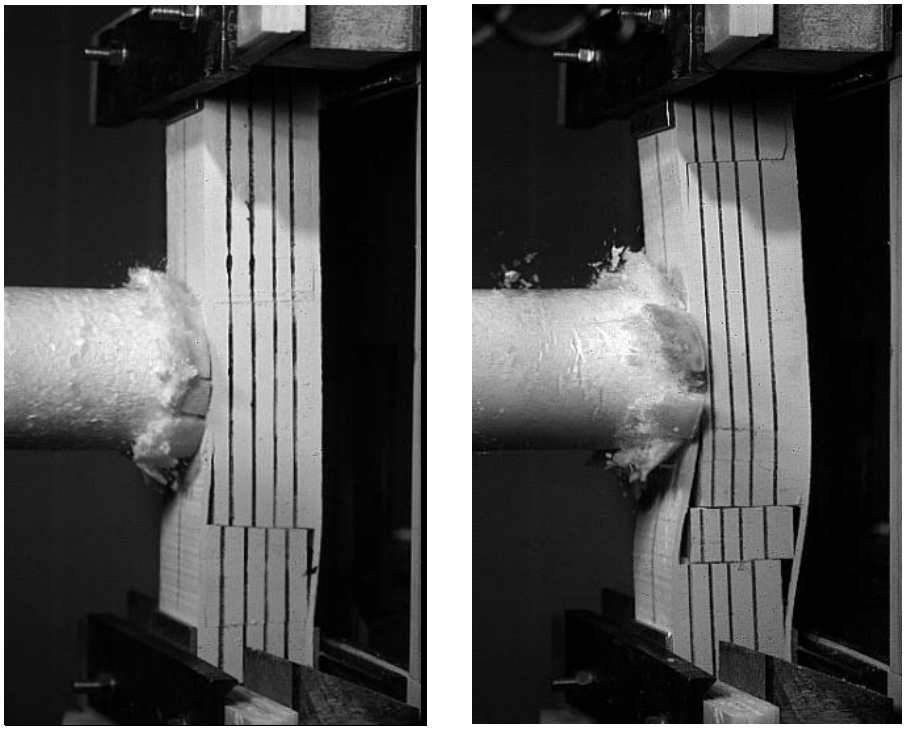

Figure 51. Preliminary PPGP tests; 160 kg/m^3 PPGP at 38.1 m/s

The initial cracks were followed by debonding of the impact-side facesheet from the core, starting from the initial shear crack and propagating towards the midspan. Separation of the backside facesheet propagated away from the midspan (see Fig. 51). No visible damage appears on the facesheets during this process. This process is detailed visually in Figs. 52-54 for all the speeds of loading.

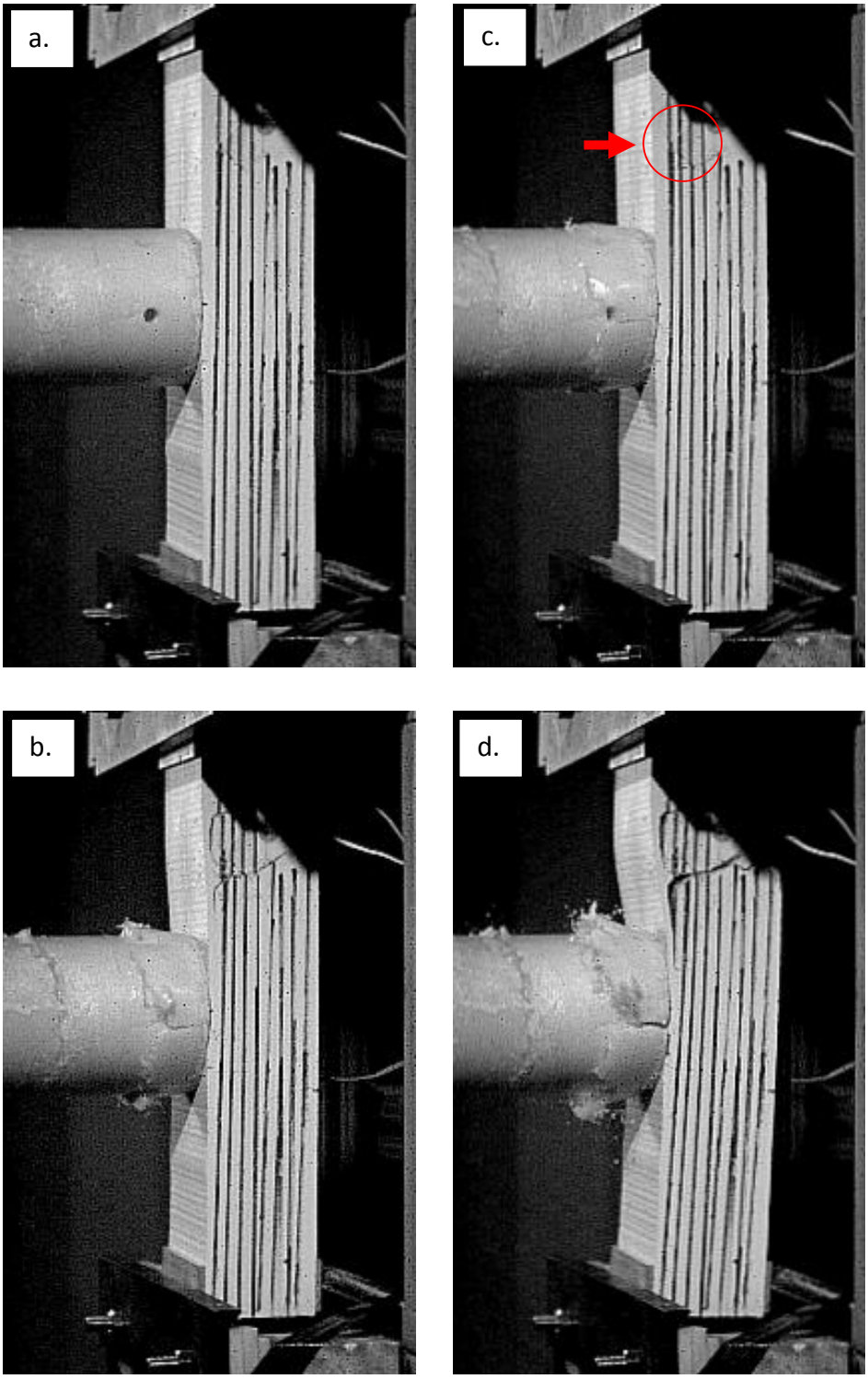

Figure 52. Shear failure in dynamic sandwich impact test; 160 kg/m^3 PPGP at 38.1 m/s; (a) t = 0 ms first contact, (b) t = 0.281 ms shear crack becomes visible, (c) t = 0.406 ms shear crack becomes larger and visibly encompasses the beam cross section, (d) t = 0.719 failure continues as the core is separated from the facesheets

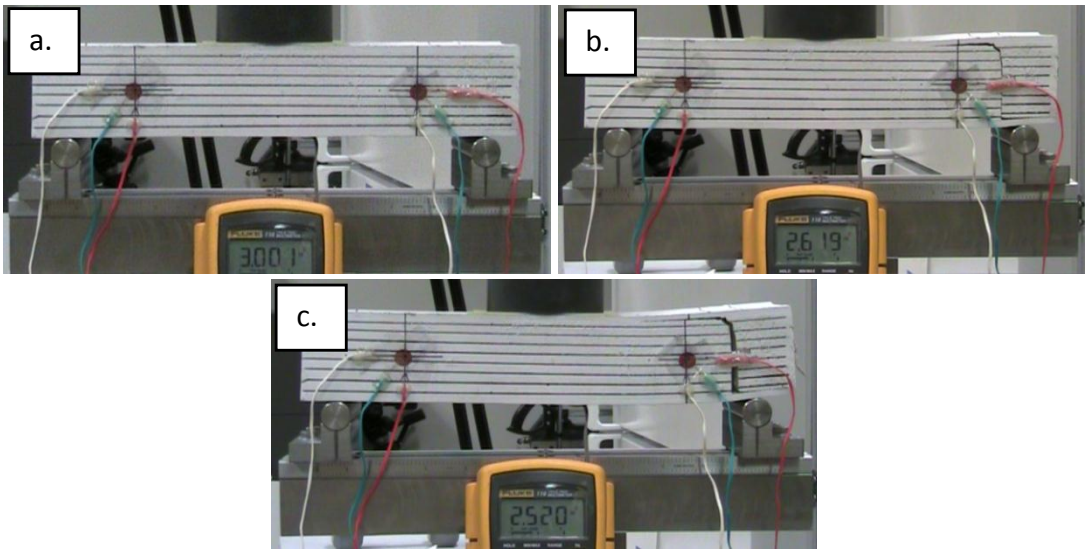

Figure 53. Shear failure in quasi-static sandwich beam test; hard rubber indentor at 8.33 x 10^{-5} m/s loading rate; (a) t = 0 sec actuator comes into contact with the beam specimen, (b) t = 45 sec shear crack becomes visible and propagates through the beam cross section, (c) t = 56 sec failure continues as the core is separated from the facesheets

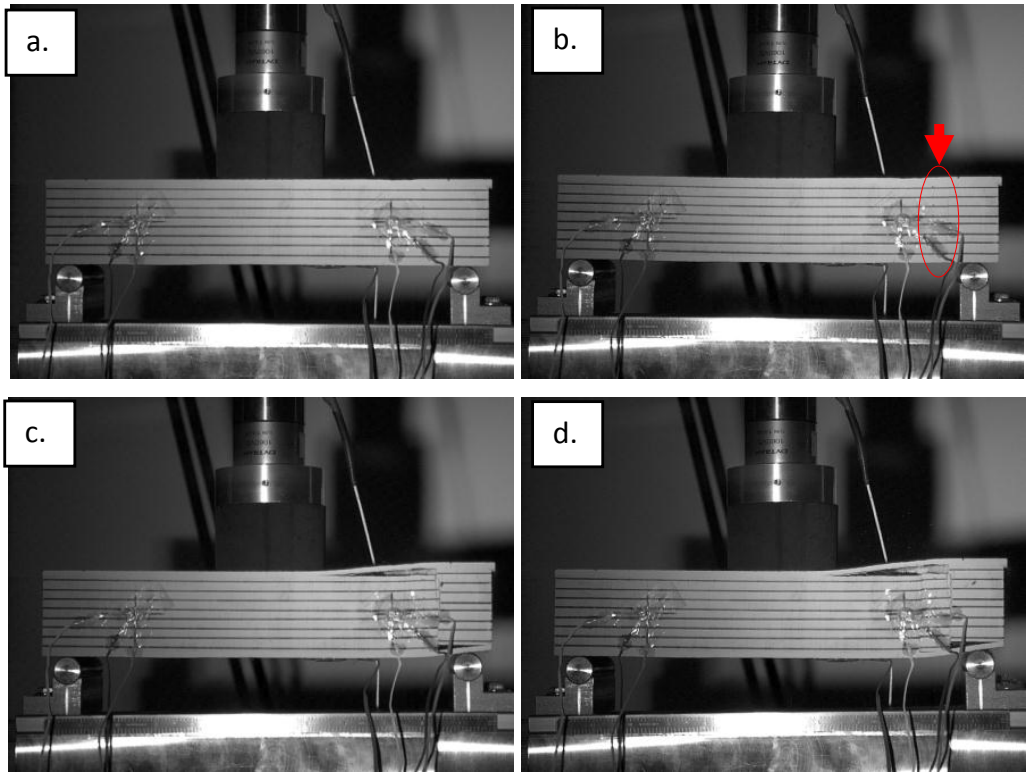

Figure 54. Shear failure in intermediate speed sandwich beam test; hard rubber indentor at 0.25 m/s loading rate; (a) t = 0 ms actuator comes into contact with beam specimen, (b) t = 15 ms shear crack becomes visible, (c) t = 16 ms, shear crack propagates through the beam cross section, (d) t = 21 failure continues as the core is separated from the facesheets

Figs. 55-57 document strain data representative of each of the three test speeds. Both strain versus time and strain versus beam center displacement are plotted for the quasi-static and intermediate speed tests. Shown here are the shear strain measurements determined via the strain rosette data, as well as the bending strain measurements given by the strain gage placed at the midspan of the non-impacted (i.e., back) face. The curves are fairly linear up to failure following initial startup loading, with catastrophic failure once the shear failure of the core occurs. Note that shear failure initiates in the much weaker balsa at levels well below any incipient failure of the composite facesheets (bending strain less than 0.3%). Observing at the strain versus time plots, it can be seen that significant stiffness loss (i.e., damage) occurs prior to the appearance of visible failure from the video documentation. For the given quasi-static test (see Figs. 53 and 56), failure occurred at 40.2 sec after actuator contact, while visible failure does not appear in the video until 45 sec after actuator contact. For the intermediate speed test (see Figs. 54 and 56), a visible shear crack can be seen forming 16 ms after actuator contact which matches with the shear strain plot where failure can be seen to also occur at 16 ms. For the dynamic impact test (see Figs. 52 and 55), failure occurs at some time between 0.128 to 0.29 ms corresponding to inflections and large decrease in the shear strain. From the high speed video, failure of the core was observed at 0.281 ms. These observations are typical for other tests that are not plotted. The peak shear strains constitute dynamic shear failure strain measurement of the balsa core material

The test results illustrate the high level of variance in the strength of the balsa, even on a single specimen. Shear failure strains can vary drastically, even across a single

specimen since shear stiffness also varies greatly based on core density. The manufacturer gave a nominal value of the balsa shear modulus as 215 MPa. This was around the middle of the range of shear moduli measured in the study by Da Silva *et. al.* [23]. Using this value as well as an assumed effective laminate shear modulus for the carbon facesheets of 15.2 GPa, an expected shear strain was calculated from the measured applied load using beam shear analyses (see detail in appendix V). The calculated shear strain, plotted together with test data in Figs. 55-57, tended to be fairly close to at least one of the shear measurements and provided a reasonable estimate of the balsa shear strength. For the dynamic impact test, shear strain was calculated using the 160 kg/m^3 pressure pulse time history measurements in lieu of the directly-measured applied load. The predicted .0085 failures strain is a close match up to the measured 0.0065 shear strain (see Fig. 55). This demonstrates that the interaction between the PPGP and beam targets resulted in pressure pulses very similar to the FMB-measured (more stiff condition) pressure pulse. Departure between the calculated and measured strain at 0.0065 indicates onset of damage resulting in stiffness loss. In Fig. 55, vibrational effects can be seen immediately after impact of the projectile, and failure of the beam occurs before the projectile reaches peak pressure.

The resulting shear failure strains for all experiments conducted are tabulated in Table 6. No strong rate dependent behavior was observed for the core shear failure, as shown by the plot of shear strain to failure versus strain rate in Fig. 58. Note the wide scatter in shear strain to failure for each test speed, which is indicative of the degree of variability of the balsa core material. Also listed are the corresponding bending strains at

the moment of core shear failure which are much lower than the failure strain associated with bending failure of the carbon fiber laminates, measured by prior tests to be in the range of 80-90%. In other words, the sandwich beams are drastically limited by the weak balsa core since carbon laminates are far from being challenged to failure.

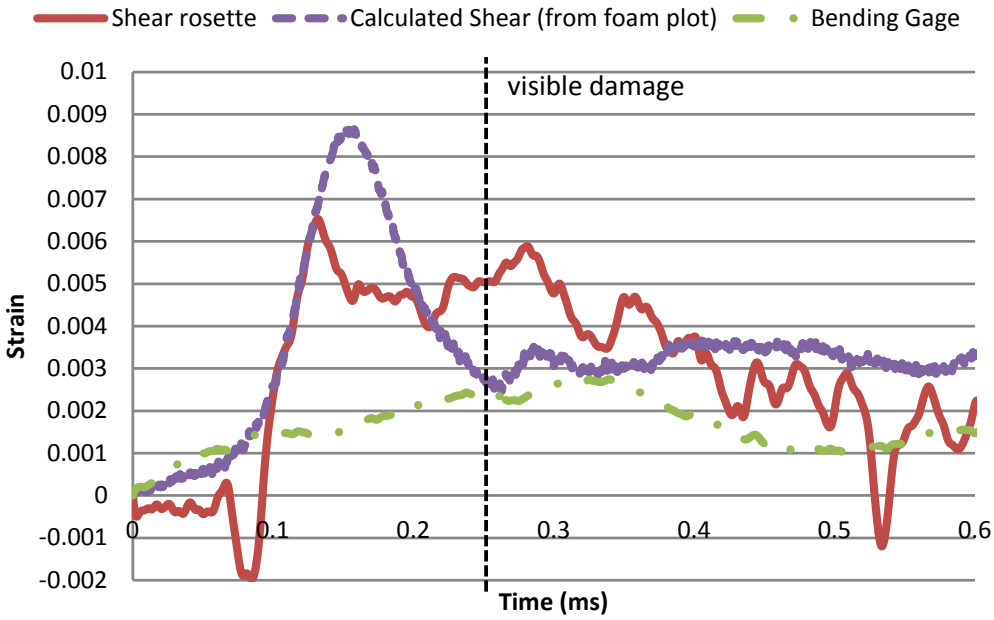

Figure 55. PPGP dynamic sandwich beam impact test strain versus time

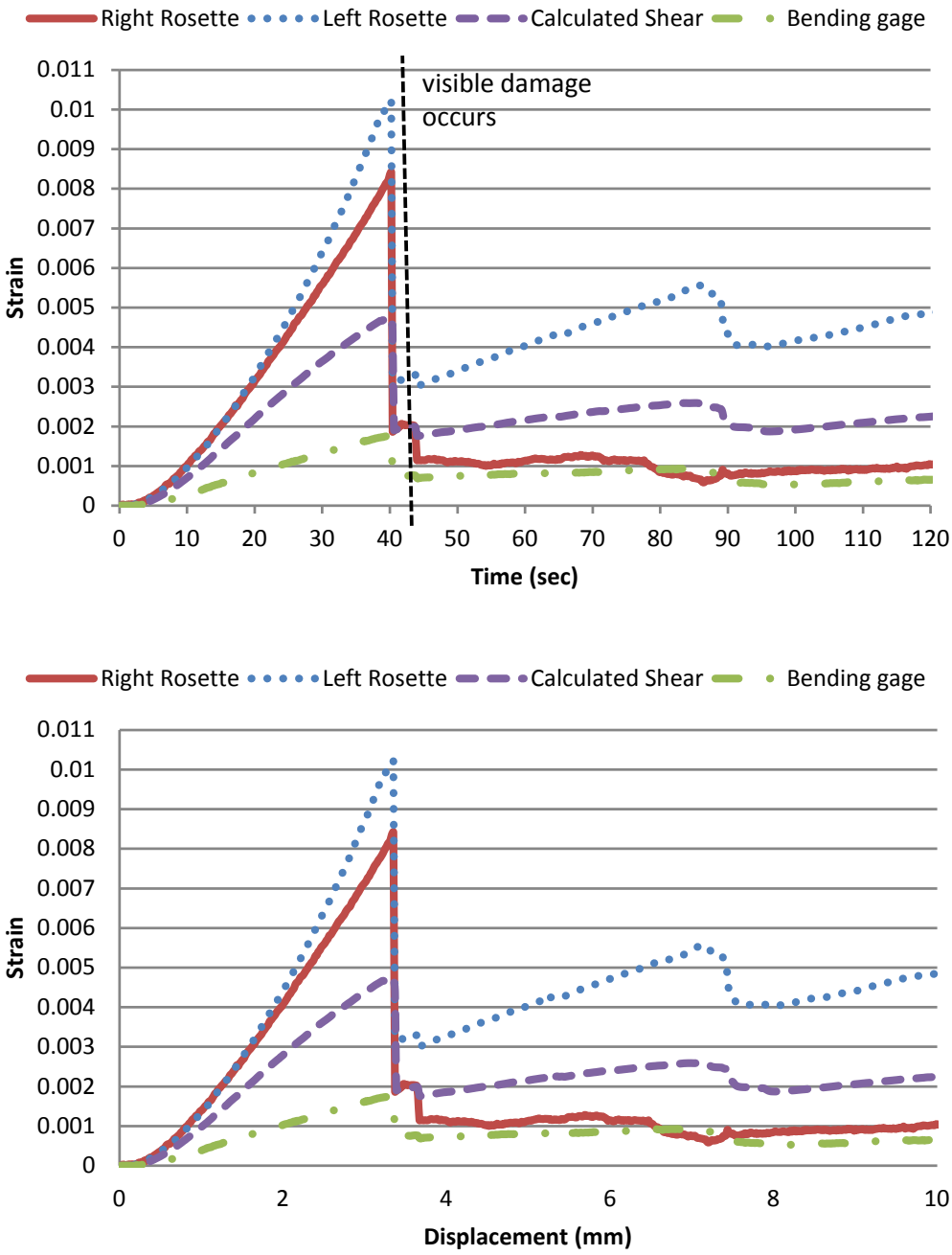

Figure 56. Quasi-static sandwich beam test (a) strain versus time, (b) strain versus displacement

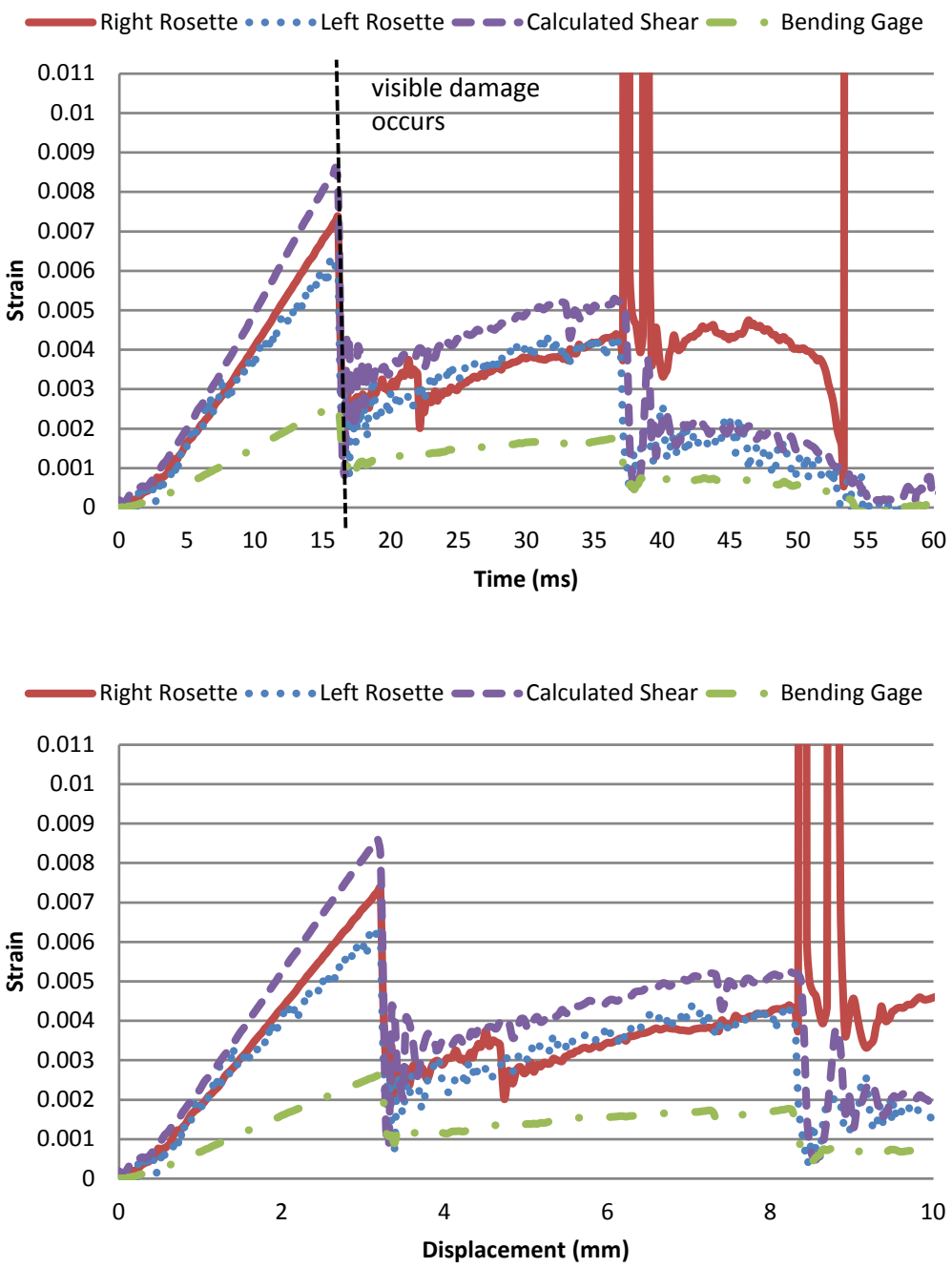

Figure 57. Intermediate Speed sandwich beam test (a) strain versus time, (b) strain versus displacement

Table 6. Sandwich beam tests

Specimen ID*	Load Rate	Bending Strain Rate	Shear Strain Rate		Ultimate Force	Peak Bending Strain	Shear Failure Strain	
	kN/s	s^{-1}		1/s	kN			
QS1	0.445	6.08E-05		1.75E-04	15.5	0.00185		0.00616
QS2	0.508	4.15E-05		1.57E-04	15.2	0.00125		0.00427
QS3	0.543	6.96E-05	LHS =	1.94E-04	22.7	0.00292	LHS =	0.00697
		6.96E-05	RHS =	1.35E-04			RHS =	0.00582
QS4	0.377	5.21E-05	LHS =	3.94E-04	12.0	0.00176	LHS =	0.0102
			RHS =	2.64E-04			RHS =	0.00842
QS5	0.355	4.93E-05	LHS =	1.34E-04	14.6	0.00201	LHS =	0.00622
			RHS =	1.38E-04			RHS =	0.00637
QS6	0.369	5.40E-05	LHS =	7.49E-04	12.0	0.00175	LHS =	0.0128
			RHS =	2.00E-04			RHS =	0.00941
IS1	NA	0.184		0.395	NA	0.00305		0.00726
IS2	NA	0.171		0.449	NA	0.00185		0.00436
IS3	1210	0.164		0.268	16.6	0.00233		0.00368
IS4	NA	0.188	LHS =	1.41	NA	0.00300	LHS =	0.0193
			RHS =	0.824			RHS =	0.0140
IS5	1540	0.183	LHS =	0.402	21.8	0.00263	LHS =	0.00627
			RHS =	0.508			RHS =	0.00738
IS6	1200	0.136	LHS =	1.54	16.0	0.00212	LHS =	0.0135
			RHS =	0.156			RHS =	0.00216
IS7	1220	0.159	LHS =	0.368	13.3	0.00194	LHS =	0.00438
			RHS =	0.818			RHS =	0.0107
IS8	1230	0.188	LHS =	0.582	17.0	0.00274	LHS =	0.00840
			RHS =	0.527			RHS =	0.00838
GG1	NA	14.1		10.7	NA	0.00276		0.00739
GG2	NA	17.3		16.6	NA	0.00195		0.00704

* GG = dynamic gas gun; IS = intermediate speed; QS = low speed quasi-static

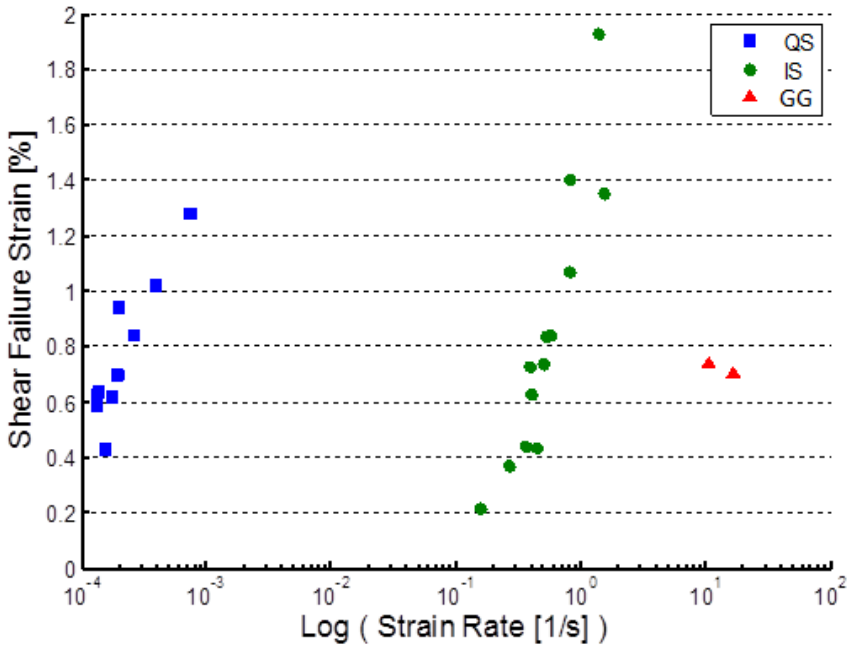

Figure 58. Shear failure strain versus strain rate

CHAPTER 6 CONCLUSIONS

This research project successfully created and implemented a new test method for the experimental simulation of dynamic explosive loading onto small scale test specimens by means of a flying a rigid polyurethane foam projectile. Use of a soft crushable projectile helped to create pressure pulse conditions similar to air blast loading. The projectiles were able to reliably produce repeatable pressure time histories that exhibited blast-like features such as: a fast rise to a peak pressure followed by an exponential-like decay into an overpressure "plateau" and ending in a drop-off to zero pressure.

This experimental method was implemented to explore the constitutive behavior and failure process of carbon/epoxy sandwich panels. These specimens consisted of high-strength carbon fiber laminated facesheets and end-grain balsa wood core. Beam specimens composed of facesheets separated from the core and were first studied using the dynamic PPGP impact test method developed and described herein. Quasi-static and intermediate speed dynamic loading applied by a uniaxial tension/compression test machine were also used to view failure behavior of the beams under slower, more controllable test conditions. When comparing the results of the dynamic tests to the quasi-static tests, it was observed that the specimens failed at significantly higher tensile strains (about 20-40% greater) and compressive failure strains (about 40-60% greater)

during the dynamic tests. This rate dependence thus makes the beams more resistant to bending failure when subjected to high rate loading.

Beam specimens made from the full sandwich were tested as well. Tests were conducted using the developed PPGP high speed dynamic test method as well as slower tests conducted with a uniaxial tension/compression test machine. These tests resulted in predominantly core shear failure behavior which exhibited wide scatter. Initial failure mode was always shear cracks forming in random locations between the outer supports and the impact zone of the projectile (beam center). Failure of the beam was dominated by shear failure of the core along the grain. Shear strain measurements varied drastically from one side of the beam to the other due to the large variation in the balsa stiffness and strength which are related to the materials' density. Following shear cracks initiating along the grain of the balsa core, extensive detachment of the core from the facesheets occurred, originating from the locations of the initial cracks. The large-scale debonding of the core leads to drastic stiffness reduction and loss of load bearing capability, i.e., complete failure of the sandwich beam. Shear strain to failure, measure over a strain rate of 10^{-4} to 10^{1} s^{-1} was found to be strongly dependent on strain rate. The balsa core material is a weak link in the sandwich panel construction dominating failure of transversely-loaded panels. Great improvements in the sandwich panel structural performance can be gained by use of a core material having higher transverse shear strength as well as much more physical uniformity.

REFERENCES

1. Mouritz, A. P., E. Gellert, P. Burchill, and K. Challis. 2001. "*Review of advanced composite structures for naval ships and submarines,"* Composite Structures 53 (1), pp. 21-41.

2. Jacinto, A. C., R. D. Ambrosini, and R. F. Danesi. 2001. "*Experimental and computational analysis of plates under air blast loading,"* International Journal of Impact Engineering 25 (10), pp. 927-947.

3. Scherbatiuk, K., N. Rattanawangcharoen, D. J. Pope, and J. Fowler. 2008. "*Generation of a pressure–impulse diagram for a temporary soil wall,"* International Journal of Impact Engineering 35 (6), pp. 530-539.

4. Houlsten, R., J. E. Slater, N. Pegg, and C. G. Desrochers. 1985. *"On analysis of structural response of ship panels subjected to air blast loading,"* Computers and Structures 21 (1-2), pp. 273-289.

5. Davidson, J. S., J. W. Fisher, M. I. Hammons, J. R. Porter, R. J. Dinan. 2005. *"Failure mechanisms of polymer-reinforced concrete masonry walls subjected to blast,"* Journal of Structural Engineering 131 (8), pp. 1194-1205.

6. Slater, J. E. 1994. *"Selection of a Blast-Resistant GRP Composite Pane design for naval ship structuresl,"* Marine Structures 7 (2-5), pp. 417-440.

7. Mouritz, A. P. 2001. *"Ballistic impact and explosive blast resistance of stitched composites,"* Composites: Part A, Applied Sciene and Engineering 32 (5), pp. 431-439.

8. Deshpande, V. S. and N. A. Fleck. 2000. *"High strain rate compressive behaviour of aluminum alloy foams,"* International Journal of Impact Engineering 24 (3), pp. 277-298.

9. Radford, D. D., V. S. Deshpande, and N. A. Fleck. 2005. *"The use of metal foam projectiles to simulate shock loading on a structure,"* International Journal of Impact engineering 31 (9), pp. 1152-1171.

10. Rathbun, H. J., D. D. Rathford, Z. Xue, M. Y. He, J. Yang, V. Deshpande., N. A. Fleck, J. W. Hutchinson, F. W. Zok, A. G. Evans. 2006. *"Performance of honeycomb-sandwich beams under shock loading,"* International Journal of Solids and Structures 43 (6), pp. 1746-1763.

11. Gong, L., S. Kyriakides, and W. Y. Jang. 2005. *"Compressive response of open-cell foams. Part I: Morphology and elasitc propoerties,"* International Journal of Solids and Structures 42 (5-6), pp. 1355-1379.

12. Gong, L. and S. Kyriakides. 2005. *"Compressive response of open cell foams. Part II: Initiation and evolution of crushing,"* International Journal of Solids and Structures 42 (5-6), pp. 1381-1399.

13. Jin, H., W. Y. Lu, S. Scheffel, T. D. Hinnerichs, and M. K. Neilson. 2007. *"Full-field characterization of mechanical behavior of polyurethane foams,"* International Journal of Solids and Structures 44 (21), pp. 6930-6944.

14. Marur, P. R. 1996. *"On the effects of higher vibration modes in the analyis of three point bend testing,"* International Journal of Fracture 77 (4), pp. 367-379.

15. Marur, P. R., K. R. Y. Simha and P. S. Nair. 1994. *"Dynamic analysis of three point bend specimens under impact,"* International Journal of Fracture 68 (3), pp. 261-273.

16. Tang, C. and X. Xu. 1990. *"A new method for measuring dynamic fracture toughness of rock,"* Engineering Fracture Mechanics 35 (4-5), pp. 783-791.

17. Yokoyama, T. and K. Kisida. 1989. *"A novel impact three-point bend test method for determining dynamic fracture-initiation toughness,"* Experimental Mechanics 29 (2), pp. 188-194.

18. Tagarielli, V. L., V. S. Deshpande, N. A. Fleck. 2007. *"The dynamic response of composite sandwich beams to transverse impact.* International Journal of Solids and Structures 44 (7-8), pp. 2442-2457.

19. Steeves, C. A., and N. A. Fleck. 2004. *"Collapse mechanisms of sandwich beams with composite facesanda foam core, loaded in three-point bending. Part I: analytical models and minimum weight design.* International Journal of Mechanical Sciences 46 (4), pp. 561-583.

20. Steeves, C. A., and N. A. Fleck. 2004. *"Collapse mechanisms of sandwich beams with composite faces and a foam core, loaded in three-point bending. Part II: experimental investigation and numerical modeling.* International Journal of Mechanical Sciences 46 (4), pp. 585-608.

21. Crupi, V. and Montanini, R. 2007. *"Aluminium foam sandwiches collapse modes under static and dynamic three-point bending,"* International Journal of Impact Engineering 34 (3), pp. 509-521.

22. Lim, T. S., C. S. Lee, and D. G. Lee. 2004. *"Failure modes of foam core sandwich beams under static and impact loads,"* Journal of Composite Materials 38 (18), pp. 1639-1662.

23. Da Silva, A. and Kyriakides, S. 2007. *"Compressive response and failure of balsa wood.* International Journal of Solids and Structures 44 (25-26), pp. 8685-8717.

24. Vural, M., and G. Ravichandran. 2003. *"Dynamic response and energy dissipation characteristics of balsa wood: experiment and analysis,"* International Journal of Solids and Structures 40 (9), pp. 2147-2170.

25. Tagarielli, V. L., N. A. Fleck, and V. S. Deshpande. 2004. *"Collapse of clamped and simply supported composite sandwich beams in three-point bending,"* Composites: Part A, Applied Science and Manufacturing 35 (6-8), pp. 523-534.

26. Tekalur, S. A., A. Shukla, and K. Shivakumar. 2008. *"Blast resistance of polyurea based layered composite materials,"* Composite Structures 84 (3), pp. 271-281.

APPENDICES

Appendix I Pressure Pulse Generating Projectile

The test method used in this study required the fabrication of rigid polyurethane foam projectiles. The following contains instruction on the proper fabrication of the projectiles. Fig. 59 shows the individual pieces that constitute the PPGP: the foam body, the aluminum mass, two V-seals, and the soft foam fins.

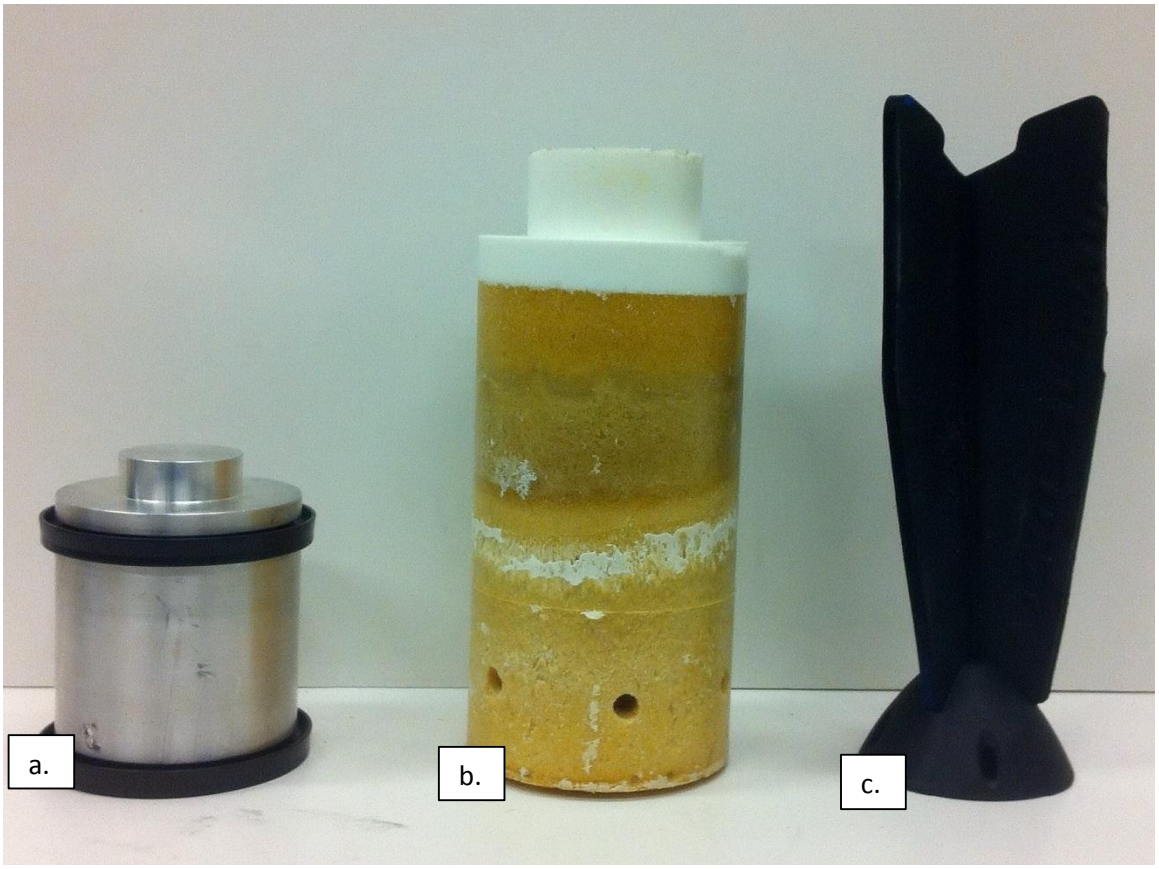

Figure 59. PPGP pieces (a) aluminum mass with two V-seals (b) foam body (c) soft foam fins

Foam Body

The foam used was the Foam-iT! series rigid urethane foam manufactured by Smooth-On, Inc. Three densities of foam were used 80 kg/m^3, 160 kg/m^3, and 240 kg/m^3, sold as Foam-iT! 5, Foam-iT! 10, and Foam-iT! 15 respectively (nominally 5, 10, and 15 lb/in^3 density). The foam projectiles were molded in a three piece stainless steel mold as shown in Fig. 59. When working with foam, eye protection and gloves must be worn at all times to avoid chemical contact with skin. The molding process begins with the application of mold release. Here, Smooth-On Universal Mold Release is used. Spray a thorough coating of the mold release along the mold interior walls, the seams between mold pieces, and any other surface of the mold where the foam may come into contact. Use a soft brush to spread the mold release to even coverage. Place the mold into the clamping fixture (see Fig. 60) to ensure a tight seal between each of the mold pieces.

Figure 60. Three piece foam mold in clamping fixture

The bolts of the fixture must be thoroughly tightened to ensure that no foam seeps out from the seams between the mold pieces. The foam comes as a two part mixture: part A and Part B. The foam will gain several times its original volume after mixing: 10 times for 80 kg/m^3, 6 times for 160 kg/m^3, and 4 times for 240 kg/m^3 (see Fig. 61).

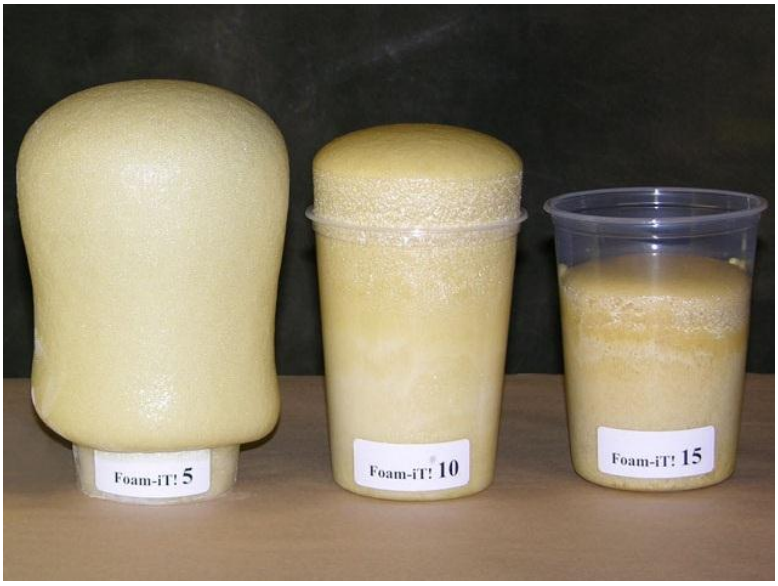

Figure 61. Volumetric expansion of urethane foams (from Smooth-On website)

Mix equal volumes of part A and part B: 2 oz. each of part A and B for the 80 kg/m^3, 3 oz. each for the 160 kg/m^3, and 4 oz. each for the 240 kg/m^3. Measure out the volumes for parts A and B (see Figs. 62 and 63). Pour them into a larger container. Mix the parts thoroughly for 45 seconds scraping the sides and bottom of the mixing container and stirring quickly. It should be noted here that the 80 and 240 kg/m^3 foam tended to be more sensitive to environmental conditions which resulted in erratic behavior during expansion. For these foam densities especially, take extra precaution during the mixing process: measure volumes of parts A and B precisely and mix as thoroughly as possible.

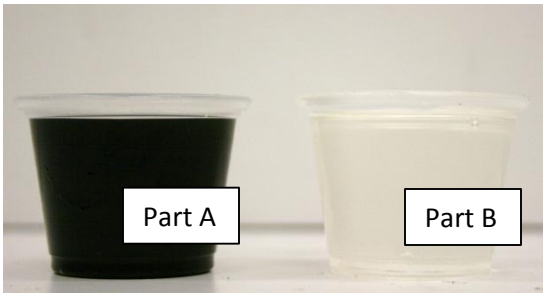

Figure 62. Rigid urethane foam parts A and B

Figure 63. Foam expansion 80 kg/m^3

Once the mixture has reached a solid color and begins to feel warm it is ready to pour into the mold. Pour the liquid into the mold opening, note the liquid is very viscous, scrape the sides of the pouring container to get as much liquid in as possible. As the foam expands in the mold, tilt and swirl the mold such that the expanding foam expands into the full volume of the mold. It is best to do this in two stages to ensure that the foam expands into the full volume of the mold: i.e. mix and pour half of the prescribed volumes of foam first, allow this first half to expand (about 1 minute), then, while the foam is still tacky, mix and pour the second half. As the second half expands,

place the bottom of the pouring container over the mold opening to apply back pressure to the expanding foam. Allow the foam to cure for two hours. Remove the mold from the clamp. Trim any excess foam from the top opening of the mold using a handsaw. Remove the bottom piece of the mold and use a soft rubber mallet to coax the foam out of the mold. It should come out without requiring too much force. The result of this process is shown in Fig. 64a.

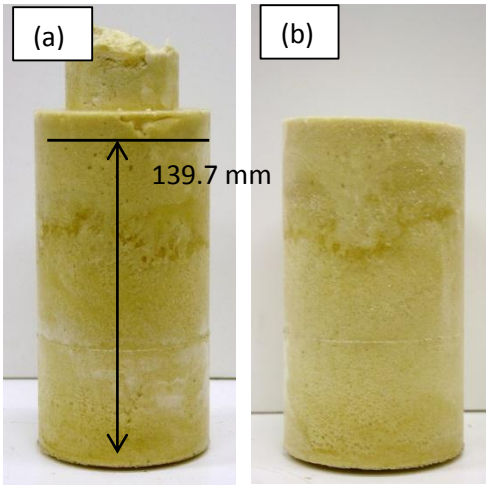

Figure 64. Foam projectile body (a) untrimmed (b) trimmed

As illustrated, the foam body is then trimmed to a length of 139.7 mm (see Fig. 64b). Mark this length off, then remove the excess portion of the foam body with a handsaw as this portion of the foam body will be replaced by a hard plastic to create a solid interface between the foam body and the aluminum mass. Replace the foam body into the mold and replace the mold into the clamp. Tighten the bolts on the clamp as tight as possible this time. The plastic used here is Smooth-On Smooth-Cast 305 white liquid plastic. This is a two part ultra-low viscosity mixture, shown in Figs. 65 and 66.

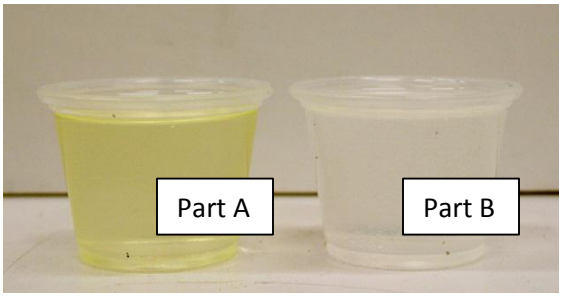

Figure 65. White liquid plastic mixture parts A and B

Figure 66. White Liquid plastic mixture

Make sure the mold is on an even surface such that the liquid plastic does not spill out when it is poured. Mix equal volumes of each part, 2 oz. each part A and part B. Mix thoroughly, stirring quickly. Once the mixture is one solid color pour into the top opening of the mold. If the plastic does not fill in the entirety of the mold, mix and add some additional plastic. Some bubbles will form as the liquid plastic seeps into the voids of the foam; use a mixing stick to tap them out. Allow the plastic to cure for 30 minutes. Once the plastic has cured, remove the mold from the clamp. The plastic may expand slightly; trim any excess that has risen above the top opening of the mold using a

handsaw making sure to create a flat surface on the top. Again, use a soft mallet to remove the foam body from the mold. There will be a thin layer of excess plastic on top of the foam. Use a sharp utility knife to shave off the excess plastic. The mold release should help the plastic to peel right off.

To control the crushing behavior of the foam, six radially holes are drilled on the front of the foam body 25.4 mm from the front face of the projectile, equally spaced around the side of the projectile. Measure and mark the centers of these holes out. The holes have diameters of 6.35 mm (1/4 in. drill bit) and are drilled to a depth of 12.7 mm. Here, a drill press is used. Clamp the foam body to the drill press table making sure not to clamp too tight and damage the body. Lock the drill press to the desired depth and drill the six holes. The result is shown in Fig. 67.

Figure 67. Completed foam body

Soft Foam Fins

The soft foam fins are used to allow the projectile to achieve stable flight. The fins used here come from a Nerf brand Vortex Ultra-light Football (see Fig. 68).

Figure 68. Nerf Vortex ultra-light football

The football is comprised of three major parts of concern: a plastic body, soft foam fins, and a hard plastic piece connecting the foam fins and the plastic body. The plastic body of the football is cut away from the rear fins using a hand saw just above the hard plastic connector. Any remaining plastic is heated with a heat gun, this softens the glue between the remaining portion of the plastic body and the hard plastic connector between the plastic body and the foam fins. The remaining portion of the plastic body can now be easily removed. What are left are the foam fins and the connector piece. These are trimmed to fit the barrel ID and then now painted black (see Fig. 69).

Figure 69. Completed soft foam fins with plastic connector

Aluminum Mass

The aluminum mass is used to impart momentum and create complete crushing of the foam (see Fig. 70). These were designed and manufactured with 6061 aluminum. The aluminum mass is designed with two grooves for rubber V-seals to sit in. These provide a low-friction, gas tight seal between the projectile and the gas-gun barrel. In the rear, the geometry is designed to seat the soft foam fins. The front has an opening to allow the foam body to fit snugly.

Figure 70. Aluminum mass with two v-seals

Connecting PPGP Pieces

The PPGP can now be constructed from its three parts shown in Fig. 71. First, use a heat gun to heat the hard plastic connector of the soft foam fins. The plastic should expand and soften once heated. It will then slip easily onto the back end of the aluminum mass. Once the plastic has cooled it should contract creating a tight fit onto the back nub of the aluminum mass. The plastic interface on the foam body should fit snugly into the front cavity of the aluminum mass. If the fit is too loose, wrap the plastic interface with a shim to create a tighter seal. If it does not fit, sand down the plastic with coarse grit sandpaper.

Figure 71. Fully constructed PPGP

Appendix II Dynamic Beam Bending

Strain Gages Placement

During dynamic beam bending tests, intense vibrations from impact loading can cause strain gage data acquisition failure. This can be caused by local failure of strain gages as well as fracture of the strain gage leads. To alleviate this problem leads must be arranged in such a way to relieve any tension that the bending beam may create as well dynamic vibration. The leads and gages must also be protected from any debris created by the PPGP during impact.

For the facesheet beam tests, two strain gages are attached, one at midspan and an outer gage 38.1 mm away from the midspan as shown in Fig. 72. Balsa wood must first be removed around the middle of the beam and where the beam is supported. The surfaces are then sanded smooth to receive the strain gage adhesive. The strain gages are oriented such that the leads are placed facing away from each other to keep the leads as that is where most of the dynamic motion occurs during testing. A length of the lead is left loose giving some slack to relieve any tension that can be developed. Just past this length, the wires are positioned away from the center of the beam and attached to the side using thermoplastic adhesive (hot glue). During testing, electrical tape is placed on top of the gages to further protect them.

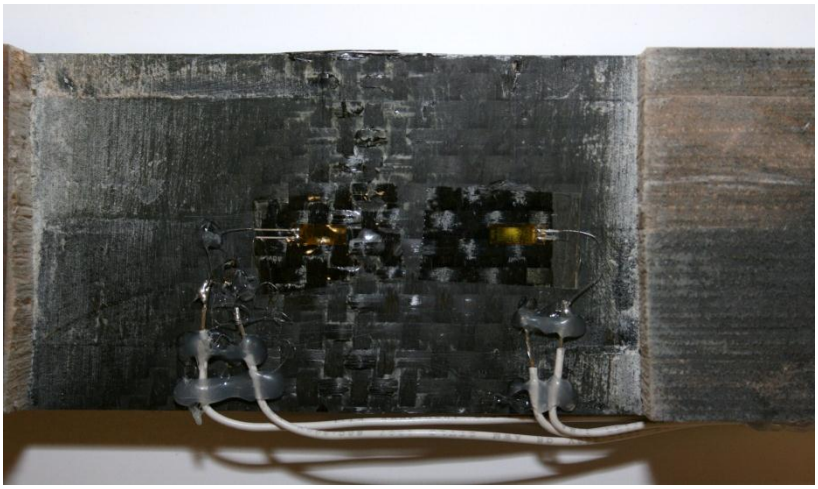

Figure 72. Facesheet beam strain gages

For the sandwich beams, a three element rosette is place on the side of the beam to record shear strain as well as a single gage at the midspan to record bending strain (see Figs. 73 and 74). This surface of the beam tends to be rough. Epoxy is first placed onto the surface to smooth out any imperfections. Once the epoxy cures, it is sanded down and a strain gage can be attached. Again, a length of the leads is kept loose to relieve any tension on the wires caused by dynamic motion. Following this length, the wires are positioned off to the side of the beam to reduce vibration on it. The leads for the rosette are placed facing away from the impact face of the beam (see Fig. 74). Table 7 lists the strain gages used in these experiments.

Figure 73. Bending gage

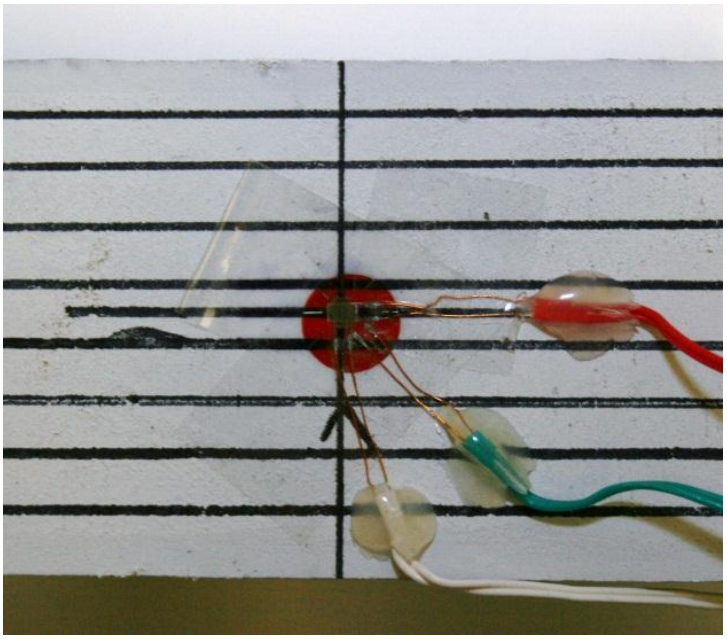

Figure 74. Strain rosette; Impact side on top of photo

Table 7. Strain gages used during testing

Strain Gage	Description	Resistance (Ω)	Gage Factor
L2A-06-250LW-350 Manuf. Vishay	Single element gage, 6.35 mm (0.25 in) gauge length and 1 m lead wires	**350.0 ± 0.6%**	**2.095 ± 0.5%**
FLA-6-350-11-1L Manuf. TML	Single element gage, 6 mm gauge length and 1 m lead wires	**350.4 ± 1.5%**	**2.12 ± 1%**
FRA-3-350-11-1L Manu. TML	0°/45° /90° 3-element rosette, 3 mm gage length and 1 m lead wires	**350.4 ± 1.5%**	**2.10 ± 1%**

Strain gage data was acquired using Encore Model 663 (see Fig. 75) or Vishay 2310B (see Fig. 76) strain gage signal conditioners set to 2 volt excitation with 100x gain and 2 volt excitation with 10x gain respectively. The strain gages wires were connected to the signal conditioners via terminal blocks (see Fig. 77) with color coded wires. The color code is noted in Table 8. Two-wire strain gages were used and connected to the red and black color leads. Therefore the sense lead was unused. The circuit was completed by connecting the white and red wires via a jumper wire.

Figure 75. Encore Model 663 signal conditioner

Figure 76. Vishay 2310B signal conditioner

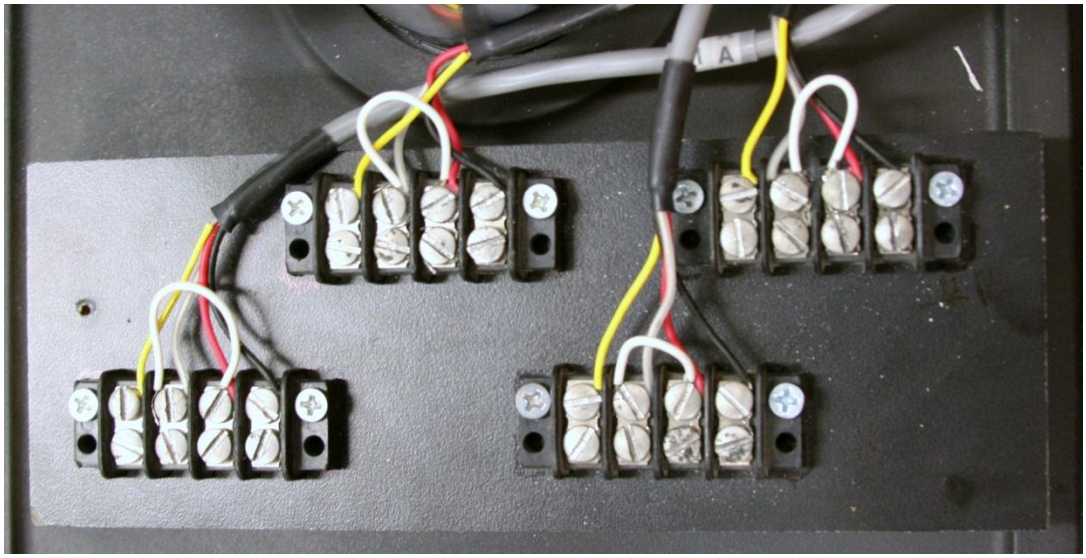

Figure 77. Terminal blocks

Table 8. Terminal block wire color code

Terminal Block Color Code		
Black	P-	Negative Excitation
Red	S+	Positive Excitation
White	R	Sense Lead
Yellow	Null	Shield/Ground

The signal conditioners were set to quarter bridge mode. The output voltage from the signal conditioners was converted to strain, ε, using the following conversion:

$$\varepsilon = \frac{4 \cdot V}{G_F \cdot E_x \cdot G_A\left(1+2\frac{V}{E \cdot G_a}\right)} \quad (1)$$

Where V is the measured output voltage in volts, G_F is the strain gage factor (see Table 7), E_x is the excitation voltage, and G_A is the gain on the amplifier.

Strain Gage Signal Conditioning Amplifier Operation

Begin by connecting the strain gages to the terminal blocks. Note that the red wire denotes positive excitation and the black wire denotes negative excitation. Ensure that there is a jumper wire between the red and white wires unless the strain gage used has a sense lead which should be connected to the white wire (without jumper).

The following lists the balancing procedures for the Encore model 663 signal conditioning amplifiers:

1. Turn on the signal conditioner box power with the switch on the right side of the front control panel.

2. Set the signal output of the amplifier to the desired gain using the knob on the top left of the control panel.

3. Set the excitation adjustment control on the bottom left of the control panel. This is labeled as EXCIT ADJ. This can be adjusted using a small flathead screwdriver. Turning the adjustment clockwise increases the excitation voltage and turning the adjustment counterclockwise decreases the voltage. The excitation voltage can be monitored using a mulitimeter from the red and black monitor ports on the bottom right of the control panel. Note that red is positive and black is negative.

4. To ensure accurate data acquisition, the Wheatstone bridge created by the strain gage circuit must be balanced to null. During this procedure monitor the output voltage of each bridge.

5. The amplifier must first be balanced. Begin by turning off the excitation voltage to the strain gage by turning the switch on the upper left corner of the control panel to ZERO.

6. Underneath the excitation switch is the bridge balance adjustment labeled BAL. Use a small flathead screwdriver and adjust the balance to null the output voltage (as close to zero as possible). Again turning the adjustment clockwise will increase the value of the output voltage and counterclockwise will decrease the output voltage.

7. Finally, turn the excitation switch to OPR to turn on the excitation voltage. Then adjust the bridge balance to null again by repeating the previous step. Note that the output voltage will be constantly changing now. The bridge output should just be adjusted to as close to zero as possible.

8. Repeat this procedure for each strain gage and signal conditioning amplifier.

The following lists the balancing procedures for the Vishay 2310B signal conditioning amplifiers:

1. Begin by powering on the amplifier by depressing the power button on the bottom right side of the front control panel.

2. Ensure the grey wide band (WB) switch is depressed to capture unfiltered data.

3. Set the gain and excitation controls to the desired settings.

4. Balance the amplifier. Begin by turning excitation toggle to off and depress the gain x100 toggle.

5. Use a small flathead to adjust the amplifier balance control labeled AMP BAL. Monitor the two output LED lights on the top of the control panel. The right LED denotes a positive output and the left LED denotes a negative output. Adjust the amplifier balance until both LEDs are off representing an output voltage of zero. Note that clockwise will increase the output voltage and counterclockwise will decrease it.

6. Depress the x1 gain toggle and set the excitation toggle to on. Note that only one output LED will be lit if there is a working wheatstone bridge circuit.

7. The Vishay 2310 signal conditioners have an automatic balancing feature. To balance the circuit, depress the AUTO BAL toggle underneath the output LEDs for about three seconds. The output LEDs should now both be off. If not, the balance can be trimmed using the TRIM control under the autobalance toggle. Clockwise is positive and counterclockwise is negative.

8. Repeat these steps for each signal conditioner.

Appendix III Gas Gun Tests

PPGPs were launched using a 79 mm (3.12 in) bore gas gun (see Fig. 78). The gas gun was powered by nitrogen gas. The pressure was monitored using a digital pressure gage. Gas gun pressure was released via a helium-activated ball valve. The projectile velocity was measured using the apparatus shown in Fig. 79. The velocity measuring system consisted of two laser photogates with a distance of 5.02 in. (~127.5 mm) between them. When a projectile crossed a photogate, it would output 4 volts. The time was measured between each crossing and a velocity could be calculated.

Figure 78. Gas gun

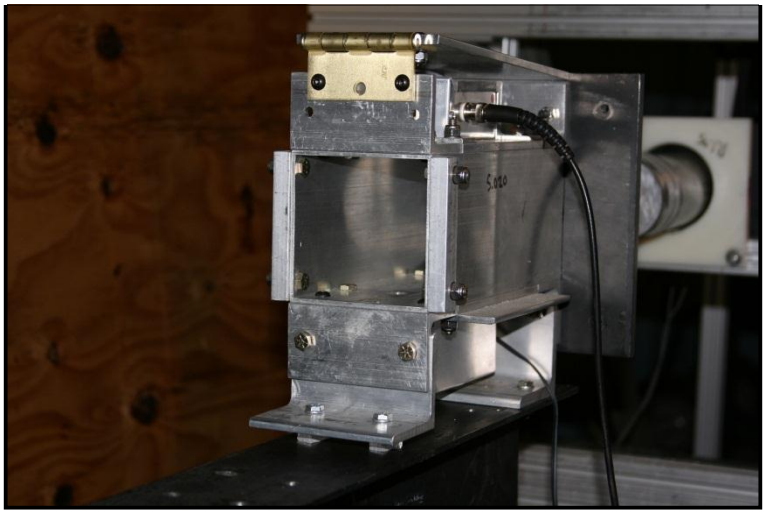

Figure 79. Velocity measurement system

Pressure versus velocity data were gathered from a number of projectiles. These were plotted and fitted to a curve shown in Fig. 80. This curve was used to provide an estimate for the velocity a given pressure could achieve for the PPGP projectile.

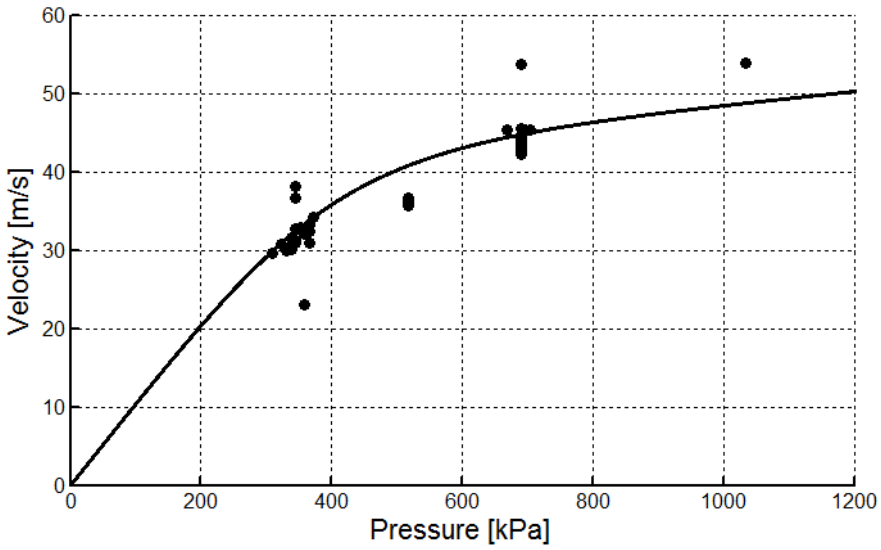

Figure 80. Velocity versus pressure curve for PPGP

A Picoscope 3424 digital oscilloscope was used to provide four channels of high speed data acquisition. Two channels were reserved for the velocity measurement system and the remaining two were used for either strain gage or FMB data. Fig. 81 shows the raw output from the Picoscope for a facesheet beam test. The data acquisition was triggered by the first photogate and the software was set to acquire 50 ms of data at 100 MHz. For FMB tests, the data acquisition input range was set to ±100 mV and for strain gages, data acquisition input range was set at ±10 V. For sandwich beam tests, two strain gage outputs were connected to the velocity measurement system output using splitter adapters. This does not interfere with the strain data collection because the output voltages from the velocity measurement system returns to zero once the projectile has passed through both photogates.

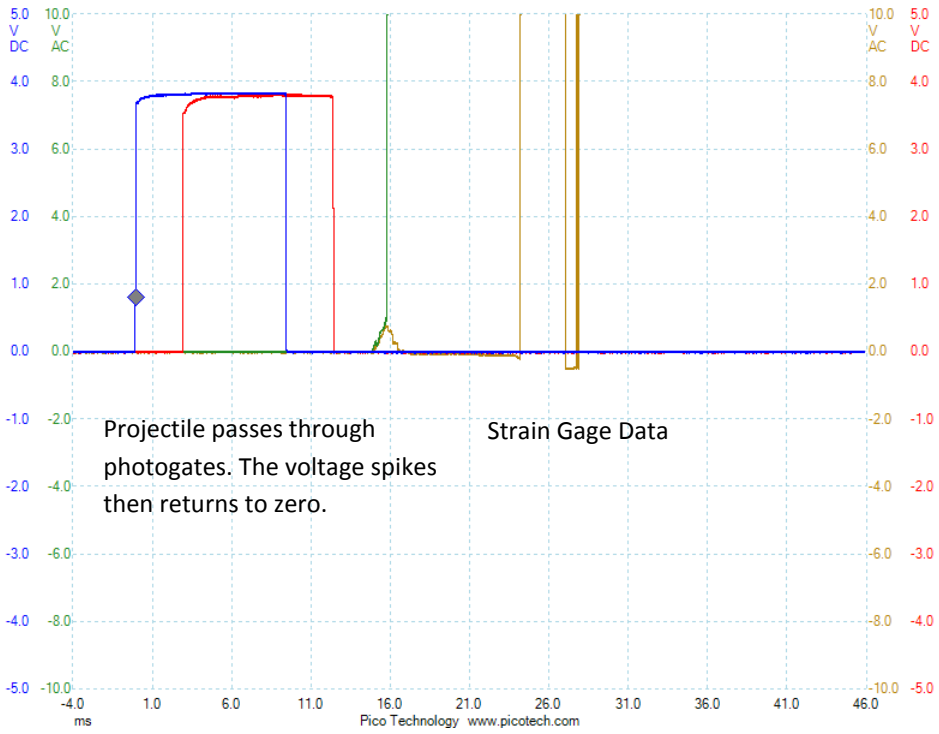

Figure 81. Typical raw Picoscope output

Force Measurement Bar

The key instrument in measuring force time histories was the force measurement bar (FMB). The FMB is a Hopkinson bar-like apparatus able to measure the force versus time response of projectiles of various shape, size, and material constituency. It consists of a 3.5 m long hollow aluminum alloy tube with an outer diameter of 76.2 mm and an inner diameter of 63.5 mm. Projectiles impact a 76.2 mm diameter, 25.4 mm thick aluminum alloy end cap (see Fig 82).

Figure 82. Hopkinson bar (FMB) and aluminum test fixture frame

The FMB measures force via two 1000 Ω strain gages (Vishay WK-13-125BZ-10C) placed on opposite sides of the aluminum tube 457 mm behind the end cap. This configuration eliminates picking up any bending strain that may occur due to eccentric loading. A projectile is launched at the end cap and, upon impact, creates a strain wave that propagates along the length of the bar. The strain gages measure this strain wave which can be converted into stress and then into force. The strain gage leads connect directly to terminal blocks mounted on the FMB. These then connect to another terminal block where a Wheatstone bridge circuit is set up (see Fig. 83). Two 1000 ohm resisters

complete the bridge and the setup is connected to a Vishay 2310B signal conditioner as a full bridge. The Wheatstone bridge circuit diagram is shown in Fig. 84 and the color code for the terminal block wires is shown in Table 9.

Figure 83. FMB terminal block

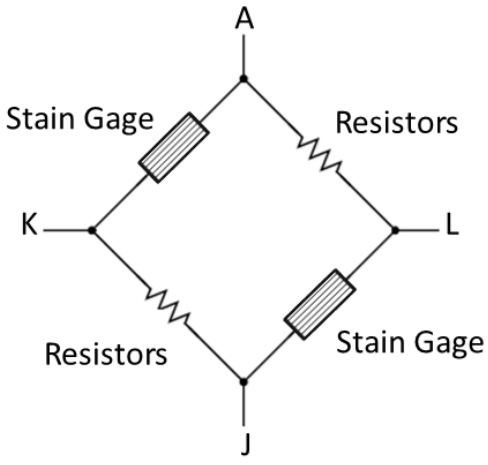

Figure 84. Wheatstone bridge circuit diagram for FMB

Table 9. FMB terminal block color code

FMB Terminal Block Color Code		
Red	A	Positive Signal Output
Black	J	Negative Signal Output
White	K	Negative Excitation
Greeen	L	Positive Excitation

The signal conditioner outputs a voltage which can be converted to strain using the following formula:

$$\varepsilon = \frac{2 \cdot V}{E_x \cdot G_f \cdot G_A} \tag{2}$$

Where V is the output voltage, E_x is excitation voltage, G_f is the gage factor, and G_A is amplifier gain. Here, a gage factor of 2.08 is used, the gages are excited with 10 V, and a 10x gain is used. The resulting strain can then be converted to force using Hooke's law:

$$\sigma = E \cdot \varepsilon \tag{3}$$

$$F = \sigma \cdot A \tag{4}$$

Here, A is the cross-sectional area of the hollow aluminum tube (1390 mm^2), and E is the Young's modulus. Here, a Young's modulus of 70 GPa for aluminum is used.

A drawback to the FMB is a limit to the duration of the force time history. This is governed by the amount of time it takes for the strain wave to travel to the far end of the beam and back to the strain gages. This can be determined by looking at the velocity v for a longitudinal wave moving through aluminum which can be obtained using the following equation:

$$v = \sqrt{\frac{E}{\rho}} \tag{5}$$

where E is the Young's modulus of aluminum and ρ is the density of aluminum, 2700 kg/m^3. We can find that the velocity of a longitudinal wave moving through aluminum is 5091 m/s. The travel time for the wave to travel to the end of the FMB and back is then about 1.2 ms. This comes to about 1.1 ms in practice. Fig. 85 illustrates this. The distance from the strain gages to the end of the FMB is about 3.05 m. The time Fig. 85 illustrates a force pulse using a hammer strike. A reflected pulse is picked up by the strain gages at about 1.1 ms after the initial strike.

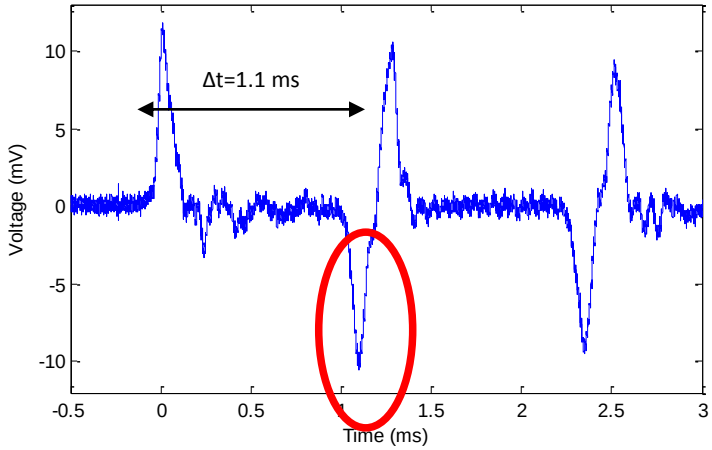

Figure 85. Hammer test illustrating FMB measurement duration

Force Cell

To record force data past the 1.1 ms duration limit of the FMB, a Dytran 1060V5 piezoelectric dynamic force sensor was used. The test apparatus used is shown in Fig. 86. The force sensor has a 25,000 lb range and the conversion from voltage to force is given as 0.214 mV/lbf (0.0481 mV/N). A 76.2 mm diameter end cap, 25.4 mm thick was mounted in front of the force sensor. The force sensor was mounted directly to a 25.4 mm thick steel plate. To help reduce dynamic vibration during impact, flat washers were placed between the sensor and the steel plate and all screws and threads were securely tightened.

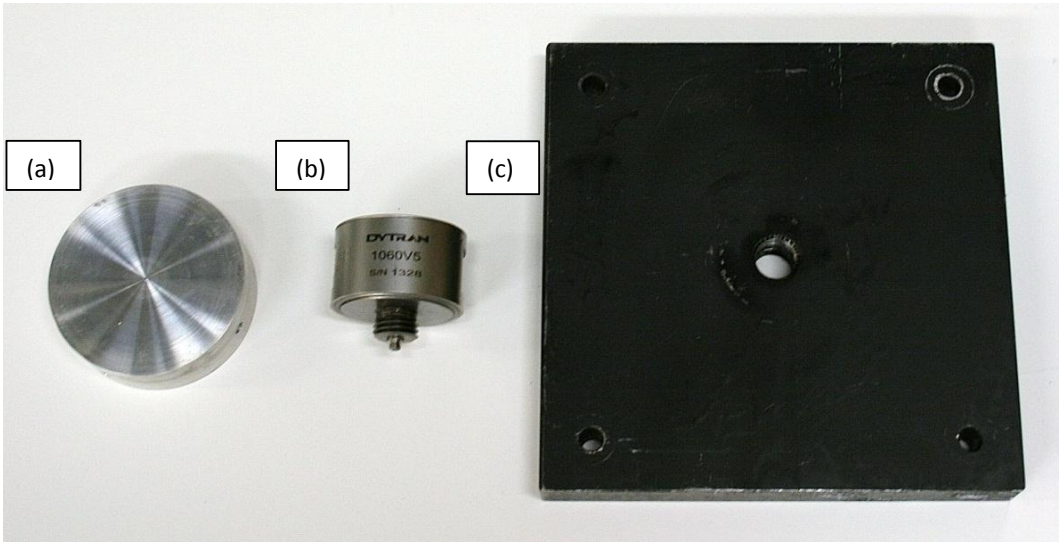

Figure 86. Force cell test fixture: (a) aluminum end cap (b) force cell (c) heavy steel fixture plate

High Speed Camera

Up to two Phantom high speed cameras, shown in Fig. 87, were used to document tests. These are used to record high speed video at frame rates up to 14,000 frames per second. Frame rate and video resolution could be controlled by the camera acquisition software (see Fig. 88). Due to a finite amount of onboard memory in the cameras, video resolution will directly affect the frame rate that could be used. Using smaller resolutions allow the camera to record at higher frame rates and vice versa. The camera can be triggered manually using a push button switch or from the camera software. The camera acquisition software controls how much video could be recorded prior to and after the trigger.

Figure 87. Phantom v7.3 high speed camera

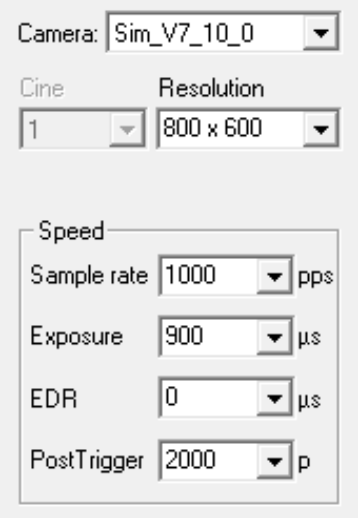

Figure 88. Camera acquisition controls for resolution, frames per second (pps) and video post trigger

The camera software provide the ability to measure speed and distances of objects in recorded video by counting pixels in the video and relating them to the desired units through a user given scale (see Fig. 89). Note that the camera is at an angle when recording the beam bending video, so the displacement measurements must be adjusted for the angle of the camera.

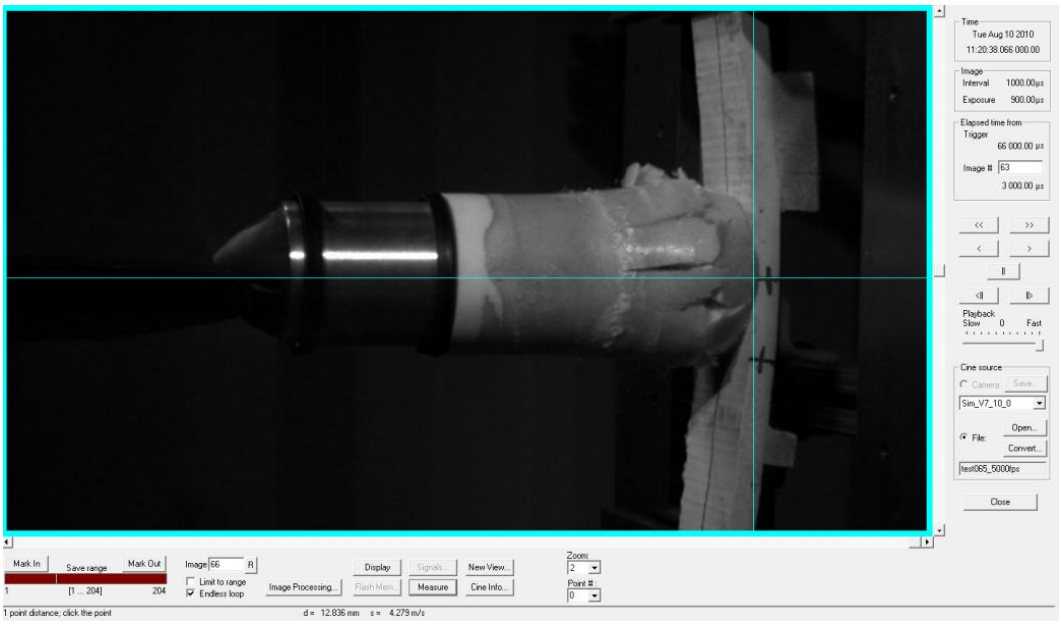

Figure 89. Camera displacement measurements

Beam Mounts

Steel V-clamps were used to provide a simply-supported boundary condition to the beams used during PPGP impact tests (see Fig. 90).

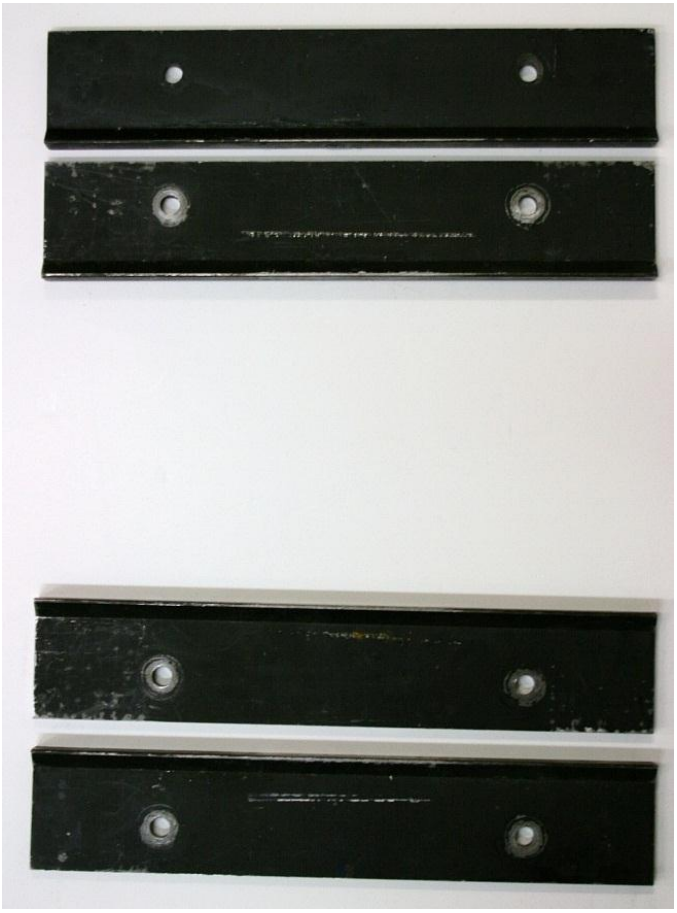

Figure 90. V-clamps provide simply supported boundary conditions

Spacers were used to create a better fit for the beams (see Fig. 91). These rested on the flat portion of the V-clamps. The clamps were then tightened to clamp down on

the beams. The spacers were made of G-10 glass-cloth laminate and scrap sandwich material. The full setup of a beam in the fixture is show in Fig. 92.

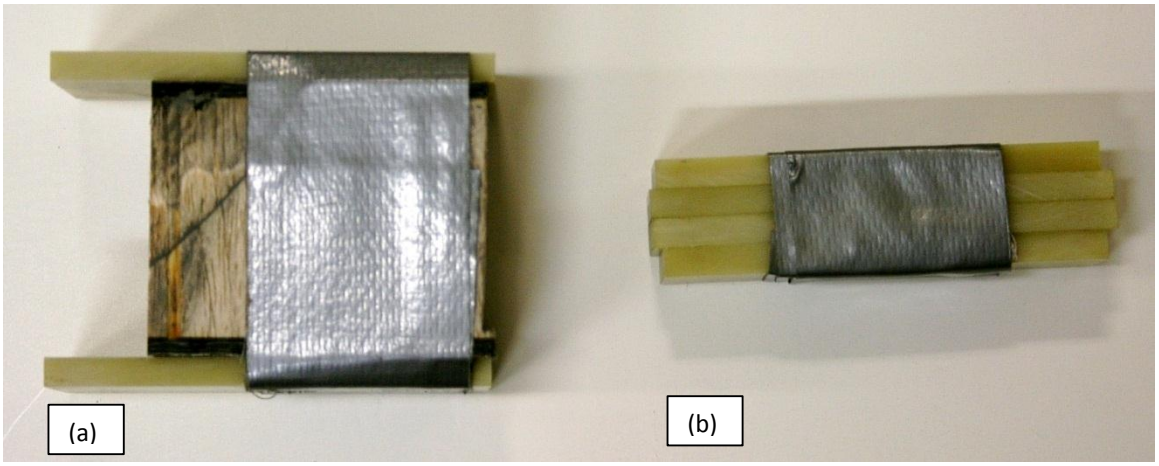

Figure 91. V-clamp spacers (a) sandwich beam (b) facesheet beam

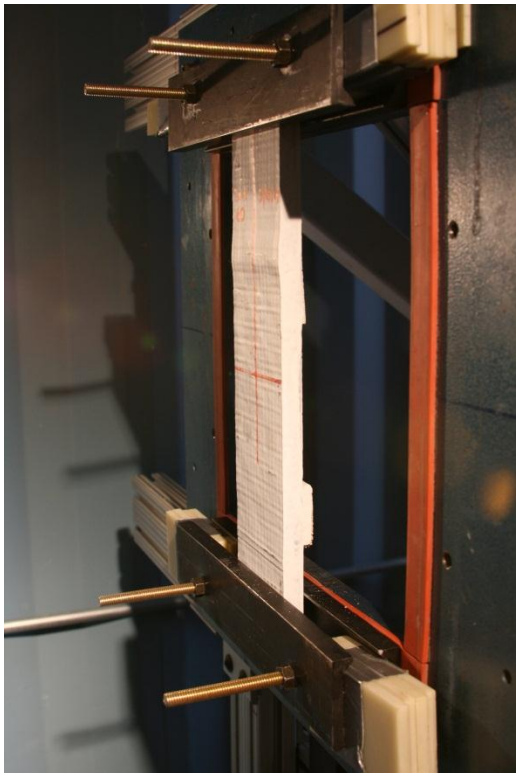

Figure 92. V-clamp fixture with beam in the aluminum test fixture frame

Gas Gun Foam Impact Projectile Test Procedure

The following is the procedure for foam projectile testing using the gas gun. Safety glasses and ear protection must be worn when operating the gas gun.

1. If a beam specimen is to be tested. Begin by mounting it in the v-clamp fixture.
2. Account for any vertical drop during flight of the projectile. Shift the specimen or FMB position if necessary, using the barrel laser to aid in target positioning
3. Connect the cable for the FMB or connect strain gages into quarter bridge terminal blocks and connect the quarter bridge cables to the Vishay 2310B signal conditioning amplifier box.
4. Balance the strain gage bridges.
5. Turn on the velocity measuring system.
6. Open the Picoscope software and ensure that trigger and data acquisition settings are as desired. The Picoscope data acquisition should be triggered by the first laser. Note that for sandwich beam tests, two strain gage outputs are connected to the same channels as the velocity measurement system using splitter adapters.
7. Check operation of triggers by interrupting the first laser to ensure the velocity measurement system is functional.
8. Monitor the Picoscope input while tapping the specimen or force sensor to ensure data is being received.

9. Setup the camera. Adjust lighting, focus, and image settings to obtain optimum picture. Test the manual trigger to ensure that it is properly activating video acquisition.
10. Perform gas gun startup procedures.
11. Weigh the projectile without the aluminum mass then with. Make note of these as well as test number.
12. Load a fully assembled projectile. The gun breech should be open. Place projectile in the front opening of the gun and use the a pole to slide the projectile back to where the breech is. Close the breech, ensure the rear end of the soft foam fins lines up with the rear end of the breech.
13. Ensure the camera and Picoscope software are waiting for a trigger.
14. Fill the main tank using the fill needle valve. Overshoot the target pressure to begin with. The pressure should drop slowly as the main tank pressure stabilizes. Allow the pressure the pressure in the main tank to stabilize, adding gas if necessary to return to target pressure.
15. Turn on power to firing switch. Depress the gun trigger and camera trigger simultaneously. Hold the gas gun trigger for about 1-2 seconds to ensure that the main tank has been fully evacuated.
16. Turn off the firing switch power
17. Open the breech.
18. Save the video and Picoscope data.
19. Repeat these tests for continued testing.

20. When tests have been concluded, begin the post-test shutdown procedure of the gas gun.

Appendix IV Servo-Hydraulic Test Machine

A MTS 810 Servo-Hydraulic Test Machine was used to conduct intermediate speed and quasi-static speed three point bend tests. Fig. 93 shows the fixtures used to conduct these tests. The fixtures consisted of two hardened steel compression platens placed into the machine grips. A 50.8 mm x 38.1 mm x 342.9 mm stainless steel beam was mounted to the bottom platen. Roller mounts were attached to this beam. 19.05 mm diameter steel rollers were connected to the roller mounts to provide simply supported boundary conditions for testing beams.

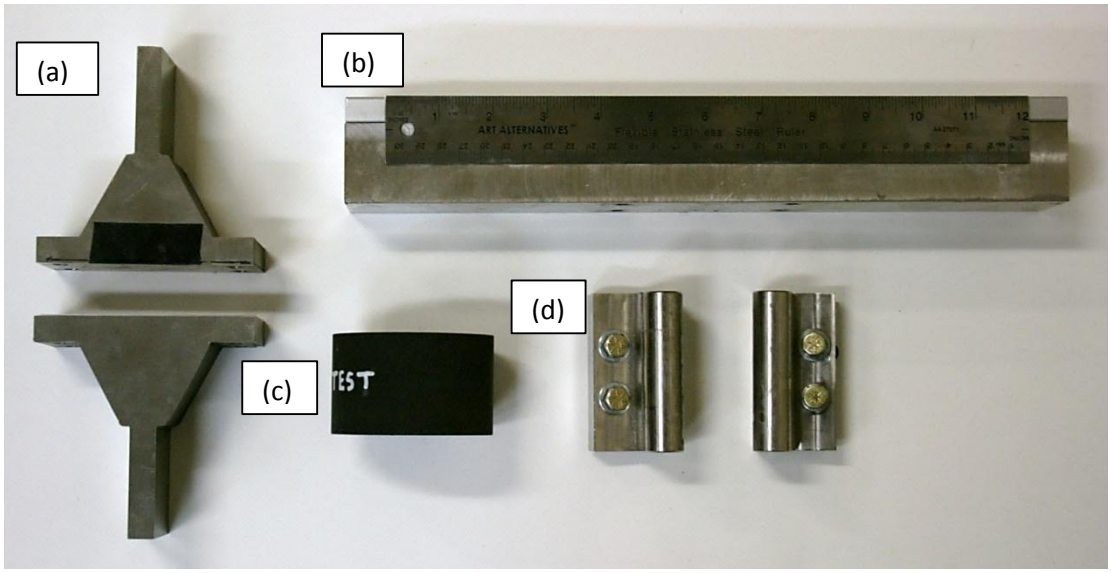

Figure 93. Three point bend test fixtures (a) hardened steel compression platens (b) stainless steel beam (c) hard rubber foam projectile analogue (d) 19.05 mm diameter rollers and mounts

Tests using the servo-hydraulic test machine were run in displacement control by specifying an actuator speed and end displacement position (see Fig. 94). To ensure the top and bottom actuators of the machine did not crash, axial displacement was not allowed to go beyond 30 mm or relative displacement (~ the height of the 19.05 mm diameter roller and mount). The test machine provided seven channels of data acquisition, the axial displacement of the actuator, and an on-board force cell (see Fig. 95).

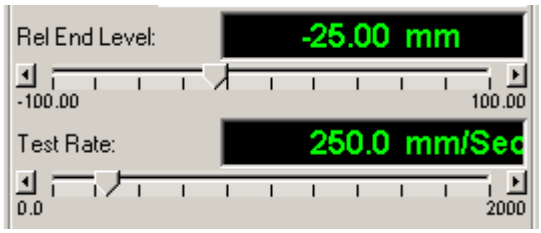

Figure 94. Displacement and speed controls

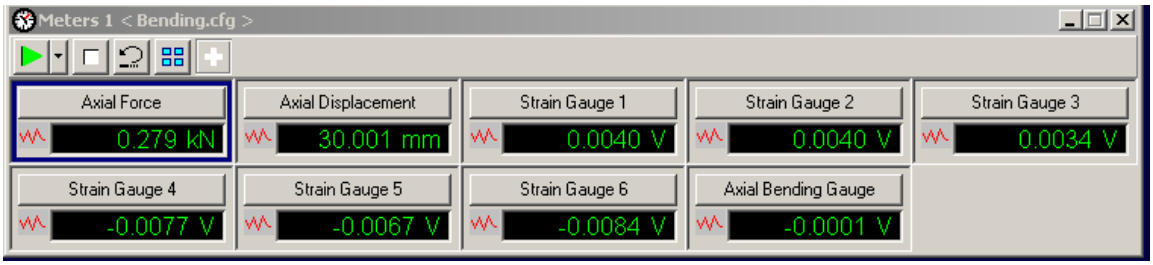

Figure 95. MTS machine channels

For intermediate speed tests, the Dytran 1060V5 piezoelectric dynamic force sensor was used in place of the test machine's force cell. The force cell data were acquired using the Picoscope 3224 digital oscilloscope and triggered using a displacement output from the test machine.

MTS 810 Servo-Hydraulic Test Machine Test Procedure

The procedure outlined here are the steps to perform three-point beam bend tests (quasi-static and intermediate speed) using the MTS 810 servo-hydraulic test machine shown in Fig. 96. Safety glasses must be worn during MTS machine testing.

Figure 96. MTS 810 material test system

The following list the startup procedures for the MTS 810 test machine:

1. Turn on the pump coolant water.
2. Turn the main pump switch on. All the lights on the pump machine will turn on. Push the blue reset button. Lightly twist the red emergency stop button to ensure that it is open.

Figure 97. Main hydraulic pump

3. Turn the Flextest SE controller on.

Figure 98 Flextest SE controller

4. Control of the test machine is performed on via computer control software shown in Fig. 99. Start the MTS desktop organizer , the start the station manager

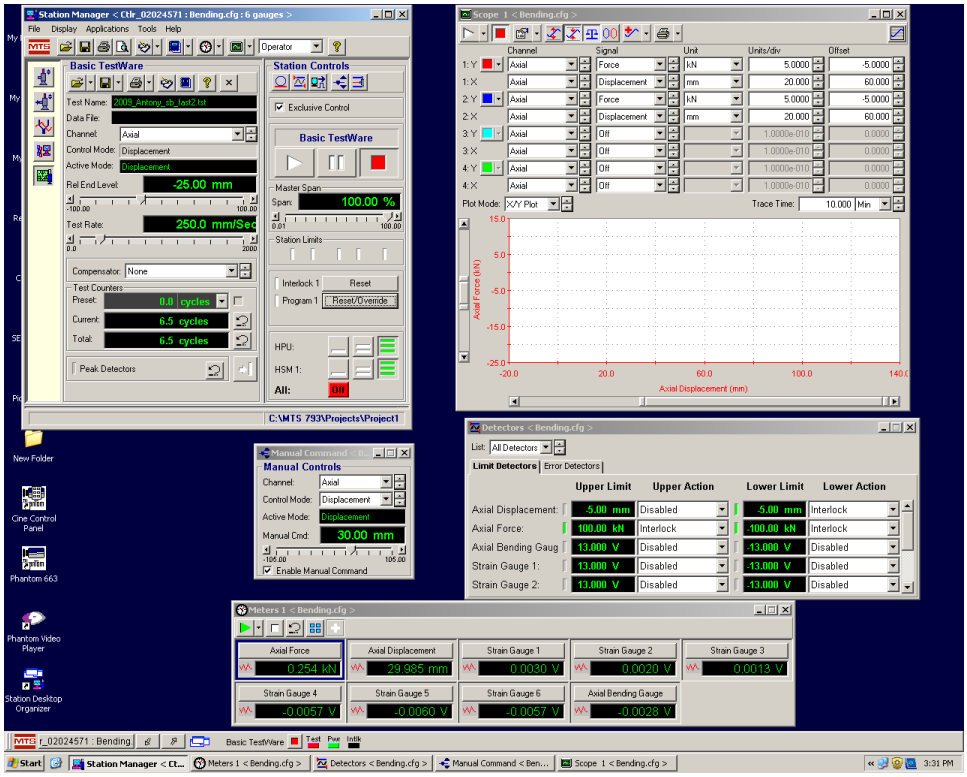

Figure 99. Station Manager software

5. Select a configuration file this will define the data acquisition inputs for the controller.
6. Turn on Exclusive control.
7. Reset the interlock if on.
8. Turn on the pump by software. Turn HPU on low first, waiting a 10 seconds then high.
9. Ensure grips are open
10. Repeat for the HSM1 control.
11. Click on function generator.
12. Choose displacement control mode, cyclic command type, sine tapered wave shape with PVC compensation.
13. Use the manual command to position test machine actuator to desired position i.e. 40 mm.
14. Choose a target set point to current position, i.e. 40mm start with amplitude of 2 mm, 0.5 Hz
15. Allow this to run for 15 min and ensure that manifold in back of actuator is warm.

The following are procedures for three-point beam tests set up:

1. Place hardened steel platen into bottom actuator grip ensuring that the platen is level when the grip is tightened ensure that the grip pressure remains set to about 7MPa (1000 psi).

2. Place the top platen on top of the bottom platen to assess where the top grip must be positioned. Note this and remove.
3. Bring down the top grip until the grips line up to where they will grip the top platen. Note: move the top grip into place with great care not to crash the test machine.
4. Bolt the top and bottom platens together. Then tighten the grips of the top actuator. This insures that the two platen faces are in planar alignment.
5. Unbolt the two compression platens and return the top actuator to the desired level.
6. Bolt steel beam to bottom platen. The four threaded holes on the bottom of the beam should line up with the holes on the platen.
7. Insert the two roller and roller mount assemblies to the aluminum track on the top of the stainless steel beam. Adjust the rollers to a desired span ensuring the beam midspan will lie at the center of the stainless steel beam.
8. Tightly bolt the roller assemblies to the aluminum track and ensure the rollers remain perpendicular to the length of the stainless steel beam.
9. Mark on the beam the locations of the rollers and midspan. Also mark a 76.2 mm (38.1 mm on either side of midspan) long area where the 76.2 diameter hard rubber cylinder will be placed. Place the beam specimen on the rollers and attach strain gages to the terminal blocks.
10. If necessary, place the external force sensor assembly on the beam. This should include the 76.2 mm diameter endcap, a threaded connector and washer to protect the force cell wire.

11. Bring the top actuator back to a desired level fairly close to the test setup while not putting any pressure on it.

The following are procedures for three-point beam test data acquisition:

1. Enter the Basic TestWare function of the station manager.
2. Ensure that proper interlocks have been set in the detectors window. Here, the relative axial displacement must not exceed the height of the roller and roller mount assembly to keep the bottom actuator from crashing into the top actuator.
3. Ensure that the data acquisition is set up correctly by checking the inputs in the meters window. For the beam bending configuration file, all seven external inputs of the controller are set up acquire raw voltages from the strain gage signal conditioner outputs.
4. Open the desired test file or manually modify the settings through the test setup options. This can be reached with the button at the top of the Basic TestWare window with the picture of a hand writing on a book.
5. In the data acquisitions tab of the test setup menu, check that all signals desired are in the signals included column and the sample rate is set to a desired level (6 kHz and 5 Hz was used for intermediate and quasi-static speed tests respectively).
6. In the data file tab, enter a title for the data file and close the test setup window.
7. Set a desired relative end level defining the actuator total stroke. This should be between 25 and 30 mm to avoid crashing the actuators and fully fail the beams.

8. Set a desired test rate (250 mm/sec for the intermediate speed tests and 5 mm/min for the quasi-static tests).
9. For intermediate speed tests, an external force sensor was used. It connects to an external power source and amplifier. The amplifier then connects to a Picoscope 3224 digital oscilloscope. The second input of the Picoscope is connected to the first external monitor port of the test controller. This is set to output actuator displacement. The Picoscope software is set to trigger acquisition once the actuator displacement goes below 20 mm (falling edge, 2 volts) with the trigger falling after 25% of data is recorded.
10. If desired, set up a camera for test documentation. For high speed recordings of the intermediate speed tests, video was taken at 800x600 pixel resolution at 1000 frames per second. These settings provide 5 seconds of recording time. The camera should be triggered manually
11. Ensure strain gage bridges are balanced and the meters for each are close to null before proceeding.
12. Manually bring the bottom actuator to a desired start position with the manual controls window.
13. Begin the tests by ensuring manual command is not enabled and interlocks have not been tripped (reset if needed). Press the play button to begin.
14. Once the test has run, return the bottom actuator to its starting position and change the data file name before proceeding to any subsequent tests.
15. Once testing has been completed, carefully remove the three-point bend fixtures from the machine grips.

16. Turn off the HSM1 and HPU controls slowly. Turn them to low first, wait five seconds, then turn them totally off.
17. Switch the pump switch to off and shutoff the pump coolant water.
18. Close the station manager software then shutoff the controller.

Appendix V Beam Shear Calculations

Classical beam theory was used to calculate shear strain on the sandwich beam tests and provide a check for accuracy of test results. The beam section dimensions are given in Fig. 100a.

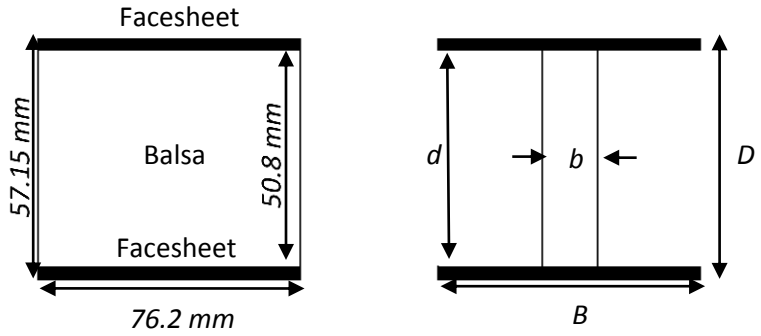

Figure 100. (a) Section dimensions (b) the transformed section

The calculations were done using a transformed section shown in Fig. 100b to account for the difference in sheer modulus between the balsa and carbon fiber facesheets. The transformed width of the core *b* is given by the following equation:

$$b = \frac{G_{balsa}}{G_{carbon}} B \tag{6}$$

Where the shear modulus of the balsa is given as 215 MPa and the shear modulus of the carbon is given as 15.2 GPa. This results in a transformed width of the core of 1.08 mm.

A moment of intertia *I* of the transformed section is given as:

$$I = \frac{BD^3 - d^3(B-b)}{12} \tag{7}$$

The beam is idealized as undergoing pure three-point bending. Maximum shear stress is then found with the following equation:

$$\tau = \left(\frac{P}{8\,b\,l}\right)[B(D^2 - d^2) + bd^2] \tag{8}$$

where *P* is the force at the center of the beam. This can then be easily transformed into shear strain γ using Hooke's law:

$$\gamma = \frac{\tau}{G} \tag{9}$$

Appendix VI Table of Tests

Table 10 lists the tests performed for work on this thesis.

Table 10. Table of tests performed

Test No.	Date	Target	Psi	Mass of Foam	total mass	Density	Velocity	Projectile Features	Notes
				g	g	lb/ft³	ft/s		
1	8/27/2008	Steel Plate	100	NA	NA	5	176	NA	1.5 in to the right of target
2	8/27/2008	Steel Plate	50	NA	NA	10	120	NA	0.5 in low center to center perfect
3	8/27/2008	Steel Plate	50	NA	NA	10	125	NA	flat face
4	8/29/2008	FMB	52	NA	NA	15	105.7	fiber reinforced, all 15	Force data lost
5	8/29/2008	FMB	48	NA	NA	10	98.3	15 fiber reinforced	
6	8/29/2008	FMB	48	NA	NA	10	98.8	All 10 epoxy reinforced	
7	8/29/2008	FMB	50	NA	NA	15	101.1	all 15 no reinforcement	
8	9/19/2008	FMB	47	134.3	852.6	10	100.9	sides reinforced	
9	9/19/2008	FMB	52	144	857.7	10	105	top reinforced	
10	9/19/2008	FMB	51	160.9	874.6	10	NA	top and sides reinforced	Force data lost
11	9/19/2008	FMB	45	215.1	933.4	10	97.3	plastic	
12	9/26/2008	FMB	53	185.4	892.2	5	106.5	plastic	Video lost
13	9/26/2008	FMB	48	234.6	941.4	10	98.8	plastic	
14	9/26/2008	FMB	50	242.3	949.1	15	102.5	plastic	
15	9/26/2008	FMB	50	116.3	835.1	5	101.3	top and sides reinforced	
16	9/26/2008	FMB	49	129.3	848.1	10	98.9	top and sides reinforced	
17	9/26/2008	FMB	48	165.9	872.7	15	98.3	top and sides reinforced	
18	9/30/2008	N1	50			10	NA	plastic	
19	10/1/2008	K1	52			10	NA	plastic	
20	10/2/2008	K2	103			10		plastic	
21	10/3/2008	K3	150			10		plastic	
22	10/3/2008	K4	200			10		plastic	
23	11/7/2008	FMB	54	169.3	888	5	112.2	plastic	

24	11/7/2008	FMB	50	162.8	881.6	5	107.4	plastic	
25	11/7/2008	FMB	52	149	867.6	5	75.6	plastic	
26	11/7/2008	FMB	53	214.3	932.9	10	101.4	plastic	
27	11/7/2008	FMB	51	202.2	920.3	10	107.9	plastic	
28	11/7/2008	FMB	51	218.4	938.4	10	106.5	plastic	
29	11/7/2008	FMB	49	257.8	977.9	15	103.8	plastic	
30	11/7/2008	FMB	53	242.3	962.2	15	109.1	plastic	
31	11/7/2008	FMB	49	238.9	957.5	15	99.8	plastic	
32	11/7/2008	FMB	100	159.6	878.4	5	145.2	plastic	
33	11/7/2008	FMB	101	155.6	875	5	148.9	plastic	
34	11/7/2008	FMB	102	160.7	879.9	5	148.5	plastic	
35	11/7/2008	FMB	97	215.3	924.5	10	148.8	plastic	
36	11/7/2008	FMB	100	219.2	938.4	10	144.6	plastic	
37	11/7/2008	FMB	101	204.9	924.2	10	148.6	plastic	
38	11/24/2008	FMB	105	254.1	973.3	15		plastic	
39	11/24/2008	FMB	104	231.2	950.3	15		plastic	
40	11/24/2008	FMB				15		plastic	Data Lost
41	2/23/2009	FMB				10		1 in holes on top	Data Lost
42	2/23/2009	FMB				10		1 in holes on top	Data Lost
43	2/23/2009	FMB				10		1 in holes on top	Data Lost
44	2/26/2009	FMB				10		1 in holes on top	Data Lost
45	2/26/2009	FMB				10		holes on top	
47	2/26/2009	FMB				10		holes on top	
48	2/27/2009	FMB	100	207.8	926.7	10	149.3	holes on side	
49	2/27/2009	FMB	100	196.8	915.7	10	144.9	holes on side	
50	2/27/2009	FMB	100	233.9	952.8	15	142.5	holes on side	
51	3/6/2009	FMB	100	236.6	955.5	10	143.9	holes on side	
52	3/6/2009	FMB	100	259.5	978.4	10	146.24	holes on side	
53	3/6/2009	FMB	150	243.3	962.2	10	176.6	holes on side	
54	3/6/2009	Beam	100	262.5	981.4	10		holes on side	Data Lost
55	3/16/2009	Beam	100	271.3	990.2	10	143.4	holes on side	
56	3/16/2009	Beam	150	257	975.9	10	174.5	holes on side	
57	3/17/2009	Beam	150	277.4	996.3	10	175.4	holes on side	
58	3/19/2009	Beam	100	247.5	966.4	10	130.2	holes on side	middle strain gage lost
59	3/19/2009	Beam	100			10	73.47	holes on side	Data lost
60	3/23/2009	Beam	150	246.3	962.3	10	174.5	holes on side	Middle strain gage lost
61	4/7/2009	Beam	150	232	947.2	10	177.6	holes on side	Middle lost strain gage lost
62	4/7/2009	FMB	100	259.9	976	10	138.8	holes on side	
63	4/7/2009	FMB	100	231.9	948	10	144.9	holes on side	
64	4/7/2009	FMB	100	262.4	978.5	10	141.3	holes on side	Fracture in middle
65	4/30/2009	Beam	75	260.1	976.2	10	118.2	holes on side	Oversaturated strain gage data
66	5/5/2009	FMB	50	395	1111.1	10	103.5	holes on side	Plastic front
67	5/5/2009	FMB	100					holes on side	

68	5/26/2009	Beam	100	348.1	1067.9			holes on side	
69	5/26/2009	Beam	100	271.4	989.2	10	142.6	holes on side	
70	5/26/2009	Beam	100	257.2	976.6	10	144.3	holes on side	
71	5/26/2009	Beam	100	341.1	1061.2	15	141.1	holes on side	
72	9/3/2009	Sand 01	100	335.1	1053	15	138.5	holes on side	
73	9/11/2009	Sand 02	75	220.1	937.1	5	120.3	holes on side	
74	9/11/2009	Sand 03	75	264.5	981.5	10	117	holes on side	
75	9/11/2009	Sand 04	75	264.8	983.9	10	118.1	holes on side	
76	9/11/2009	Sand 05	100	256	975.3	10	140.7	holes on side	
77	9/14/2009	Sand 06	100	267.1	984.4	10	139.9	holes on side	
78	9/14/2009	Sand 07	100	229.8	949.3	5	142.8	holes on side	
79	9/14/2009	Sand 08	75	252.2	971	10	118.4	holes on side	
80	9/14/2009	Sand 09	100	274.7	993.5	10	141.9	holes on side	
81	9/14/2009	Sand 10	100	288.9	1006.2	10	141.2	holes on side	
82	9/14/2009	Sand 11	100	283.1	1000.5	10		holes on side	lost data
83	10/6/2009	Sand 12	100	296.5	1016.7	10	140.6	holes on side	
84	10/6/2009	Sand 13	100	291.3	1021.9	10	140.2	holes on side	
85	10/13/2009	Sand 14				10	143.1	holes on side	
86	10/13/2009	Sand 15				10	142.1	holes on side	
87	10/27/2009	FC01	102	218.1	939.5	5	144.9	holes on side	
88	10/27/2009	FC02	50	213.5	934.4	5	100.4	holes on side	
89	10/27/2009	FC03	75	222	942.9	5	121.6	holes on side	
90	10/27/2009	FC04	76	250.5	970.5	10	120.2	holes on side	
91	10/30/2009	FC05	75	290.1	1010.1	10	121.2	holes on side	
92	10/30/2009	FC06	76	295.7	1015.8	10	120.4	holes on side	
93	10/30/2009	FC07	76	338.7	1059.1	15	118.7	holes on side	
94	10/30/2009	FC08	76	334	1054.1	15	119	holes on side	
95	10/30/2009	FC09	75	320.7	1040.8	15	118.8	holes on side	
96	10/30/2009	FC10	77	212.9	933	5	123.1	holes on side	
97	10/30/2009	FC11	75	200.5	920.6	5	123.5	holes on side	
98	11/17/2009	FC12	75	253.6	972.8	10	121.4	holes on side	
99	11/17/2009	FC13	75	203.9	922.9	5	120	holes on side	
100	11/17/2009	FC14	75	342.9	1061.9	15	115.7	holes on side	
101	1/15/2009	Sand 15	75	245	964.6	10		holes on side	lost data
102	1/15/2009	Sand 16	75	257.7	975.7	10	118.2	holes on side	
103	1/20/2009	Sand 17	75	259.9	980.2	10	124.6	holes on side	
104	1/25/2010	FC15	75	255.8	974.8	10		holes on side	lost data
105	1/25/2010	FC16	75	344	1064.5	15	118.2	holes on side	
106	1/25/2010	FC17	75	348.2	1068.5	15	121.1	holes on side	

107	1/25/2010	FC18	75	324.2	1045	15	123.7	holes on side	
108	1/25/2010	FC19	75	324.4	1045.2	15	123	holes on side	
109	1/25/2010	FC20	75	247.4	967.7	10		holes on side	lost data
110	1/25/2010	FC21	75	261.6	982.2	10	123.9	holes on side	
111	1/25/2010	FC22	75	260.1	980.7	10	124	holes on side	
112	1/25/2010	FC23	50	208.1	928.8	5	105.4	holes on side	
113	1/25/2010	FC24	75	235.4	956.1	5	125	holes on side	
114	1/25/2010	FC25	75	221	941.7	5	125.4	holes on side	
115	1/25/2010	FC26	75	210.8	930.9	5	125.1	holes on side	

Appendix VII CAD Drawings

Three Point Bend Fixtures

The following are drawing of the fixtures used for quasi-static and intermediate speed three point bend tests.

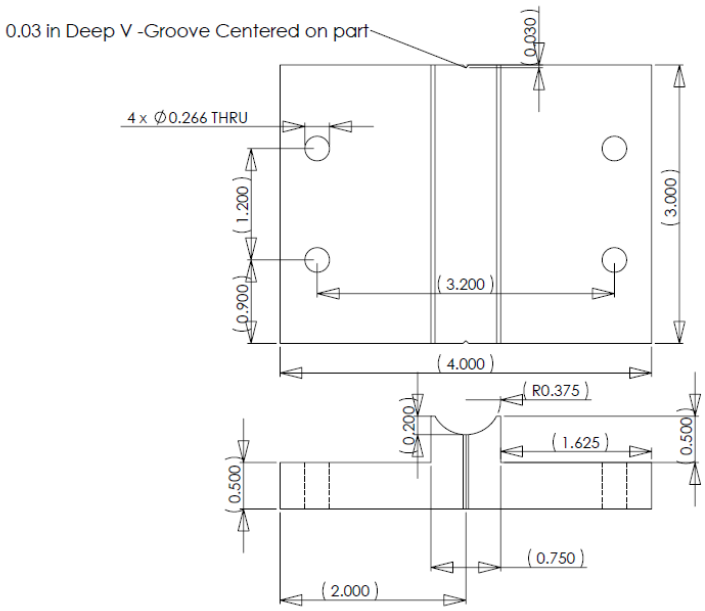

Figure 101. Center Roller (dimension in inches, material: aluminum)

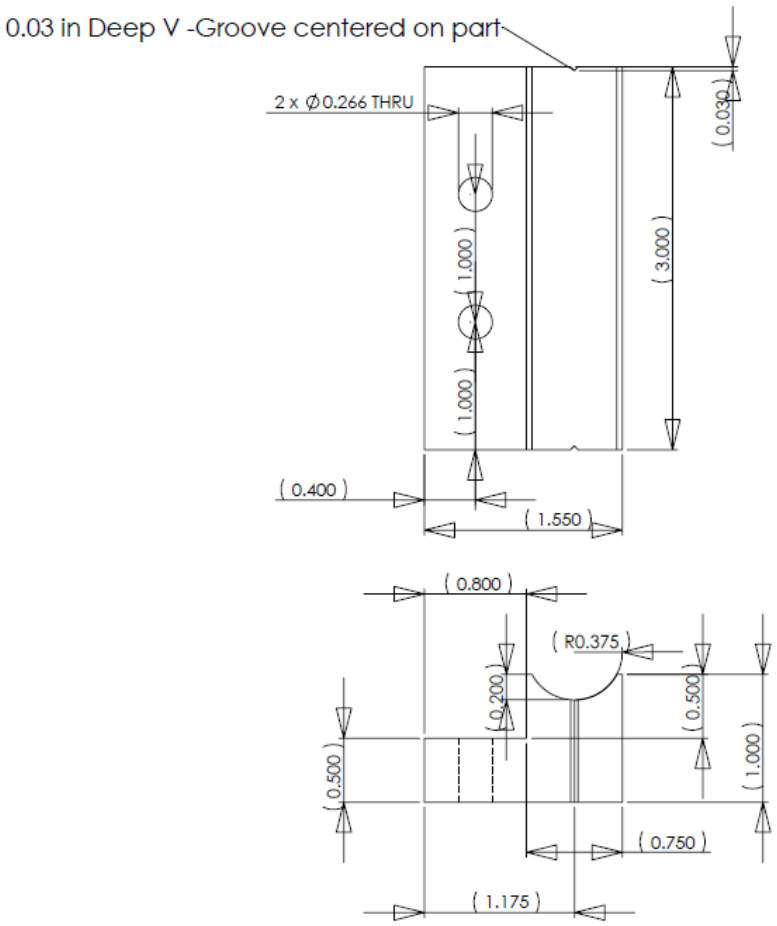

Figure 102. Roller mount for 0.75 in diameter roller (dimensions in inches, material: aluminum)

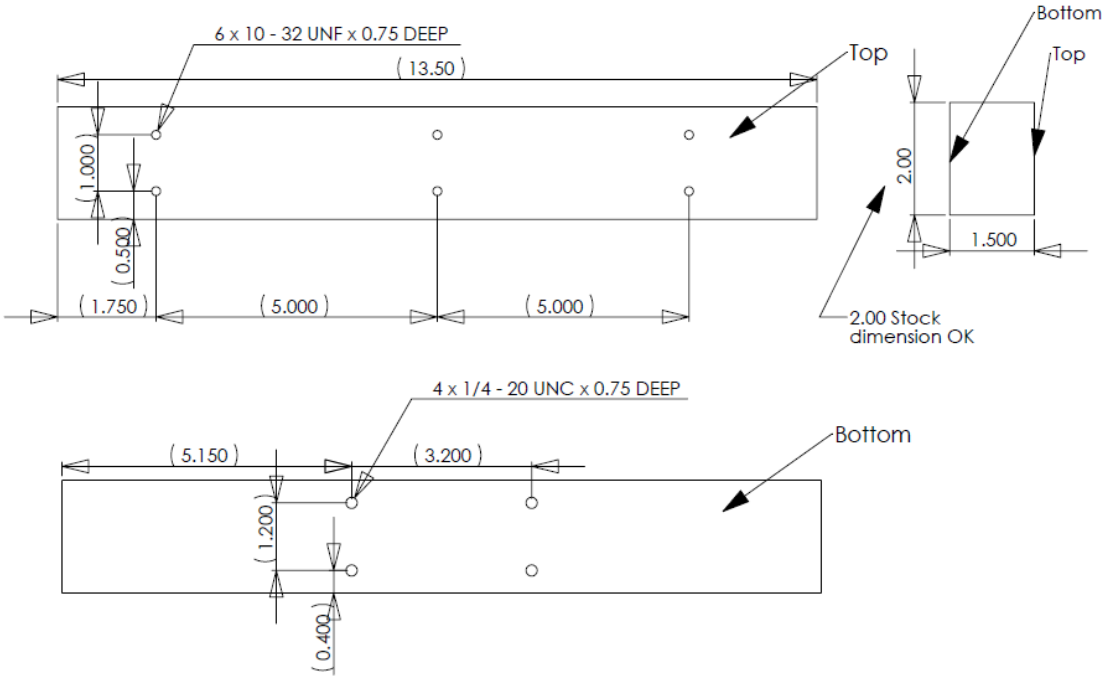

Figure 103. Stainless steel beam (dimensions in inches, material: stainless steel)

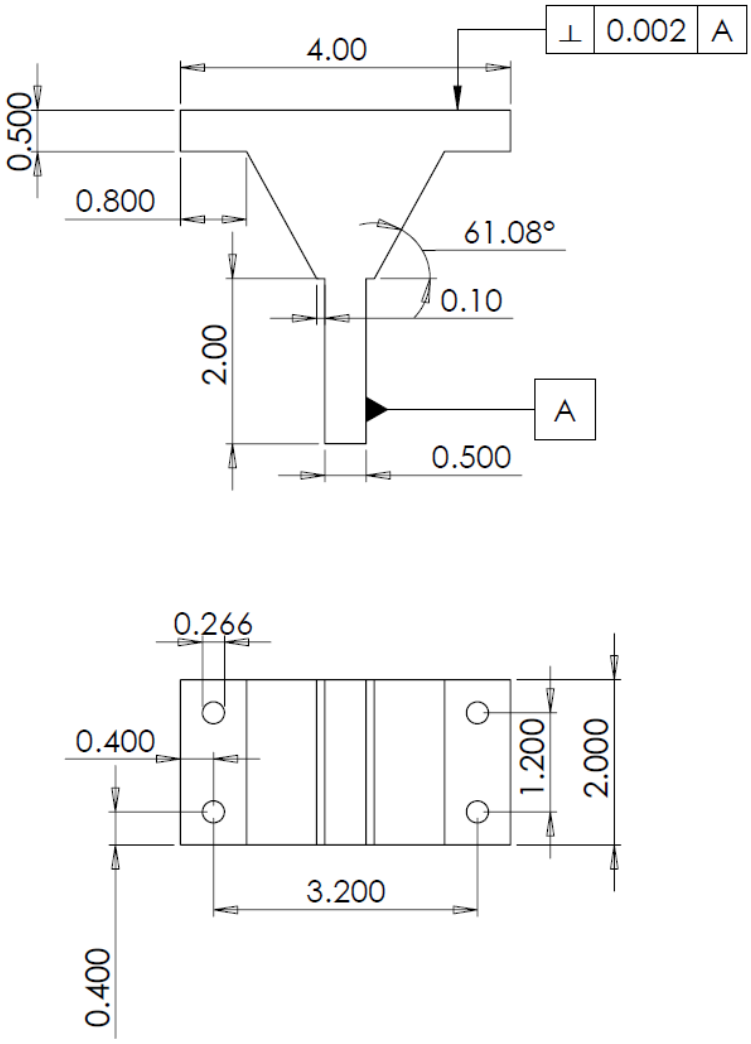

Figure 104. Compression platen (dimensions in inches, material: hardened A2 steel)

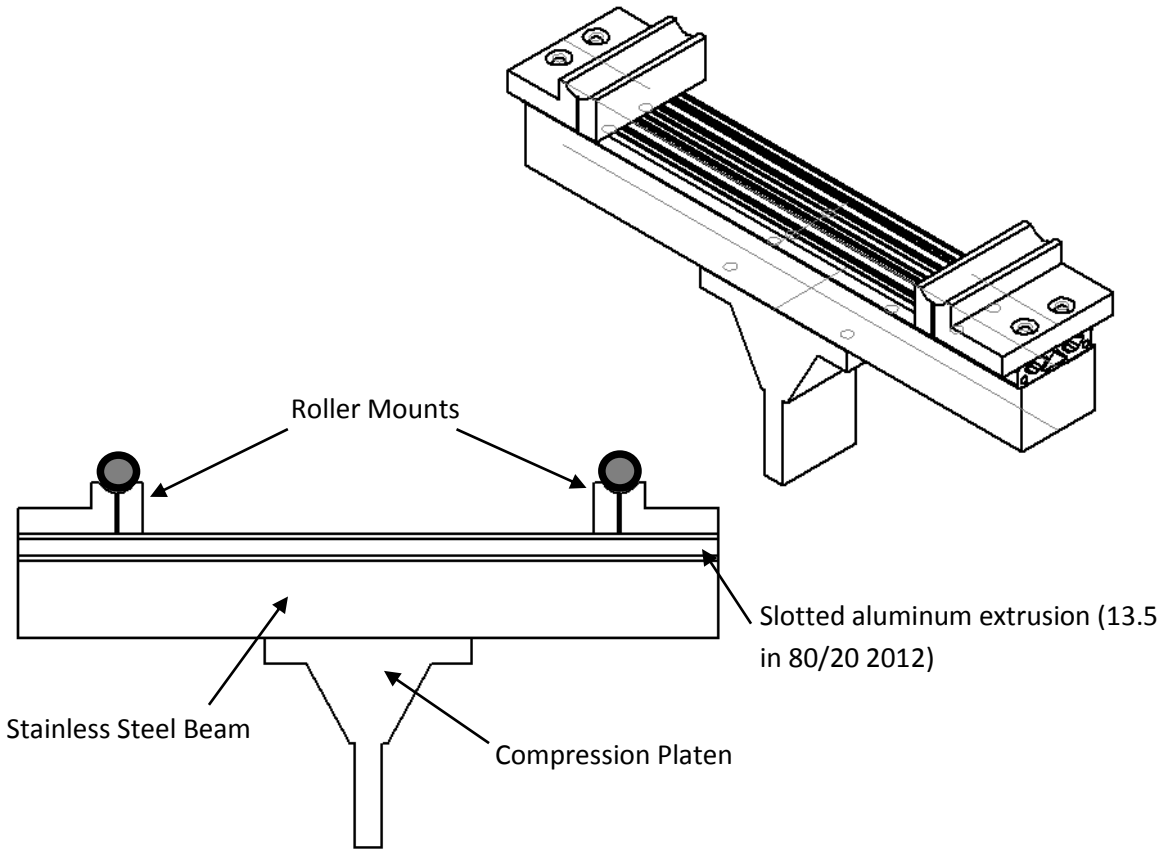

Figure 105. Three-point bend test fixture assembly

Fig. 105 illustrates the assembled three-point bend test fixture. The compression platens connect to four 1/4-20 threaded holes on the bottom of the stainless steel beam. A slotted aluminum extrusion (80/20 2010) connects to the top of the stainless steel beam via six 10-32 UNF threaded holes. The roller mounts are then bolted to the slotted aluminum extrusion. Note that the assembly allows the roller mounts to slide giving a variety of beam spans. 0.75 in rollers are attached to the roller mounts using cyanoacrylate adhesive (super glue).

Parts for PPGP

The following are drawings for the parts used for the PPGP.

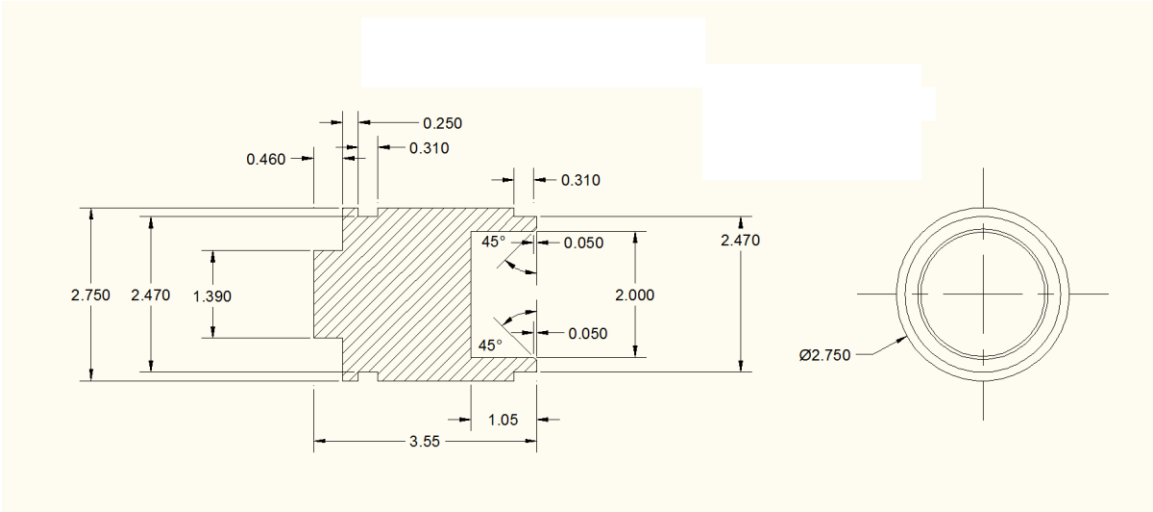

Figure 106. Aluminum mass (dimensions in inches, material: aluminum)

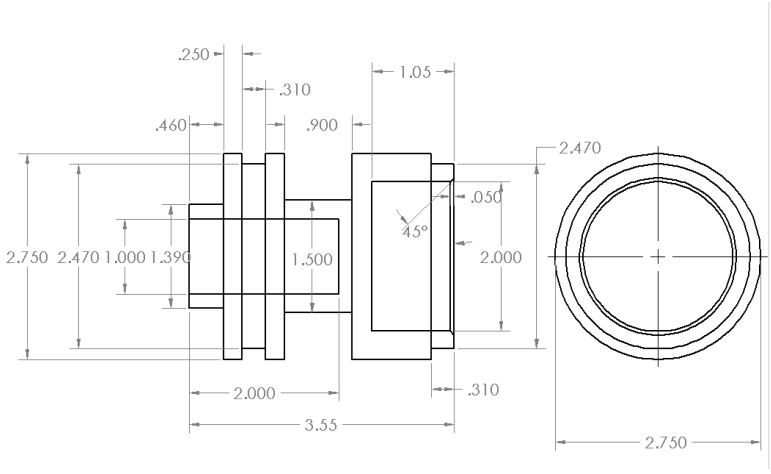

Figure 107. Lightened aluminum mass (dimensions in inches, material: aluminum)

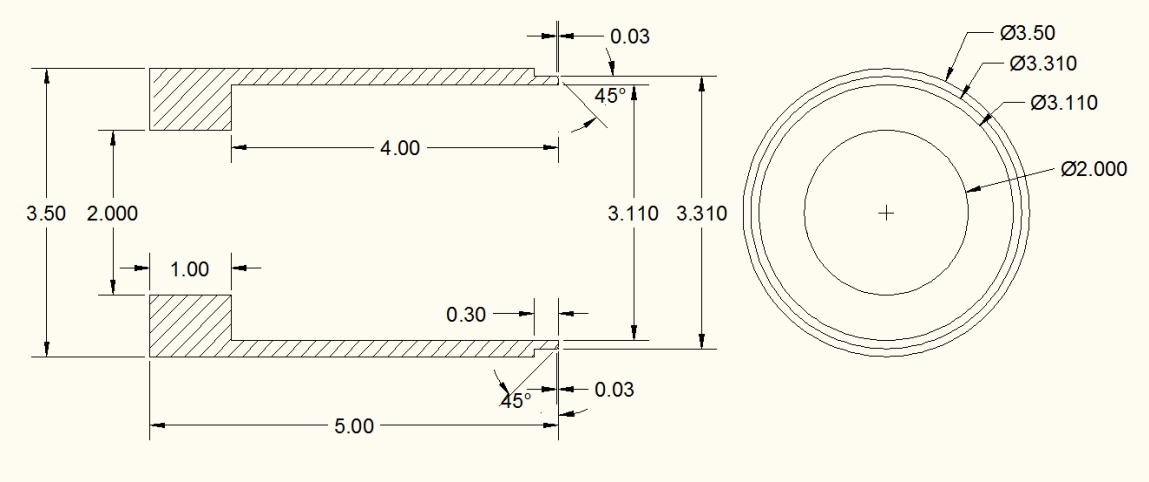

Figure 108. Foam body mold part A: 5 in main body (dimensions in inches, material: stainless steel)

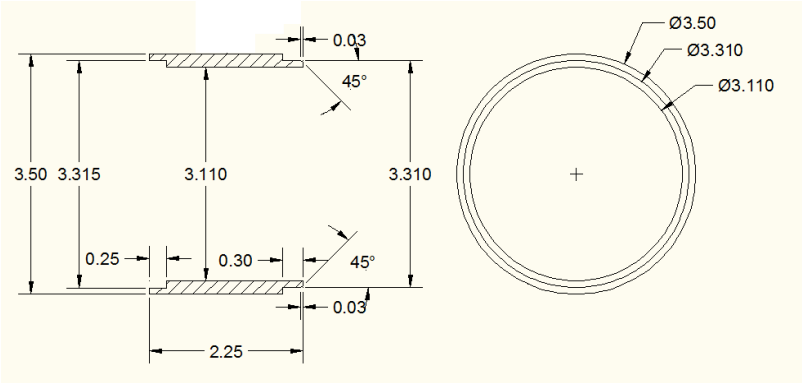

Figure 109. Foam body mold part B: 2.25 in extension (dimensions in inches. material: stainless steel)

Gas Gun Test Fixtures

The following are drawings for the fixtures used during gas gun tests.

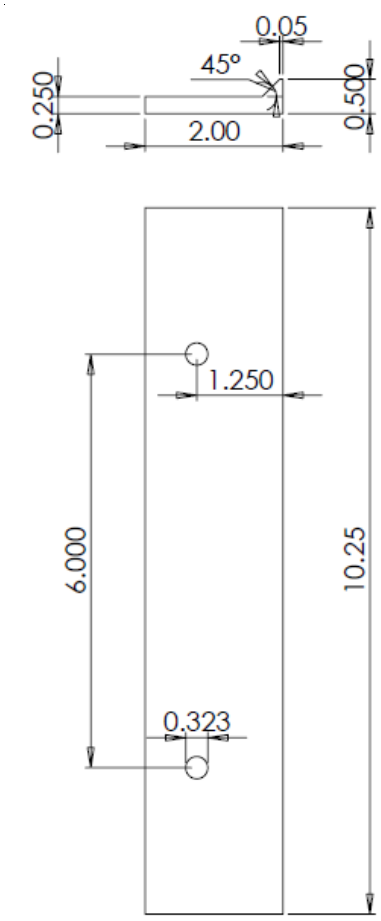

Figure 110. V-block fixture

Appendix VIII Pressure Pulse FEA

Preliminary computational modeling analysis was done using ABAQUS/Explicit, creating a 2D axisymmetric model of the PPGP impacting a 3.5 m FMB with an initial velocity of 50 m/s. The PPGP model, shown in Fig. 111, was composed of intermediate density foam with an aluminum backer mass, with the following dimensions: 76.2 mm diameter and 152.4 mm length. The foam was modeled as elastic-plastic and the aluminum was modeled as Al 6061-T6 elastic.

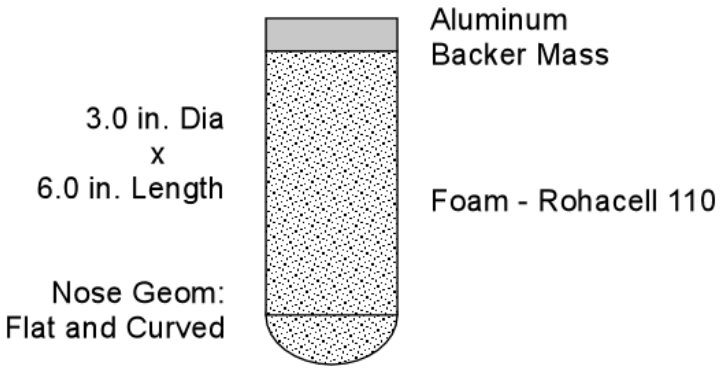

Figure 111. PPGP computational model

This modeled explored the effects of different nose geometry: flat and curved. Fig. 112 shows the results of the tests: deformation at t = 0.3 ms. The pressure time history shape was found to be tunable by adjusting nose geometry. The resulting pressure time histories for each nose geometry us shown in Fig. 113. Varying foam strength and density was found to modify the pressure pulse history shape as well as projectile

velocity (see Fig. 114). Higher density foam has higher crush strength and has more momentum for a given velocity. Higher velocity provides more momentum.

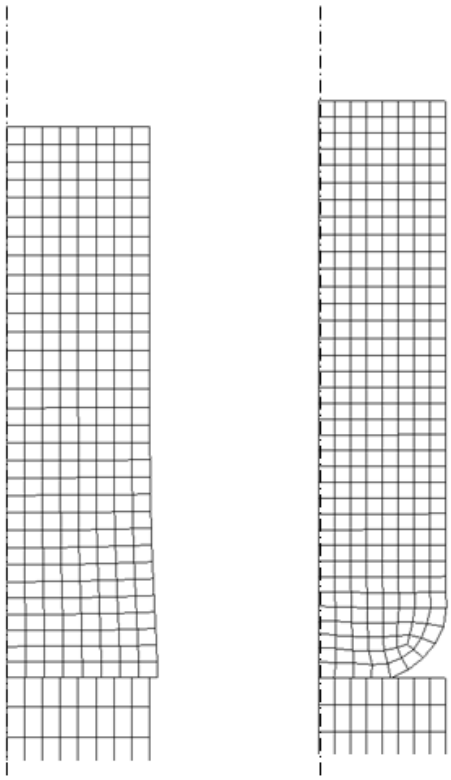

Figure 112. Deformation for (a) flat nose (b) curved nose geometry at t = 0.3 ms

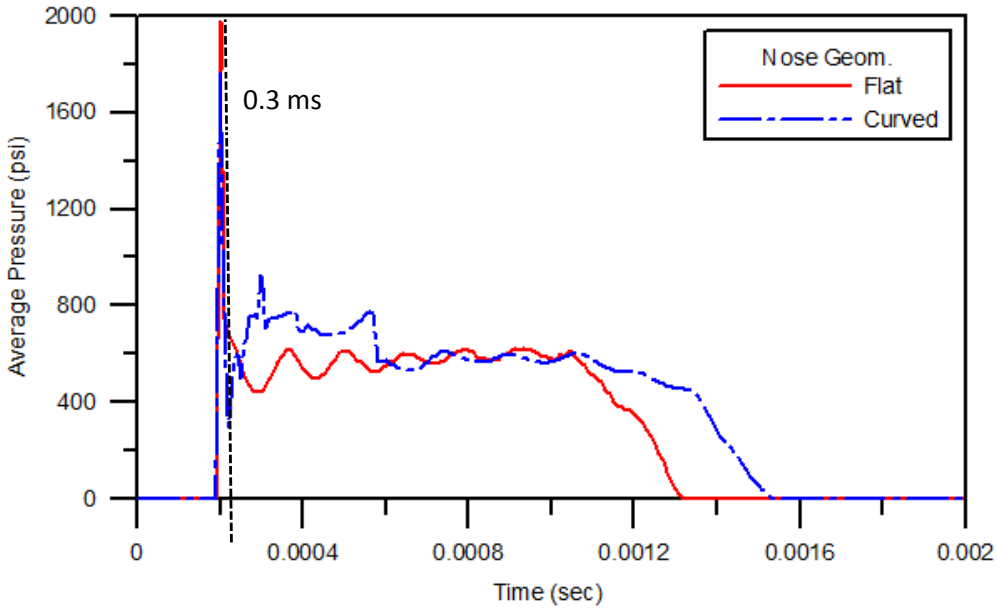

Figure 113. Pressure versus time for PPGP computational model flat and curved nose geometry at 50 m/s

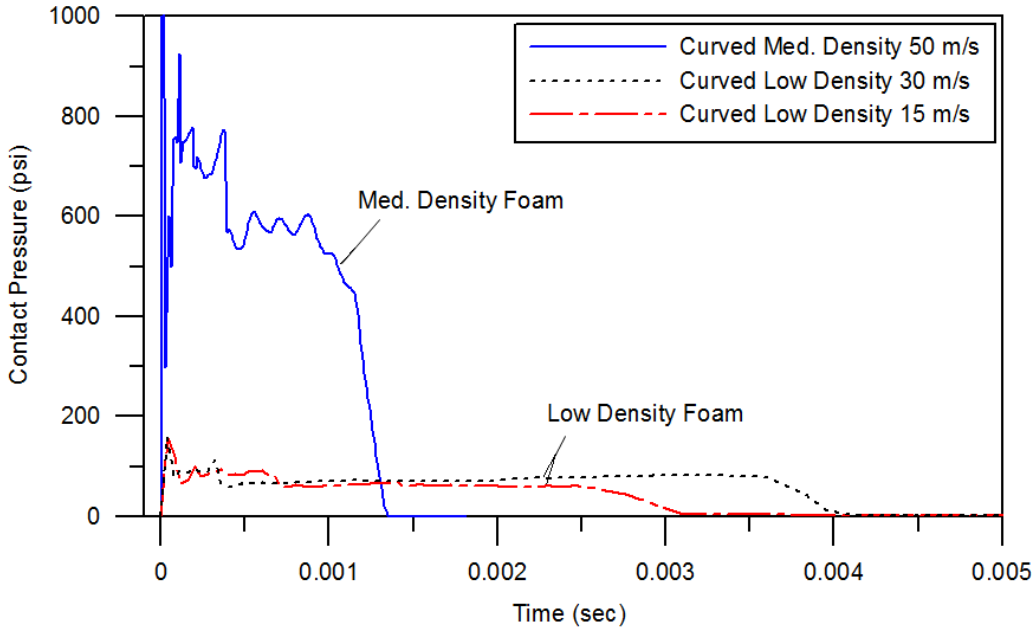

Figure 114. Pressure versus time for PPGP computational model: multiple density and velocity

The pressure pulse developed from impact on composite panel targets was explored. Fig. 115 shows the total contact force over time of a Rohacell 110 foam projectile impacting at 50 m/s three targets: FMB, sandwich panel (4 mm carbon/epoxy skins and 50.8 mm core), and thin skin (single 4 mm carbon/epoxy skin). It was found that the resulting force pulse was not strongly dependent on target stiffness.

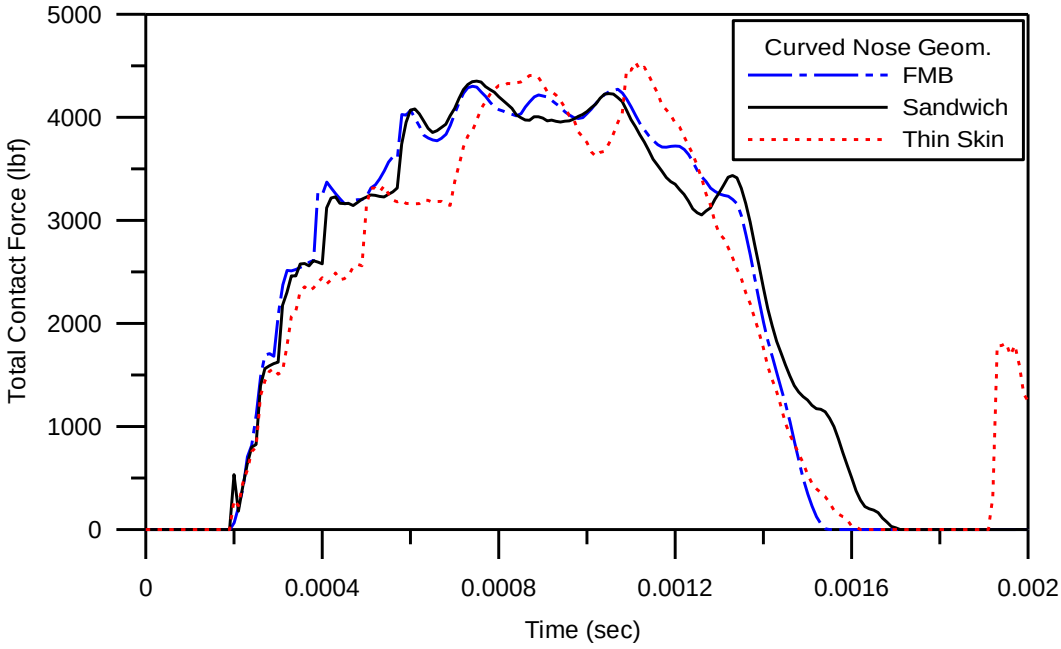

Figure 115. Total contact force versus time; Rohacell 110 foam projectile at 50 m/s